ABSTRACT

Title of Dissertation: USING SINGLE MOLECULE TECHNIQUES TO DETERMINE THE MECHANISM OF DNA TOPOLOGY SIMPLIFICATION BY TYPE IIA TOPOISOMERASES

Ashley Harris Hardin, Ph.D., 2011

Dissertation Directed By: Professor Devarajan Thirumalai
Institute for Physical Science and Technology
Department of Chemistry and Biochemistry

Type IIA topoisomerases are essential, universally conserved proteins that modify DNA topology by passing one segment of duplex DNA (the transfer, or T-segment) through a transient double strand break in a second segment of DNA (the gate, or G-segment) in an ATP-dependent reaction. Type IIA topoisomerases decatenate, unknot, and relax supercoiling in DNA to levels below equilibrium, resulting in global topology simplification. The mechanism underlying non-equilibrium topology simplification remains speculative, though several plausible models have been proposed. This thesis tests two of these, the bend angle and kinetic proofreading models, using single-molecule techniques. The bend angle model postulates that non-equilibrium topology simplification scales with the bend angle imposed on the G-segment DNA by a type IIA topoisomerase. To test this model, we used atomic force microscopy and single molecule Förster resonance energy transfer to measure the extent of bending imposed on DNA by

three type IIA topoisomerases that span the range of topology simplification activity. We found that all proteins bent DNA, but the imposed bends are similar and cannot account for the differences among the enzymes. These data do not support the bend angle model and suggest that DNA bending is not the sole determinant of non-equilibrium topology simplification. Based on the assumption that the rates of collision between DNA segments is higher in knotted, linked, and supercoiled DNA than in topologically free or relaxed DNA, the kinetic proofreading model proposes that two successive binding events between a G-segment bound topoisomerase and a putative T-segment are required to initiate strand passage. As a result of the two step process, the overall rate of strand passage should scale with the square of the collision probability of two DNA segments. To test this model, we used magnetic tweezers to manipulate a paramagnetic bead tethered to the surface by two DNA molecules. By rotating the bead, we varied the proximity, and thus collision rate, of the two molecules to determine the relationship between collision probability and rate of strand passage. Our data indicate that the strand passage rate scales linearly with the collision probability, which is inconsistent with the kinetic proofreading model.

USING SINGLE MOLECULE TECHNIQUES TO DETERMINE THE MECHANISM OF DNA TOPOLOGY SIMPLIFICATION BY TYPE IIA TOPOISOMERASES

By

Ashley Harris Hardin

Dissertation submitted to the Faculty of the Graduate School of the
University of Maryland, College Park, in partial fulfillment
of the requirements for the degree of
Doctor of Philosophy
2011

Advisory Committee:
Professor Devarajan Thirumalai, Chair
Keir Neuman, Ph.D., NIH Advisor
Associate Professor Wolfgang Losert
Associate Professor Jason Kahn
Professor Sergei Sukharev, Dean's Representative

Dedication

This work is dedicated to my husband, Lance, and my children, Luke and Avery.

Acknowledgements

First and foremostly, I would like to thank Keir Neuman, my PhD advisor. It is no understatement to say that I would not be where I am today were it not for his seeming boundless encouragement, patience, and support. I honestly cannot imagine working for a better PI and I consider myself extraordinarily lucky to have been a part of his lab. He bravely accepted the challenge of mentoring me and has helped guide my transformation into the scientist I am today.

I'd also like to thank my fellow lab members, past and present, for their support and help, both professionally and personally. I cannot imagine working with a better group of people and I certainly would not have been able to accomplish any of this without them. In particular, I'd like to thank Junghoon In for teaching me how to use the AFM, Grace Liou for providing me with a seemingly boundless supply of Topo IV, Susanta Sarkar for help with the smFRET experiments, and Yeonee Seol for help with the bend angle data analysis and the magnetic tweezers experiments. I'd also like to thank my on campus advisor, Dave Thirumalai, for his guidance and support, and my PhD committee.

I would be completely remiss not to thank my family and friends who have supported me throughout this process. In particular, I'd like to thank my mom who gave up her entire summer to help me with my new baby when I was frantically trying to finish this dissertation and my husband who agreed to move to Maryland so I could pursue my dream and has been a great support throughout this process. I'd also like to thank my friend Stephanie Guzik, a fellow NIH graduate student who was instrumental in preserving my sanity and humor over the years leading up to this.

Table of Contents

List of Tables

List of Figures

Chapter 1: Background

1.1 Introduction

The discoveries of the importance and structure of DNA are among the most groundbreaking scientific accomplishments of the twentieth century. DNA, with its elegantly terse four letter code, is sufficient to fully characterize all the variation found among living things from the smallest bacteria to the exceptionally complex *Homo sapiens*. Its deceptively simple double helical structure is well suited for storing genetic information due, in part, to the complementary nature of the two strands, which provides a useful mechanism by which the genetic code can be replicated and any mismatches between the paired strands can be addressed. However, because the double helix is so well evolved to protect the DNA code, accessing the nucleotides presents substantial difficulties. In order for a cell to obtain the information stored in its DNA for the critical processes of replication and transcription, it must frequently and efficiently open the double helix to allow access to the nucleotides. However, the process of unwinding a double helix is fraught with physical obstacles. At a replication or transcription fork, the DNA ahead of the machinery becomes overwound and the torsional resistance stalls the replicative or transcriptive process if not resolved. Furthermore, DNA molecules cannot be replicated without the sister chromosomes becoming interlinked. These linkages, if not promptly resolved, will either stall cell division or result in an improper number of chromosomes in both of the daughter cells. To overcome the physical complications inherent in unwinding the double helix, living organisms have evolved a specialized family of proteins that regulate the topology of DNA. These proteins, the topoisomerases, modify DNA topology by removing knots and linkages as well as relaxing and, in some

cases, generating supercoils. Topoisomerases function by creating transient single or double stranded breaks in a DNA molecule and then passing a second strand or duplex through the lesion or, in the case of type IB topoisomerases, allowing for rotation around the intact strand. By untangling and unlinking DNA molecules and relieving the tension buildup ahead of the replication and transcription forks, topoisomerases enable cells to efficiently access their genetic code while ensuring that the nucleotides remain protected. Because DNA topology is of utmost concern for all life, topoisomerases are essential and universally conserved. Also, the tendency for them to be up-regulated in dividing cells makes them extremely potent anticancer drug targets. Though these vital and indispensable proteins have been studied extensively since their discovery in the 1970s, there are still many open questions about them. In this thesis, I address the question of the mechanism underlying topology simplification by type II topoisomerases.

1.2 The Structure of DNA and the Topology Controversy

Deoxyribonucleic acid (DNA) is the universal encoder of genetic information and is essential to all life. All of the information necessary for an organism to fully form from a single cell, perform its designated function, synthesize required proteins, and reproduce itself at the proper time is encoded in its DNA. Although we now know a great deal about DNA, the discovery of its importance, function, and structure are relatively recent scientific achievements. DNA was discovered in 1869 by Friedrich Miescher (1), and groundbreaking work by Albrecht Kossel and Phoebus Levene in the late 1800s and early 1900s showed that DNA is a polymer with repeating units, called nucleotides, consisting of some configuration of deoxyribose sugars, phosphate groups, and four nitrogenous

bases: cytosine, guanine, adenine, and thymine (1). Although there was speculation early on that DNA plays a role in the transmission and storage of genetic information, it was not immediately obvious that DNA is the molecule of heredity. Many biochemists believed that the DNA molecule was much too simple to be responsible for the vast variation in species. This belief was based, in part, on Levene's incorrect but extremely popular tetranucleotide hypothesis, which speculated that the various nucleotides were present in equimolar ratios in DNA and that each monomer of the DNA polymer was identical and contained one of each of the four bases (1). As a result of the wide acceptance of this hypothesis, which obscured DNA's ability to encode information, it was half a century before DNA was established as the molecule of heredity by the breakthrough work of Avery, Macleod, and McCarty in 1944 (2). Avery and colleagues showed that DNA, not proteins, were responsible for the transfer of genetic information from one generation to the next and by doing so, unleashed a frenzy of research on what had previously been considered a mundane molecule. In 1951, Erwin Chargaff showed that though the absolute quantities of each nitrogenous base varied among the DNA of different organisms, a 1:1 ratio of cytosine to guanine and adenine to thymine remained fixed (3). This result disproved the tetranucleotide hypothesis and revealed a mechanism, the ordering of the bases, by which DNA could possibly encode information (1).

In 1953, the structure of DNA was famously solved by James Watson and Francis Crick (4,5). Based on the previous studies of DNA composition and unpublished X-ray diffraction pictures of crystallized DNA taken by Rosalind Franklin and Raymond Gosling (6), Watson and Crick postulated that DNA exists as a right-handed double helix

with the nitrogenous bases located on the interior of the molecule, bound to one another via hydrogen bonds, which served to hold the two anti-parallel strands together.

The four bases can be subdivided into two categories, based on their chemical structure. Cytosine and thymine are pyrimidines which contain one aromatic ring, and adenine and guanine are purines, which contain two fused aromatic rings and are therefore larger than the pyrimidines (Figure 1.2.1) (7). Since the X-ray data showed a uniform helix, the two bases spanning the interior of the helix have to be of uniform size. The observation that a purine-purine pair would be much larger than a pyrmidine-pyrimidine pair was powerful evidence that each nucleotide "bridge" must consist of a complementary purine-pyridimine pair. In addition, Chargaff's previous discovery that adenine and thymine occur in equimolar ratios, as do cytosine and guanine, helped reveal the base pairing rules, which immediately suggested a built-in replication mechanism where each strand could serve as a template strand for its complementary partner (1,4,5).

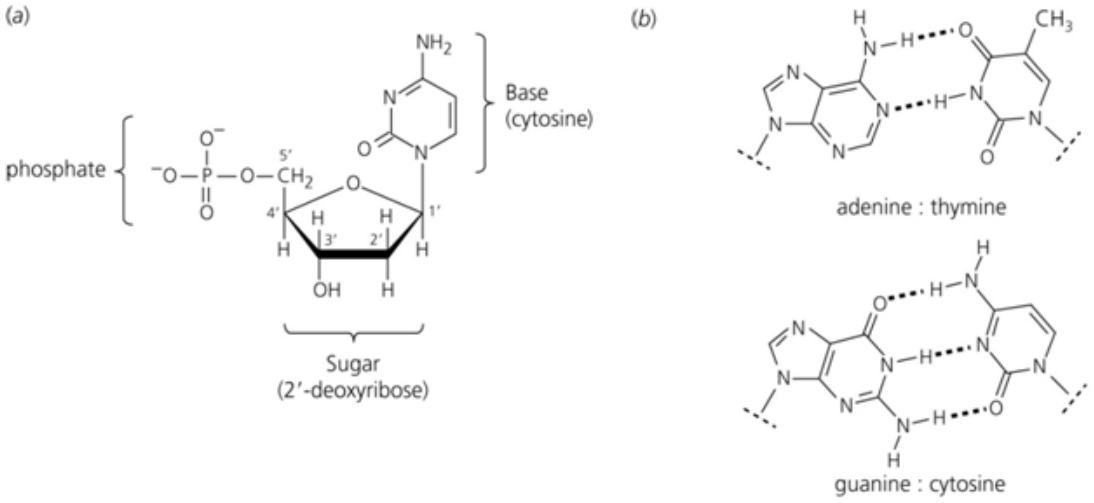

Figure 1.2.1 DNA nucleotide and base pairs **A.** The chemical structure of a nucleotide. **B.** The two types of base pairing schemes possible in DNA. [Reproduced Fig. 1.1 from (7), with permission (Appendix A)]

The double helical model of DNA, held together by hydrogen bonded complementary bases (Figure 1.2.2), provided a convenient semi-conservative replication mechanism, whereby the strands could unwind and each strand could then serve as a template for the creation of a new complementary strand (4,5). However, the controversy surrounding DNA structure was far from over. Several scientists were skeptical of this replication mechanism, especially as chromosomal DNA was shown to be much longer than originally thought. The physical act of unwinding very long DNA strands, which would be necessary during DNA replication, would generate sufficient shear force to cause extensive breakage of the DNA backbone (8). In addition, the discovery of circular DNA molecules that were intact, and hence, covalently closed, led to further skepticism of the semi-conservative replication by unwinding theory since it is impossible to unwind a circular DNA molecule without breaking the backbone (8). It seemed that the unwinding problem presented an intractable barrier to effective and efficient DNA replication if the DNA were, indeed, a double helix.

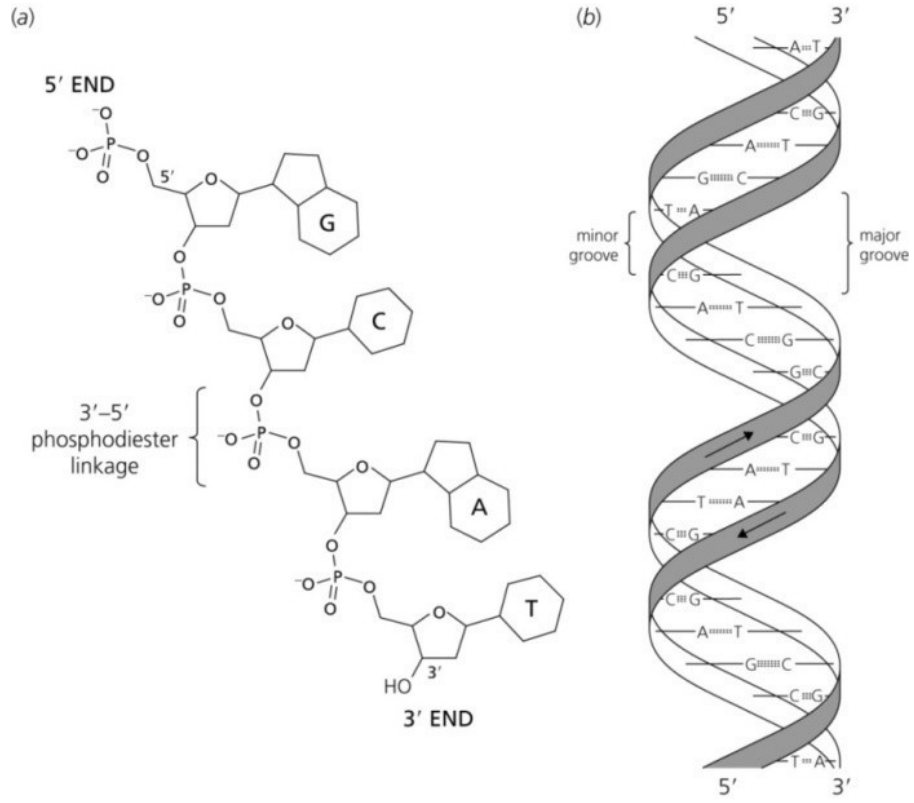

Figure 1.2.2 The structure of DNA **A.** The chemical structure of nucleotides joined at the phosphate backbone. **B.** The double helical structure of DNA [Fig 1.2 from (7), with permission (Appendix A)]

A landmark publication in 1958 by Matthew Meselson and Frank Stahl showed that the circular DNA of *Escherichia coli* indeed utilizes a semi-conservative replication mechanism in which the strands completely separate during replication. This result revealed that the DNA molecule must somehow overcome seemingly insurmountable topological barriers and completely unwind (9). As a result of this discovery, mathematicians Pohl and Roberts (10) rejected the double helical model outright due to the topological obstacles associated with unwinding a DNA double helix that was hundreds of thousands, or even millions, of base pairs long or covalently closed in circle, as was the case for *E. coli*. Other researchers, such as Rodley *et al*. (11) and Sasisekheran and colleagues (12,13), in an effort to avoid the unwinding problem, proposed an alternative DNA structure: a side by side (or paranemic) model of DNA that postulated the strands of DNA lay side by side in a repeating helix of five right hand turns followed by five left hand turns that would keep the strands topologically isolated, as opposed to Watson and Crick's plectonemic model in which the DNA strands are wound around one another (14,15). This structure was still able to match the X-ray pictures of DNA, but allowed the strands to separate without unwinding.

The DNA topology problem grew even more complicated when DNA supercoiling was discovered in the mid-1960s. It was assumed that a sample of DNA from an organism with a circular chromosome would contain two populations: circular DNA and linear DNA, which would be generated by the harsh treatment of DNA during purification. Researchers were surprised, however, to find three distinct topological populations of DNA when a sample containing DNA purified from the polyoma virus, that had previously been shown to contain closed circular DNA, was subjected to

sedimentation by ultracentrifugation. Inspecting the three sample components with an electron microscope, Vinograd *et al.* (16) found that there were three populations of DNA: one linear population and two distinct populations of closed circular DNA. The most abundant population consisted of DNA rings that contained many self-crossings and were compacted into a superhelical structure. The less abundant circular population contained DNA rings that had a circular appearance with few, if any, crossings (Figure 1.2.3) (15,16). The least abundant population contained linear DNA. The DNA that was tightly coiled around itself was later determined to be negatively supercoiled, or twisted in the direction opposite that of the double helix, and it was soon after determined that circular DNA molecules purified from organisms exist predominantly in a negatively supercoiled state (15). Because the "relaxed" open circles are the conformation with the lowest free energy, maintaining the DNA in a perpetually underwound state has a net energetic cost to the cell. Thus, not only must there be a reason for the DNA to adopt such an energetically costly conformation, there also has be some sort of mechanism to push the DNA topology away from the energetically favored open conformation towards the negatively supercoiled state (15).

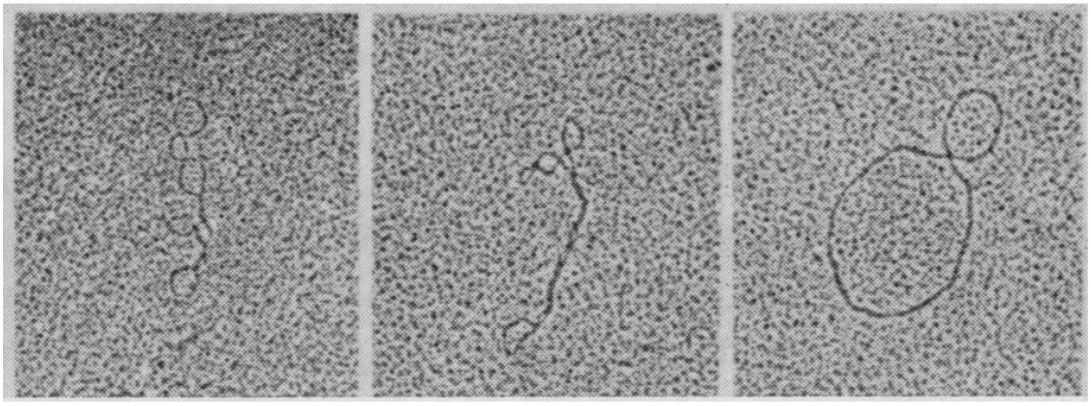

Figure 1.2.3 Electron micrographs of DNA with varying levels of supercoiling. Panels 1 and 2 show highly supercoiled DNA molecules and panel 3 shows a slightly supercoiled DNA molecule with only one superhelical crossing. [Adapted from Fig. 2-1 from (15)]

1.3 DNA Topology

1.3.1 Buildup of Torsional Strain During Replication and Transcription

The DNA double helix gives rise to a host of inherent topological problems. Most eukaryotic chromosomes, which can be millions of base pairs long, are one long contiguous strand of DNA, and many organisms, such as bacteria and some viruses, contain circular DNA rings. The two strands of DNA are intertwined, much like the strands in a rope, and those strands need to be separated in order for the cell to access the genetic information stored inside. When the DNA helix is "unzipped" in order to allow the transcription and replication machinery to access the bases, torsional strain accumulates ahead of the fork that is formed as the strands are separated (Figure 1.3.1) (7). Without a method to relieve this strain, the buildup of torsion would quickly stall the cellular machinery responsible for replication and transcription. Because the genetic code must be accessed continuously for protein synthesis, this challenge must be overcome in order for the strands of DNA to separate regularly and without too great an energetic cost to the cell (7).

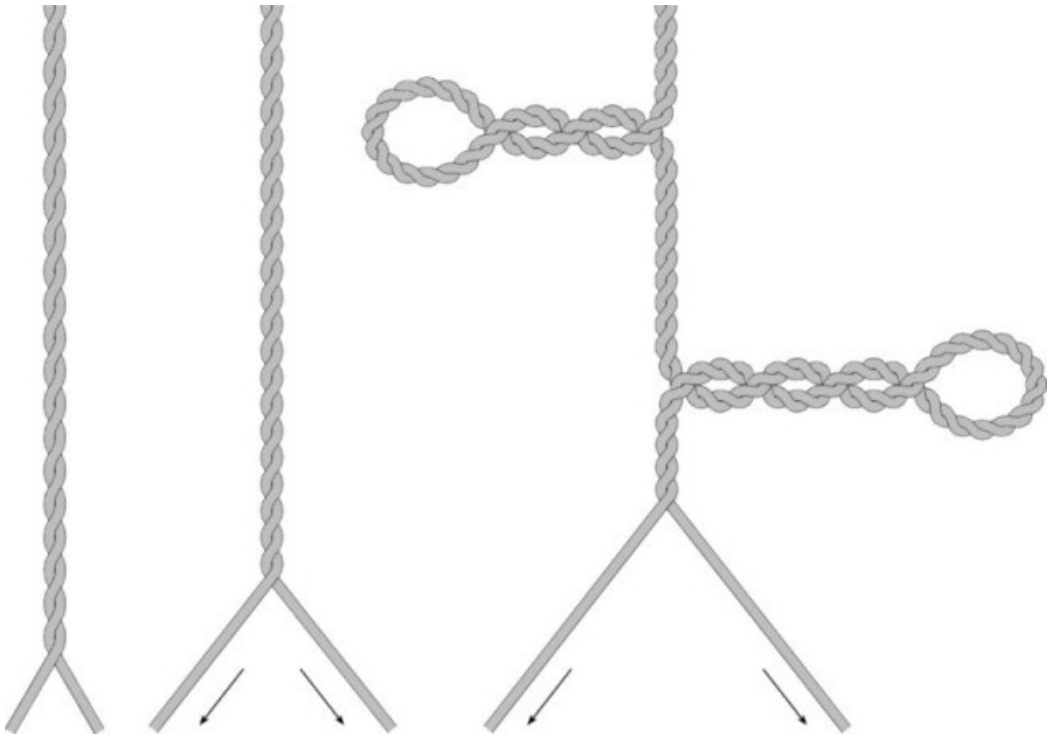

Figure 1.3.1 Illustration of the buildup of torsion and creation of plectonemic supercoils ahead of the separation fork when two interwound strands are separated. [Fig. 2.1 from (7), with permission (Appendix A)]

1.3.1 DNA Supercoiling

In addition to the unwinding and torsional buildup challenges during replication and transcription, another topological concern is the spatial constraint imposed by the size of the nucleus, which is where all cellular DNA, with the exception of mitochondrial DNA, is located in eukaryotes. A mammalian genome is on the order of 2 m in length, but it must be compressed in order to fit inside the nuclear compartment which is on the order of only 10^{-17} m^3 (17). In fact, if it were possible to enlarge the nucleus of a human cell to the size of a baseball, the DNA it contains would be about 150 miles long (15)! In prokaryotes, there is a similar size concern since the overall size of a prokaryotic organism can be an order of magnitude smaller than a eukaryotic nucleus. In order to fit the entire genome inside this compressed intranuclear or intracellular space, it is necessary for the DNA to be as compact as possible. To accomplish this goal, the DNA can either be underwound or overwound to the extent that it adopts a more compact plectonemic or superhelical structure as shown in Figure 1.2.3. As discovered by Vinograd *et al.* (16), the DNA in a cell is maintained in a perpetually underwound state. Because the DNA has to be easily accessible by the replicative and transcriptive machinery of the cell, keeping the DNA underwound has certain advantages since it requires less energy to separate the strands of underwound DNA than to separate the strands of relaxed or overwound DNA. Underwound DNA is referred to as negatively supercoiled ((−) sc) and overwound DNA, as in the case of DNA ahead of the replication or transcription fork, is referred to as positively supercoiled ((+) sc).

Supercoiling of circular DNA molecules can be quantified by a variable known as the linking number (*Lk*). The linking number is a measure of the degree of linking

between two intertwined closed rings and can be calculated by projecting two curves onto a plane, assigning them a polarity, and then assigning a sign to each crossing (or node) of the two curves according to the convention shown in Figure 1.3.2. The linking number is the sum of all the crossings divided by two and is always an integer. Two rings that are not intertwined would have a linking number of zero. Because strands are taken to go in the same direction, by convention, the sign of right-handed DNA crossings is positive (7).

Because DNA generally has a helical pitch of 10.5 base pairs (bp) per turn under standard conditions (0.2 M NaCl, pH 7, 37°C) (18), a circular DNA molecule can only be made to lie flat in a plane if the ends of the DNA line up exactly, i.e. the number of base pairs is an exact multiple of 10.5. Otherwise, the DNA will have to slightly under or over twist in order for the two ends to join. Because this amount of twist is small when considering the thousands or tens of thousands of base pairs that make up the molecule, the linking number for the lowest energy conformation of a closed circular DNA molecule (denoted Lk_m by convention) is the closest integer to the number of base pairs divided by the helical pitch:

$$Lk_m \approx \frac{N}{10.5} \qquad [1.3.1]$$

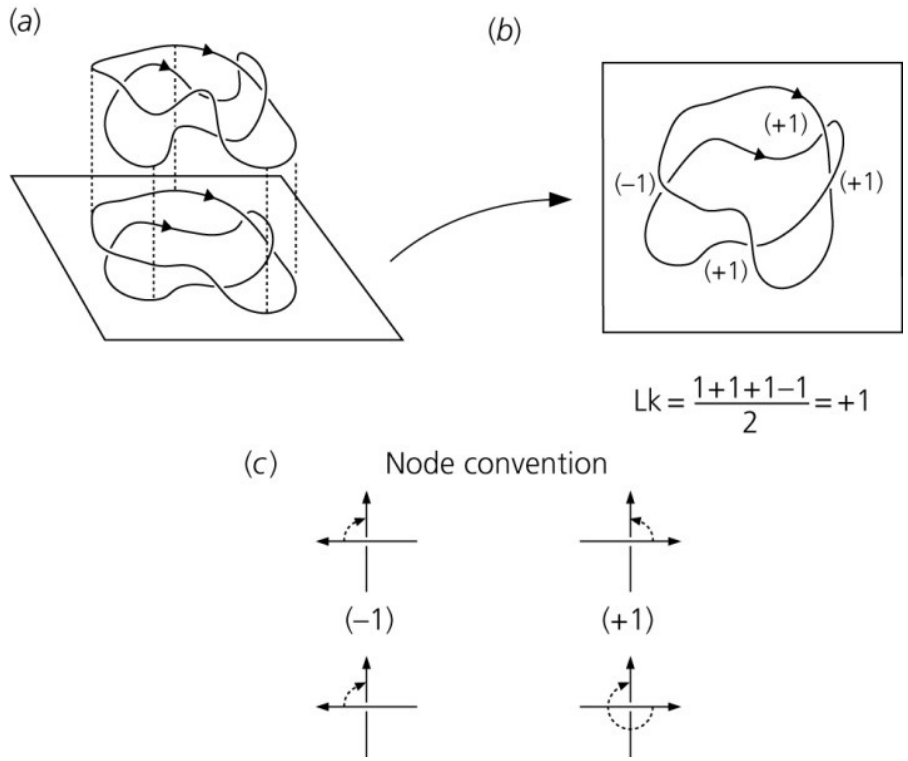

Figure 1.3.2 To calculate the linking number of two linked rings **A.** first project the two rings onto a plane **B.** then count the number of nodes using the convention shown in (c) and divide the final number by two to get the linking number. [Fig. 2.6 from (7), with permission (Appendix A)]

In order for a DNA molecule to be (+) sc, its Lk must larger than Lk_m and in order to be (−) sc, its Lk must be smaller than Lk_m. To compare the level of supercoiling between two different circular DNA molecules, it is prudent to also consider the slight amount of supercoiling that is required to seal the ends of the DNA. Thus, it is necessary to define a second quantity, Lk^0, which is called the hypothetical linking number, and is the number of base pairs divided by the helical pitch without any rounding, i.e. it does not have to be an integer:

$$Lk^0 = \frac{N}{10.5} \qquad [1.3.2]$$

An important indicator of the absolute level of supercoiling of a DNA molecule is ΔLk, which is the difference between the molecule's actual and relaxed linking number:

$$\Delta Lk = Lk - Lk^0 \qquad [1.3.3]$$

Because the torsional stress introduced into a DNA molecule by additional links scales inversely with the number of base pairs, a useful quantity to allow the comparison of torsional stress between molecules of different lengths is the specific linking difference (σ):

$$\sigma = \frac{\Delta Lk}{Lk^0} \qquad [1.3.4]$$

There are two ways that supercoiling can manifest in DNA. The first is by the introduction or removal of twist (Tw) and the second is by the introduction or removal of writhe (Wr). As a DNA molecule becomes increasingly supercoiled, the helical pitch will increase or decrease up to the so-called buckling transition. At the buckling transition, which is dependent on the length of the DNA, it becomes more energetically favorable for the double helix to buckle and begin to adopt a superhelical structure that is generally plectonemic (Figure 1.2.3). The change in helical pitch is defined as twist and the change

in superhelical structure is defined as writhe. The linking number of a DNA molecule is the sum of its twist and writhe:

$$Lk = Tw + Wr \qquad [1.3.5]$$

In a closed circular molecule of DNA, the total linking number cannot be changed without breaking chemical bonds, so the linking number is invariant. Thus, any change in twist or writhe must be accompanied by an offsetting change in the other (7,19,20):

$$\Delta Lk = \Delta Tw + \Delta Wr \qquad [1.3.6]$$

The study of DNA topology was revolutionized by the development of DNA agarose gel electrophoresis using the DNA intercalating agent, ethidium bromide, as a fluorescent probe (21-24). Because DNA is negatively charged, it will migrate through an agarose gel when an electric field is applied. The speed at which DNA migrates is related to the shape and size of the DNA molecule. The longer or less compact the DNA, the slower it migrates, so DNA topoisomers, or molecules with different levels of writhe, can be separated via agarose gel electrophoresis (7,22,23).

Figure 1.3.3 shows an agarose gel image of circular plasmid pBR322 which is ~4.5 kbp long. Lane (a) shows DNA directly after purification from a bacterial cell. The bottom band represents negatively supercoiled DNA and the top band represents open circular (nicked) DNA. Nicked DNA is a common by-product of the harsh treatment of DNA during purification and is not usually present *in vivo* at the levels detected in a gel. Lane (b) shows the same plasmid prep that has been nicked and then treated with ligase to repair the nicks. Instead of a single band of DNA that runs with the nicked, open circular, band from lane (a), five distinct bands are present. Each of these bands contains DNA that has a different level of absolute writhe, or ΔLk. Because positive and negative

writhe of the same degree have the same level of compactness, they migrate together on a gel and cannot be resolved without an additional treatment, described in the following section. The ΔLk values for each band from top to bottom are: 0, ±1,±2,±3, and ±4. Each band grows fainter and thus less populated by DNA as the absolute ΔLk increases. This is because treatment of nicked circular DNA with ligase results in a Boltzmann distribution of topoisomers centered on the relaxed topoisomer band.

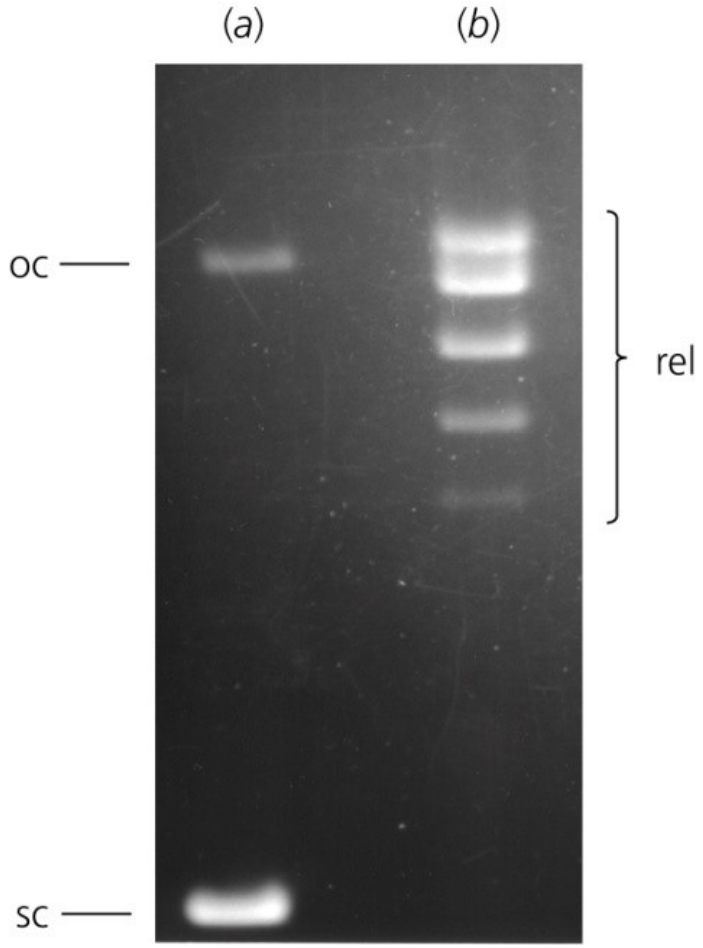

Figure 1.3.3 Agarose gel showing the migration of different topoisomers of circular DNA. (a) DNA from cellular purification. The supercoiled (sc) band runs fastest and the open circular (oc - nicked) band runs slowest (b) The same DNA from (a) that has been nicked and ligated to form an equilibrium distribution of relaxed and slightly supercoiled topoisomers. Topoisomers with the same levels of absolute writhe co-migrate. [Fig 2.11 from (7), with permission (Appendix A)]

1.3.2 The Thermodynamics of Supercoiling

Most commonly used fluorescent DNA stains, such as ethidium bromide, are intercalating agents, which generally have a planar aromatic structure that enables them to become inserted between two base pairs of double stranded DNA, resulting in reduction of the twist of the molecule (7). This reduction in twist is compensated for by an increase in positive writhe. As such, these intercalating agents affect the mobility of DNA on agarose gels.

Since an increase in total writhe is energetically unfavorable, the binding behavior of ethidium bromide to DNA can be used to assess the free energy of supercoiling. Ethidium bromide decreases the total amount of writhe when it binds to negatively supercoiled DNA and increases the total level of writhe when it binds to relaxed or positively supercoiled DNA. Because the lower energy state of DNA is preferred, ethidium bromide has a higher affinity for negatively supercoiled DNA than for relaxed or positively supercoiled DNA. This binding preference was exploited by both Bauer and Vinograd (25) and Hsieh and Wang (26) when they independently used an ethidium bromide titration to determine that, for DNA molecules of several thousand base pairs, the free energy of supercoiling has a quadratic dependence on the extent of supercoiling (7). Therefore the free energy required to achieve a linking difference of ΔLk_i is:

$$\Delta G_i = K \cdot \Delta Lk_i^2 \qquad [1.3.7]$$

A quadratic relationship between free energy and supercoiling suggests that the act of supercoiling is an elastic process. The free energy of supercoiling, including the small amount of supercoiling required to covalently close the DNA molecule (δ), would thus be:

$$\Delta G_i = K \cdot (\Delta Lk_i - \delta)^2 \qquad [1.3.8]$$

The probability of a DNA molecule being in the i[th] topoisomer conformation with linking difference $\Delta Lk_i - \delta$ is:

$$P_i = Ae^{\frac{-(\Delta Lk_i - \delta)^2}{\langle \Delta Lk^2 \rangle}} \qquad [1.3.9]$$

where, δ is the difference between $Lk_m$and Lk^o and $\langle \Delta Lk^2 \rangle$ is the variance of the topoisomer distribution. For the most intense topoisomer ($\Delta Lk_0 = 0$):

$$P_0 = Ae^{\frac{-\delta^2}{\langle \Delta Lk^2 \rangle}} \qquad [1.3.10]$$

Hence, the free energy difference between the i[th] topoisomer and the 0[th] topoisomer is:

$$\Delta G = -RT\ ln\frac{P_i}{P_0} \qquad [1.3.11]$$

so:

$$\Delta G = \frac{RT}{2\langle \Delta Lk^2 \rangle}[(\Delta Lk_i - \delta)^2 - \delta^2] \qquad [1.3.12]$$

Therefore, the proportionality constant from Equations [1.3.7] and [1.3.8] is:

$$K = \frac{RT}{2\langle \Delta Lk^2 \rangle} \qquad [1.3.13]$$

The general expression for the free energy of supercoiling can thus be written:

$$\Delta G = \frac{RT(\Delta Lk - \delta)^2}{2\langle \Delta Lk^2 \rangle} \qquad [1.3.14]$$

In an equilibrium population of closed circular DNA, topoisomers with the same absolute writhe have similar mobility in agarose gels. Hence, all topoisomers, except the band corresponding to linking number Lk_m overlap with one other band, which skews the topoisomer distribution such that its Gaussian shape is not immediately evident. Intercalating agents are useful when separation of the co-migrating topoisomers is

desired. The most commonly used intercalating agent for this purpose is chloroquine, primarily because it is less carcinogenic and thus safer to work with. A concentration of 0.5 – 1.0 μg/mL of chloroquine in a 1% Tris-Acetate EDTA (TAE) agarose gel is sufficient to separate the co-migrating topoisomers (27). Like ethidium bromide, chloroquine introduces negative twist when it intercalates, causing the DNA to compensate with an increase in positive writhe. Thus, relaxed and positively supercoiled DNA will adopt a more compact conformation since their absolute writhe increases, and these bands will migrate faster through the gel. Conversely, negatively supercoiled DNA will adopt a less compact conformation because the addition of positive writhe causes a decrease in absolute writhe. These bands will then migrate more slowly through the gel. The end result of a gel run in the presence of chloroquine is a Gaussian distribution of topoisomers centered on Lk_m with a variance of $\langle \Delta Lk^2 \rangle$ (Figure 1.3.4).

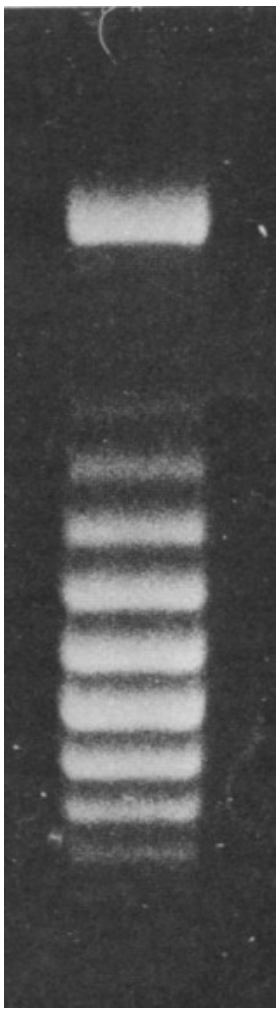

Figure 1.3.4 Agarose gel showing the migration of different topoisomers of circular DNA in a gel that contains chloroquine to resolve topoisomers that have the same levels of absolute writhe in the absence of chloroquine. These bands represent a Gaussian distribution of DNA topoisomers. [adapted from Fig. 2.19 from (7), with permission (Appendix A)]

1.3.3 Knots and Catenanes

An additional topological concern for the cell is the creation of DNA knots (28) and linkages, known as catenanes, which are frequent byproducts of the replicative process itself (7,29,30). As a new molecule of DNA is formed from a circular parental DNA molecule, the new molecule and the parent molecule are topologically linked in a "precatanane" state which, if not resolved by the end of the replication process, will result in two chromosomes that are linked (Figure 1.3.5). If this linkage is not removed prior to cell division, it is impossible for each of the daughter cells to obtain the proper number of chromosomes, most likely resulting in a fatal outcome.

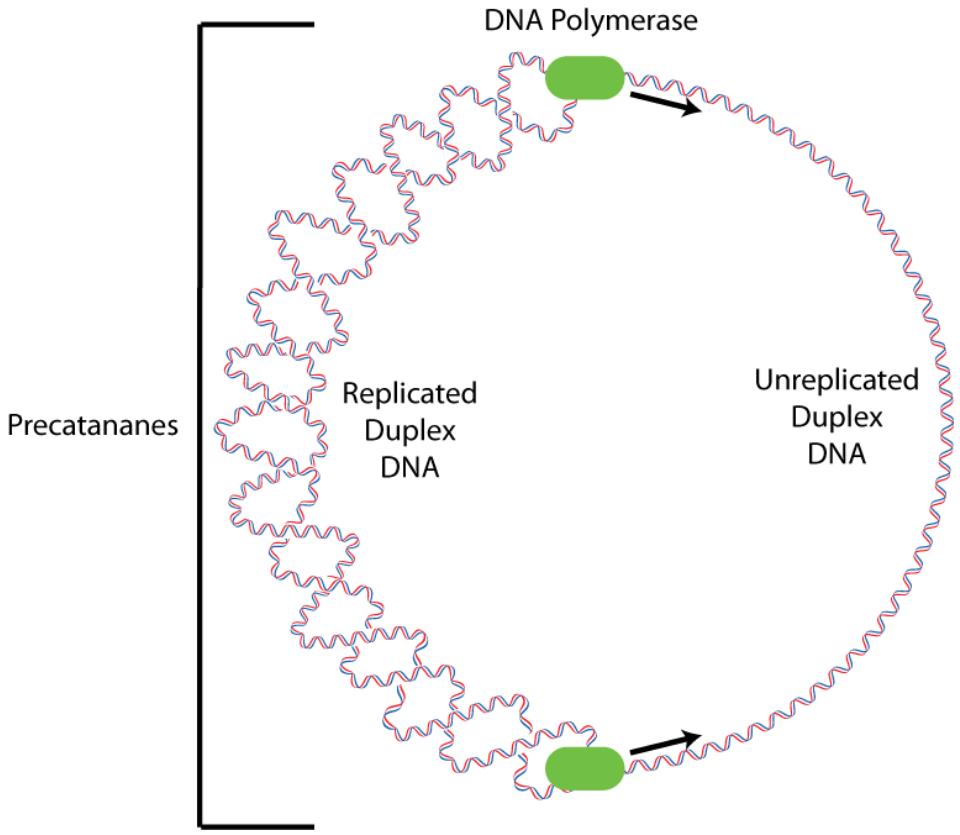

Figure 1.3.5 Illustration of precatenane creation during circular DNA replication. If the precatenanes are not resolved prior to cell division, the new DNA chains will be linked the daughter cells will not receive the proper complement of chromosomes.

1.4 The Discovery of Topoisomerases

In 1968, a mistake by James Wang during the purification of intracellular phage λ DNA rings produced a peculiar sample. While most purified circular DNA was predominately (−) sc, this sample was predominately relaxed. Since all previous and subsequent preparations of this particular DNA molecule in the same lab resulted in the expected predominance of (−) sc DNA, this particular sample was conspicuously unusual. A review of the experimental technique that resulted in this atypical sample revealed that while typical purifications of this DNA were done at 0°C, the high speed centrifugation step of this particular DNA purification was accidentally performed at 20°C and the sample was centrifuged for 2.5 hours rather than the usual 20 minutes. As a result, the DNA had been in contact with the cell extract for a longer period of time and at a higher temperature (15).

While many researchers would have attributed this anomalous relaxed DNA to some mundane source and gone on to purify the DNA "correctly" to carry out the original experiment, Wang decided to investigate this aberration. He had several hypotheses regarding what could have gone wrong, but extensive biochemical testing of the relaxed DNA as well as the cell extract with which it had been in contact during ultracentrifugation revealed that every one of his hypotheses was incorrect: the relaxed DNA was not a result of nicking by endonucleases, nicking by endonucleases followed by ligation by DNA ligase, the creation of a short track of single stranded DNA, or the binding of an intercalating protein. The only other possibility that was considered was the existence of a new sort of protein that creates transient breaks in DNA and then reseals them. However, the idea of a new protein was initially rejected because it seemed

unlikely that a single protein would have simultaneous DNAse and ligase function, while not requiring any sort of energy storing molecule such as ATP or NAD^+ (15).

As it turns out, Wang was right. He had discovered a topoisomerase, which he named ω protein. He postulated that ω protein functioned by breaking the DNA backbone and using that energy to create a covalent bond between the DNA and the protein. He further suggested that the energy necessary to reseal the DNA lesion was supplied by breaking the covalent bond between the protein and the DNA. He published these findings in 1971, but it was five years before this bond swapping mechanism, known as transesterification, was substantiated and ten years before the gene that encodes this protein, now known as *E. coli* topoisomerase I (Topo I) was discovered (15). Shortly after the discovery of ω protein, a second new protein, calf-thymus swivelase (later renamed eukaryotic Topo I) was discovered in mouse nuclear extracts. This swivelase could relax both positive and negative supercoils, which was an important discovery because it could explain how the positive supercoils ahead of the replication fork could be relaxed, thereby reducing the torsional resistance to processivity of the replication machinery (21,31). At last there was a solution that could rescue the proposed double helix structure and its semiconservative replication mechanism, just as Watson and Crick had predicted there would be. However, the problem of replicating circular DNA still remained. The solution to this problem would be found several years later in 1976 when DNA gyrase was discovered (21,32). This remarkable protein was found to be capable of both introducing negative supercoils and decatenating linked DNA molecules.

1.5 The DNA Topoisomerases

DNA Topoisomerases are a family of enzymes, including ω protein (now known as prokaryotic Topo I, a type IA topoisomerase), calf-thymus swivelase (now known as eukaryotic Topo I, a type IB topoisomerase), and DNA gyrase (a type IIA topoisomerase), that regulate the topology of DNA in a cell. Because of their critical roles in maintaining the genomic integrity of organisms, topoisomerases are vital and universally conserved; every organism has at least two different topoisomerases, a type I and a type II. Topoisomerases play an essential role in cell division and are up regulated in rapidly dividing cells. Because disrupting the action of topoisomerases can, at minimum, arrest cell division and will possibly bring about cell death, these proteins are extremely popular and potent anti-cancer drug targets. Also, bacterial topoisomerases are the targets of a common broad-spectrum class of antibiotics, the quinolones, which function as prokaryotic type II topoisomerase poisons.

1.5.1 Type I Topoisomerases

Although *E. coli* Topo I and eukaryotic Topo I are both type I topoisomerases, their mechanisms are actually quite different. Their main similarity is the capacity to cleave only one strand of DNA and relegate that strand via a completely ATP independent mechanism. The type I topoisomerases are subdivided into three classes based on their functional and structural differences. Bacterial Topo I (including *E. coli* Topo I, previously known as ω protein), bacterial Topo III, and eukaryotic Topo III are a few members of the subclass known as the type IA topoisomerases. These proteins, with the exception of a unique topoisomerase found only in hyperthermophilic archaea and

bacteria, called reverse gyrase, are only capable of relaxing negatively supercoiled DNA. Type IA topoisomerases function by nicking one strand of double stranded DNA and separating the two ends of the broken strand such that the second strand can pass through the lesion (Figure 1.5.1A). Because some of these topoisomerases, the Topo IIIs, are capable of moving one strand through another, they are also able to decatenate linked DNA rings if one of the molecules contains a nick.

Reverse gyrase is found in the vast majority of hyperthermophilic archaea and bacteria (21). It is a particularly unusual type IA topoisomerase because in addition to the topoisomerase I domain, it also contains a helicase domain. Helicases are ATP-dependent enzymes that are responsible for unwinding DNA. Because reverse gyrase contains a helicase ATP binding domain, it has the unique ATP-dependent ability to introduce positive supercoils. In addition to the generation of positive supercoils, reverse gyrase also has the ability to perform the single strand nick-passage reaction typical of other type IA topoisomerases. Reverse gyrase is the only type I topoisomerase that can use ATP. It is believed that the exclusive presence of reverse gyrase in hyperthermophilic organisms is due to the increased instability of the DNA double helix at high temperatures. At high temperatures, it is thought that maintaining the DNA in a perpetually overwound state favors genome stability (33).

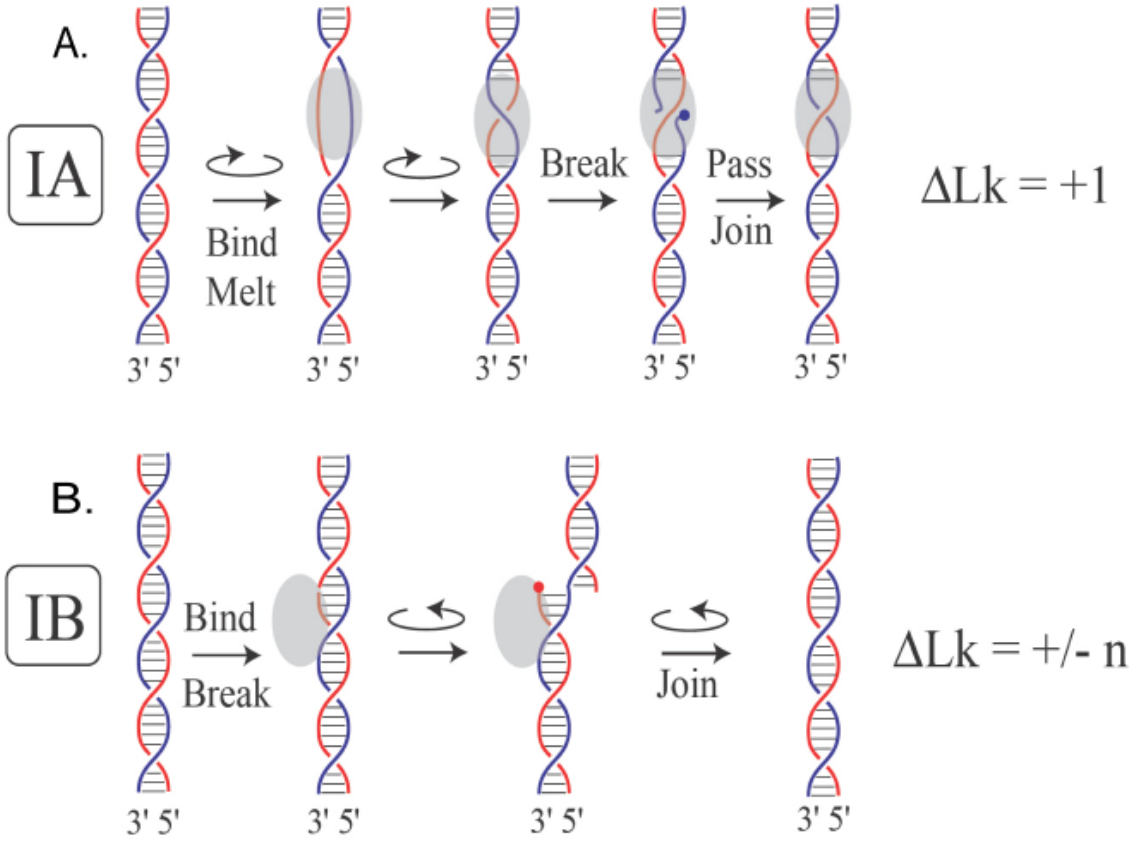

Figure 1.5.1 Mechanism of the type I topoisomerases. **A.** Type IA topoisomerases nick one strand of DNA and physically move the second strand through the nick. These topoisomerases can also decatenate linked DNA if one of the two molecules contains a nick. **B.** Type IB topoisomerases nick one strand of duplex DNA and the other strand undergoes a controlled rotation around the intact phosphate backbone. [Reproduced from Fig. 1 from (34), with permission (Appendix A)]

Eukaryotic Topo I is a type IB topoisomerase. Type IB topoisomerases are structurally and functionally distinct from type IA topoisomerases (21). Type IB topoisomerases are capable of removing both positive and negative supercoils. They function by nicking one strand of double stranded DNA and allowing the other strand to perform a controlled rotation around the intact backbone (Figure 1.5.1B). As such, type IB topoisomerases do not physically engage in strand passage and therefore do not have the decatenase activity on nicked DNA like the type IA topoisomerases. Because neither type of enzyme (with the exception of reverse gyrase) requires or uses ATP or any other energy storing molecule, they use only the torsional energy already present in the DNA topology to relax supercoils. Also they are incapable of removing catenanes to below equilibrium values (35).

Type IB topoisomerases are extremely effective anticancer drug targets. Every eukaryotic organism encodes at least one type IB topoisomerase and for some invertebrates, and all vertebrates, the enzyme is essential (36). The drug camptothecin and its chemical derivatives specifically poison type IB topoisomerases by reversibly inhibiting relegation of the cleaved DNA strand (36,37). Camptothecin-derived drugs tend to produce double-stranded breaks in DNA, perhaps caused by the accumulation of (+) supercoils ahead of the replication machinery or aberrant repair of enzyme-mediated DNA lesions (38). The success of cancer treatment using camptothecin-derived drugs to target type IB topoisomerases has triggered a broad search for other chemical compounds that also inhibit these enzymes. Several compounds isolated through this search are currently in the drug development stage, with many already in clinical trials, making the type IB topoisomerases a very popular family of enzymes to study (17).

A third subclass of type I topoisomerases has recently been characterized, the type IC topoisomerases (33). This subfamily currently only contains one member, topoisomerase V. Topo V has only been found in a particular type of archaea and possesses the unique ability to repair abasic DNA lesions (33,39). Topo V was originally characterized as a IB topoisomerase because it utilizes a similar controlled rotation mechanism as the IB topoisomerases. However, recent studies have shown that Topo V is structurally distinct from the IB topoisomerases and the mechanism is only superficially similar to that of the IB topoisomerases (33).

1.5.2 Type II Topoisomerases

Unlike the type I topoisomerases, the second class of topological enzymes, type II topoisomerases, catalyze ATP-dependent DNA topology manipulation. Like the type I topoisomerases, type II topoisomerases are also divided into two subclasses, types IIA and IIB. Type IIA topoisomerases are the most broadly dispersed topoisomerase family; they can be found in almost every single organism from viruses to eukaryotes with few exceptions (33,40). These enzymes use a two-gate mechanism to manipulate DNA topology in which the topoisomerases cut both strands of one segment of DNA (called the gate, or G-segment) and pass a second segment (called the transfer, or T-segment) through the transient double strand break via an ATP-dependent mechanism (Figure 1.5.2) (41-44). One of the gates is responsible for the binding and cleavage of the G-segment DNA, providing a path for the T-segment to pass through the G-segment and into the interior cavity of the protein, where it then exits through the second protein gate. The closing of the ATP clamp yields a two gate mechanism that results in unidirectional strand passage (33,45).

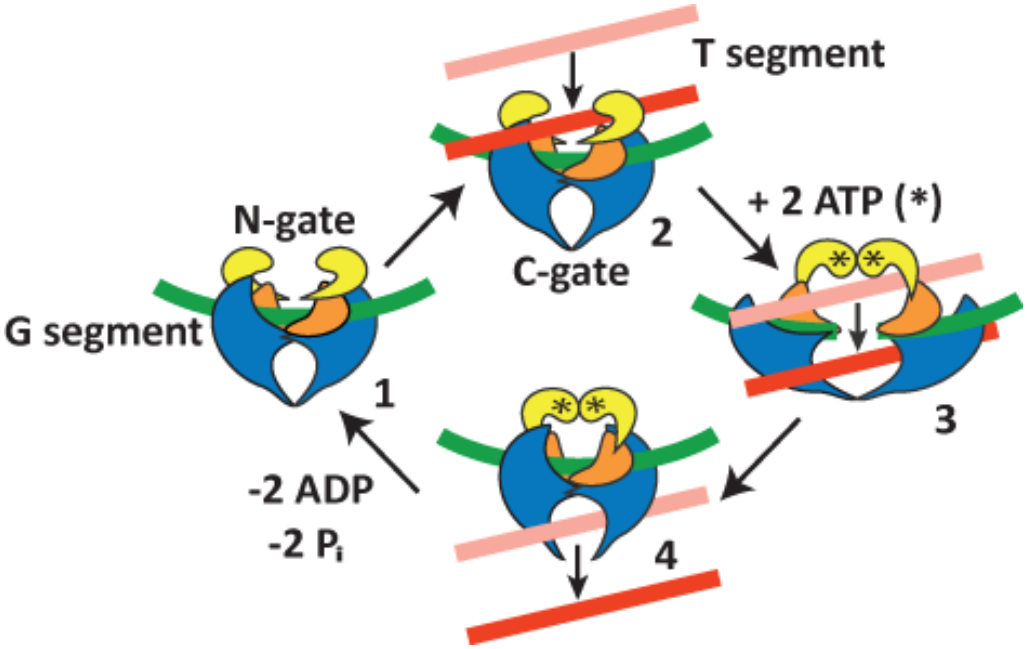

Figure 1.5.2 Core mechanism of type II topoisomerases. (1) The topoisomerase binds G-segment DNA (green) (2) The topoisomerase binds T-segment DNA (Red, pink to red designates motion) (3) The G segment is cleaved and when ATP is bound, the protein undergoes a conformational change that causes the ATP clamp to close and the G segment to be separated. (3) The T segment passes through the G segment and exits the molecule. (4) The products of ATP hydrolysis are released and the protein resets for another round of strand passage. [Adapted from Fig. 3 from (45)]

The type IIA topoisomerases are capable of relaxing and introducing supercoils as well as generating and removing knots and catenanes. Type IIA topoisomerases play a fundamental role in chromosome segregation during cell division by unlinking catenated sister chromatids, thereby enabling daughter cells to receive the proper complement of chromosomes (41). They are also likely required to reduce the level of DNA knotting that is expected in highly compacted DNA, which would be lethal if allowed to accumulate (46-49). Because type IIA topoisomerases pass an intact double-stranded segment of DNA through a second double-stranded segment, they change the *Lk* of the molecule(s) by steps of ± 2.

Type IIA topoisomerases are able to use the energy of ATP to perform strand passage in situations that will preferentially remove knots, catenanes, and supercoils, thus coupling ATP hydrolysis to a shift in the topological equilibrium towards topology simplification (7,27,35,50). The exact mechanism underlying the coupling between ATP hydrolysis and topology simplification remains unknown, but several plausible models have been proposed, as described in the following section. A distinctive type IIA topoisomerase, bacterial DNA gyrase, has the unique ability to introduce (−) supercoils instead of relaxing them. Gyrase is the only known protein that can introduce (−) supercoils into intact duplex circular DNA (21). This distinctive ability of gyrase arises from its ability to form a left-handed wrap of DNA around itself prior to strand passage so that when strand passage occurs, the left-handed wrap will be transformed into a right-handed superhelical crossing, resulting in the introduction of a single (−) supercoil (Figure 1.5.3).

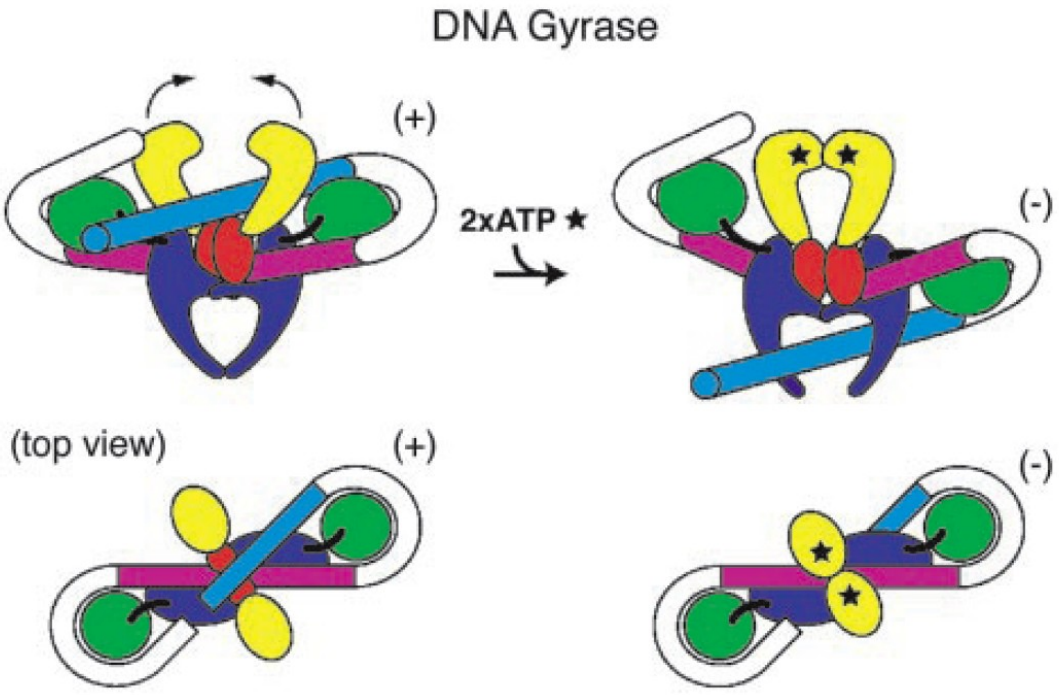

Figure 1.5.3 Mechanism of DNA gyrase. Gyrase wraps G-segment DNA around itself to create a (+) crossing where the G- and T-segments are part of the same DNA molecule. When strand passage occurs, the crossing changes sign from (+) to (-) and a ΔLk of -2 is introduced into the molecule. [Reprinted from Fig. 4 from (51), Copyright (2004) National Academy of Sciences, USA. Permission not required]

Although the type IIA topoisomerases share the same core mechanism and have a high degree of homology, there are some notable differences among the members of this family of enzymes that lead to specialized cellular functions. For example, one of the bacterial type IIA topoisomerases, Topo IV, shows a particular affinity for relaxing (+) supercoils and decatenating circular DNA molecules. A cellular homolog of Topo IV, DNA gyrase, is also able to decatenate circular plasmid DNA molecules, but it shows nowhere near the decatenase capabilities of Topo IV. Furthermore, as previously mentioned, gyrase has the unique ability to introduce (−) sc into closed circular DNA molecules due to its ability to wrap a DNA molecule around itself. It is believed that the differences between these two enzymes can be traced to differences in the C-terminal domains (CTDs) of each of the proteins. Mutation or removal of the gyrase CTD causes it to retain its decatenase activity but completely lose its supercoiling ability. Likewise, mutation or removal of the Topo IV CTD results in loss of ability to remove (+) supercoils (33).

Like bacteria, vertebrate cells also possess two complementary type IIA topoisomerases: Topo IIα and Topo IIβ (36). While Topo IIα is essential and is mainly expressed in replicating cells, Topo IIβ is nonessential and is present in both replicating and nondividing cells. Though it is classified as a nonessential enzyme, the lack of Topo IIβ has been linked to improper neural development and transcription regulation. These topoisomerases also contain CTDs, but they are very dissimilar from the bacterial CTDs, are poorly conserved, and typically unstructured. However, like Topo IV, Topo IIα relaxes (+) sc DNA much more efficiently than (−) sc DNA, while Topo IIβ displays a similar efficiency in relaxing both types of supercoils (52). Interestingly, a Topo IIβ

chimera with its CTD replaced by that of Topo IIα is able to confer viability in the absence of a native Topo IIα. This result suggests that even though the CTDs of these topoisomerases are largely unstructured and harbor scant resemblance to those of their bacterial cousins, these domains may still be responsible for the substrate specificity and divergent cellular roles of Topo IIα and Topo IIβ. Like Topo IIβ, other eukaryotic type IIA topoisomerases, such as the Topo IIs from yeast and *Drosophila*, show no substrate specificity indicating that their CTDs are likely not involved in differentiating supercoil handedness in these enzymes (33). Further investigation of the specific roles and functions of the type IIA topoisomerase CTDs is necessary to fully comprehend the complexities of and differences among these beguiling and intricate enzymes.

In addition to being largely essential and nearly universally conserved, type IIA topoisomerases also have enormous clinical relevance. Gyrase and Topo IV are popular targets of a very potent class of broad spectrum antibiotics known as the quinolones. The quinolones, including the commonly prescribed drugs ciprofloxacin, moxifloxacin, and levofloxacin, function as specific bacterial type II topoisomerase poisons that show more than three orders of magnitude decreased toxicity toward eukaryotic type II topoisomerases (36). These compounds stabilize the DNA cleavage complex and prevent the topoisomerase from re-ligating the cleaved DNA segment, which leads to the accumulation of double stranded DNA lesions when topoisomerase cleavage complexes are encountered by the cell's replication or transcription machinery and the topoisomerase is dislodged from the DNA. In short, these drugs transform essential protective DNA enzymes into agents of toxic DNA damage. Double stranded DNA breaks are usually toxic if they cannot be repaired. As a result, double stranded lesions

commonly lead to cell death (36). Current research is underway to modify the base quinolone structure to produce even more potent and specific antibacterial agents and to overcome the quinolone resistance that has developed in some bacterial strains.

Like the type IB topoisomerases, type IIA topoisomerases are also important anticancer drug targets. There are two classes of anticancer type IIA topoisomerase targeting drugs: Topo II poisons and Topo II inhibitors. Topo II poisons lead to the accumulation of DNA breaks by freezing the Topo II-DNA cleavage complex and preventing relegation of the cleaved DNA strands. This functionality is similar to that of the antibacterial quinolones. Examples of clinically relevant Topo II poisons include: etoposide, doxorubicin, and mitoxantrone (53). Conversely, compounds that inhibit the catalytic activity of the Topo IIs without causing a buildup of DNA breaks and cleavage complexes are called Topo II inhibitors. These inhibitors work by, for example, trapping the topoisomerase in a state that renders it incompetent for DNA binding (53). Examples of clinically relevant Topo II inhibitors are the bisdioxopiperazines, including ICRF-159, ICRF-187, and MST-16. These compounds block Topo II from completing its catalytic cycle much as binding to non-hydrolysable ATP analogs does (53). Unfortunately, few Topo II inhibitors show promise in becoming clinically viable anticancer drugs, as all of the presently identified compounds have cellular targets in addition to Topo II. This is a developing research area (53).

The second, and less well characterized, subclass of type II topoisomerases are the type IIB topoisomerases. Though they share a similar core strand passage mechanism, type IIA and IIB topoisomerases are structurally, biochemically, and evolutionarily distinct (21,54-56). The only known type IIB topoisomerase is Topo VI, and it is found in

archaea and some plants (21). There is very little sequence or structural homology between the IIA and IIB topoisomerases, though they have similar functions.. However, although Topo VI requires ATP, it does not share the ability to simplify DNA topology with its type IIA counterparts (56).

1.6 Topology Simplification by Type IIA Topoisomerases

In 1997, Rybenkov *et al.* (35) showed that non-supercoiling type IIA topoisomerases (i.e., all type IIA topoisomerases with the exception of DNA gyrase) simplify the global topology of DNA, shifting it away from an equilibrium distribution of catenanes, knots, and supercoils toward a less entangled overall topology. Furthermore, Rybenkov and colleagues showed that the relative extent of topology simplification by each topoisomerase was the same for knots, linkages, and supercoils (35). In other words, an enzyme that is two times better than another enzyme at removing knots is also two times better at relaxing supercoils and unlinking catenanes. This indicates that all types of topology simplification arise from the same mechanism, so a measure of only one of the three types of topology simplification will give insight into the overall topology simplification activity of the enzyme. Supercoil relaxation by three type IIA topoisomerases that span the range of documented topology simplification abilities are shown in Figure 1.6.1A (50). A type I topoisomerase is also included to show an equilibrium distribution of topoisomers. As described in section 1.3.2, this gel was run in the presence of chloroquine, so each band contains a unique topoisomer. The center band in each distribution contains relaxed DNA ($\Delta Lk = 0$) and the bands above and below the zero band contain $\Delta Lk = \pm 1, \pm 2$, and so on. The narrower the topoisomer distribution, the further the topoisomerase has compressed the distribution from its equilibrium width.

Figure 1.6.1B shows a plot of the normalized intensity of each topoisomer band vs. location on the gel, fit with a Gaussian. The parameter typically used to quantify the narrowing of the topoisomer distribution, *R*, is the ratio of the variance of the equilibrium DNA population to the variance of a topoisomerase treated DNA population..

The ability of type IIA topoisomerases to shift global topology away from equilibrium implies that they must somehow couple topology sensing to strand passage in order to achieve preferential simplification of knots, catenanes, and supercoils. Since type IIA topoisomerases consume ATP, conservation of energy is not violated, but the detailed mechanism by which the energy of ATP hydrolysis is coupled to topology sensing, and thus, topology simplification remains elusive (27). Specifically, it is unclear how an enzyme that acts on the scale of nanometers is able to assess the global topology of DNA. How is the enzyme capable of below equilibrium catenane removal? If a type IIA topoisomerase only interacts with a single DNA crossing, how is it able to determine that a strand passage event would result in the removal, rather than the creation, of a linkage (Figure 1.6.2)?

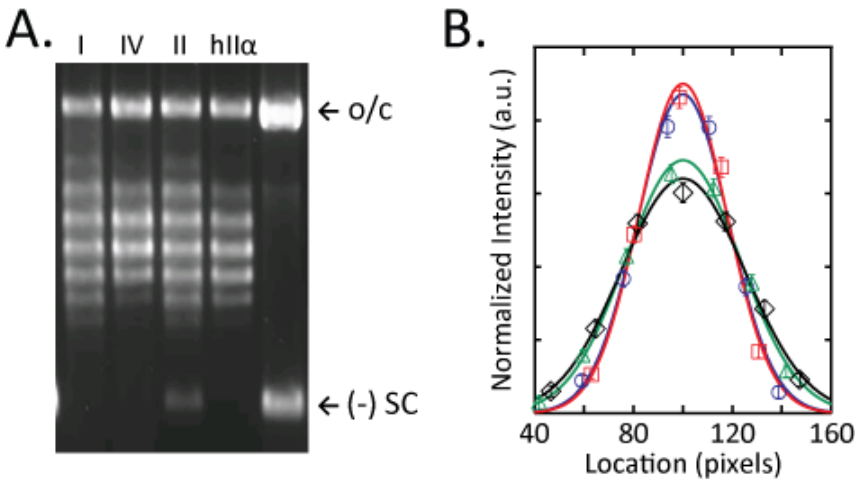

Figure 1.6.1 Topology simplification by type IIA topoisomerases. **A.** An agarose gel containing chloroquine showing the topoisomer distributions for a type IB topoisomerase (I) and three different type II topoisomerases: Topo IV (IV), yeast Topo II (II) and human Topo IIα (hIIα). Also shown is the starting material in lane 5. **B.** Distributions of topoisomers for each topoisomerase fit to a Gaussian: Topo IV (red squares), human Topo IIα (blue circles), yeast Topo II (green triangles) and Topo I (black diamonds).

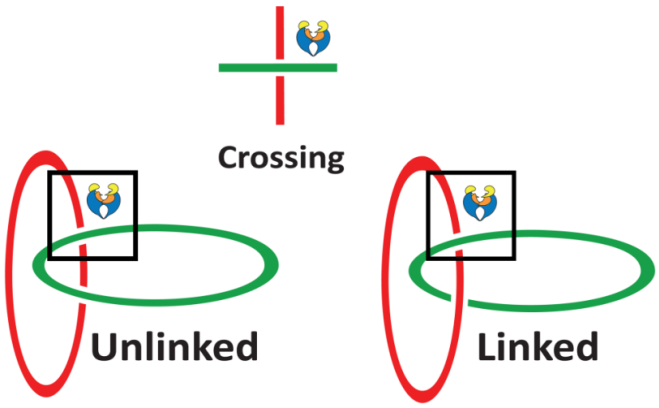

Figure 1.6.2 How can a topoisomerase acting on the scale of a single DNA crossing asses the global topology of the much larger DNA molecule?

Several mechanistic models of topology simplification by type IIA topoisomerases have been proposed (35,57-61), though to date the experimental evidence distinguishing them has been equivocal and, at times, contradictory (62). A tracking model, which was conceived by Rybenkov *et al.* (35) upon their discovery of this phenomenon, proposes that the enzyme binds to a DNA crossing and tracks along the DNA to trap T-segments that are catenated or knotted (35). However, an experiment that placed "roadblocks" in the form of tightly bound proteins at several locations along supercoiled circular DNA did not affect non-equilibrium supercoil relaxation (27). This showed that it was not required for the topoisomerase to "track" along the DNA in order to ensnare linked T-segments. A three segment binding model postulates that the topoisomerase binds two potential T-segments prior to selecting one for strand passage based on local geometry (61). However, this model predicts an overall asymmetric removal of supercoils, which other studies have failed to detect (27). Three competing and untested possibilities are the bend angle, hooked juxtaposition, and kinetic proofreading models, described below.

The authors of the bend angle model, originally proposed by Vologodskii *et al.* (59) and later expanded upon by Klenin *et al.* (60), postulate that non-supercoiling type IIA topoisomerases introduce a sharp bend in the G-segment DNA that localizes the active site of the enzyme to the interior apex of the bent DNA (Figure 1.6.3). The bend orients the topoisomerase such that the T-segment binding site of the enzyme tends to point toward the inside of circular DNA, favoring strand passage from the interior to the exterior of the circle. This geometric selection, coupled with the unidirectional strand passage embodied in the two gate mechanism of type IIA topoisomerases, would lead to

preferential unlinking, unknotting, and supercoil relaxation. The authors of the bend angle model further postulate that topology simplification activity scales with the magnitude of the imposed bend angle, providing a mechanistic basis for the observed variation in non-equilibrium simplification activities among different type IIA topoisomerases (27,35). This model has been somewhat supported in the literature by several type IIA topoisomerase-DNA co-crystal structures that show topoisomerase mediated DNA bending by around 150° (63-66). However, because a major tenet of this model is the scaling of topology simplification ability with bend angle, and the bend angles of the crystallized DNA are very similar, these structures do not support the bend angle model if the crystallized topoisomerases are capable of different levels of topology simplification. Of the three topoisomerase-DNA complexes crystallized, two are bacterial Topo IVs and one is eukaryotic yeast Topo II. Topo IVs are expected to be much more capable topology simplifiers than yeast Topo II, though the specific topology simplification activities of the crystallized Topo IVs had not been reported prior to this work (Chapter 2). However, they display a striking sequence homology to *E. coli* Topo IV, which, based on its topology simplification ability, would be expected to have a bend angle a factor of three times larger than that of yeast Topo II.

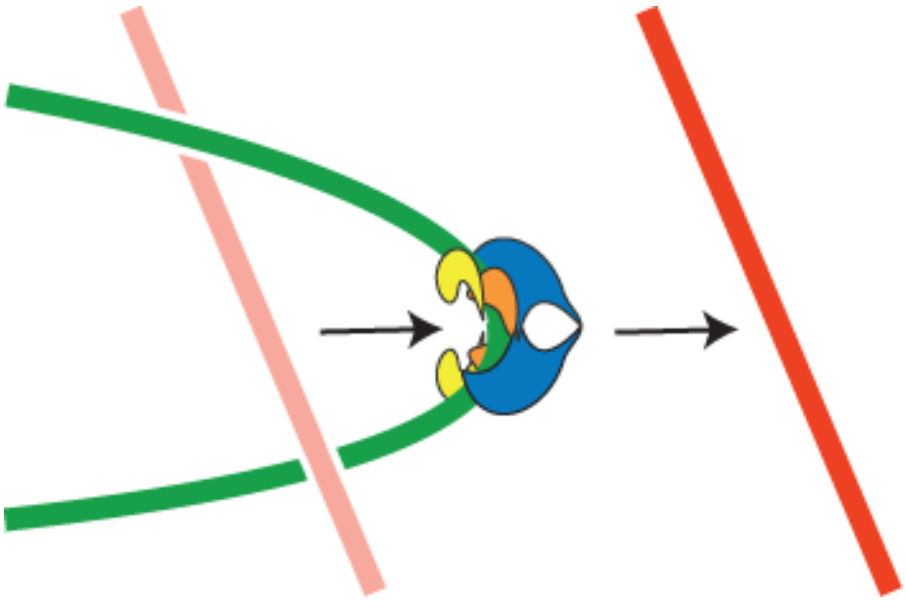

Figure 1.6.3 Illustration of the bend angle model of topology simplification by type IIA topoisomerases. This model postulates that upon binding DNA, the type IIA topoisomerase introduces a sharp bend into the DNA that orients the active site of the protein towards the interior of the bend.

In the experiments detailed in Chapter 3, we directly and indirectly measured DNA bending by type II topoisomerases using the techniques of atomic force microscopy (AFM) and single molecule Förester Resonance Energy Transfer (smFRET), respectively. These measurements were not consistent with the predictions of the bend angle model. Furthermore, one of the two bacterial type II topoisomerases that has been co-crystallized with DNA has an activity larger than yeast Topo II (Chapter 2). The fact that the DNA bend angle established in the crystal structure is so similar to the DNA bend angle imposed by yeast Topo II also suggests that DNA bending alone cannot account for differences in topology simplification abilities between the two proteins.

The authors of the hooked juxtaposition model postulate that type IIA topoisomerases detect and relax specific juxtapositions of catenated, knotted, and supercoiled DNA in which the G- and T-segments are bent towards one another (57). Simulations indicate that strand passage at these hooked juxtapositions is sufficient to produce non-equilibrium topology simplification. However, strand passage at a half hooked juxtaposition, such as proposed in the bend angle model, is not (67-71). This model has not yet been tested.

The kinetic proofreading model suggests that upon binding to G-segment DNA and encountering an initial T-segment, the topoisomerase becomes activated, perhaps by binding one of the two ATP molecules. The model goes on to postulate that the T-segment is then released and strand passage will ultimately only occur if a second T-segment is captured while the enzyme is in the transient active state (Figure 1.6.4) (58,72). As detailed in Chapter 4, this model was tested using magnetic tweezers. In these experiments, a magnetic bead was tethered to the surface of a coverslip by two parallel

DNA molecules and the time to strand passage by *E. coli* Topo IV was measured for a range of different DNA-bead geometries, as well as a number of different local geometries between the two DNA molecules, mediated by rotation of the bead. Simulations of DNA in these different configurations were performed to characterize the probability of DNA juxtapositions for each imposed rotation. These probabilities were compared to the experimentally determined rate of strand passage for each geometry to determine the nature of the relationship between the probability of DNA segment collision and the rate of strand passage.

Though there are simulations in support of each of the three models, prior to the experiments detailed in Chapter 3 and Chapter 4, none of them had been tested to determine whether the theoretical predictions could be verified experimentally. My work has focused on testing these models to determine which predictions, if any, are experimentally supported. In this thesis, I will describe how we used several different single-molecule techniques to test the bend angle and kinetic proofreading models.

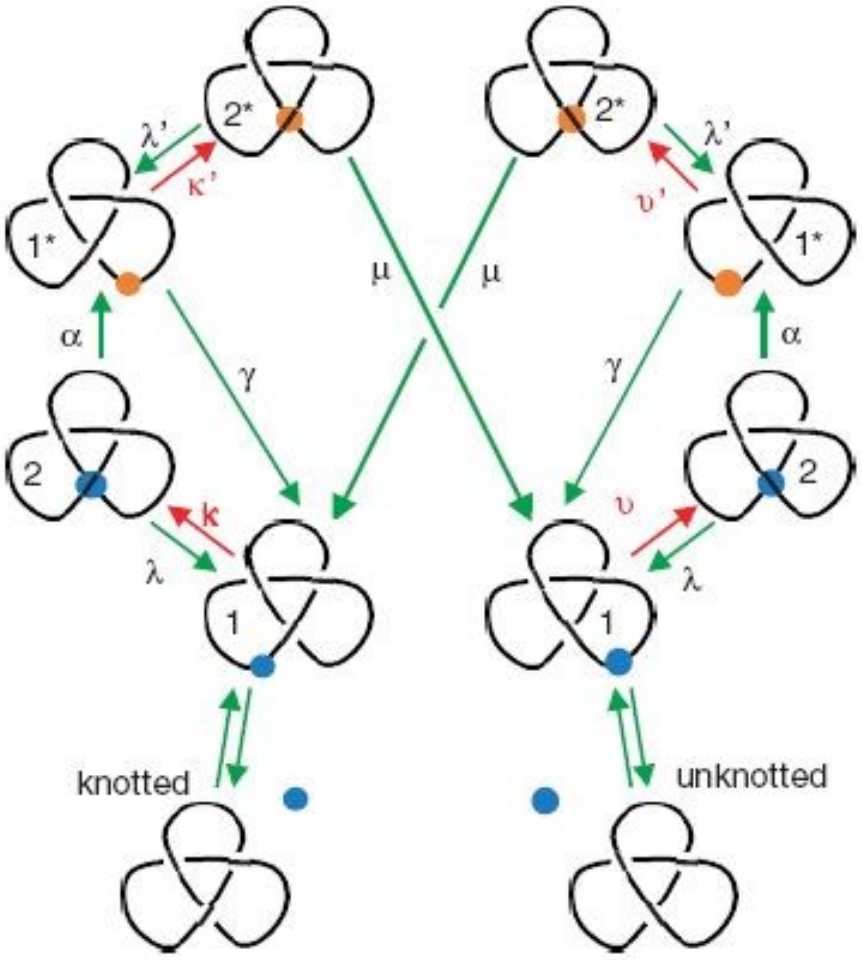

Figure 1.6.4 Schematic of the kinetic proofreading theory of topology simplification by type IIA topoisomerases. According to this model, the topoisomerase becomes activated upon the first encounter with a T-segment. It then releases the T-segment and if it binds a second T-segment before the protein decays back into the inactivated state, then it will initiate a strand passage event. (The specifics of this model are detailed in Chapter 4) [Fig. 4 from (58), reprinted by permission of Macmillan Publishers, Ltd: *Nature* copyright (2006) (Appendix A)]

Chapter 2: Non-Equilibrium Topology Simplification by Type II Topoisomerases

2.1 Determination of DNA Topology by Agarose Gel Electrophoresis

In addition to being widely used for DNA size determination, agarose gel electrophoresis can also be used to separate DNA molecules in different topological states. Because DNA carries a uniform charge and linear double-stranded DNA is relatively free of structural complications that might affect migration, linear DNA molecules having the same length will co-migrate in an agarose gel and can be resolved in a single band (73). On the other hand, the migration of closed circular DNA molecules depends on both length and topology, so it is possible to identify multiple topoisomers of a closed circular DNA molecule via gel electrophoresis. Supercoils introduced into closed-circular plasmid DNA manifest as writhe. This means that supercoiled DNA molecules are more compact than relaxed DNA molecules, so they are able to travel faster through the agarose matrix. The more supercoiled a DNA molecule is, the faster it will migrate, which allows for the separation of multiple topoisomers. However, because positive and negative supercoiling of the same degree (e.g. ±1, ±2, etc.) compacts the DNA to the same extent, these topoisomers will co-migrate unless an appropriate intercalating agent is used to separate them.

As described in section 1.3.2, the anti-malarial DNA intercalator, chloroquine, is often used to separate topoisomers with the same level of absolute writhe. Chloroquine works by promoting negative ΔTw in the DNA double helix. Because a circular DNA molecule is covalently closed, any addition of twist must be compensated for by an equal and opposite addition of writhe, as shown in Equation [1.3.6]. Thus, the DNA molecules

all migrate within the gel as if they were more (+) sc than they actually are. This has the net result of causing the topoisomers that already have positive writhe to experience a positive ΔWr, making them more compact so that they travel faster through the agarose matrix. On the other hand, DNA molecules that have negative writhe, experience a negative ΔWr and become less compact so that they travel more slowly through the gel. Using chloroquine in this way lifts the degeneracy among the DNA topoisomer bands and allows the full distribution of topoisomers to be resolved, with the relaxed topoisomer band migrating in the center of the distribution (Figure 1.3.4). The bands above and below the center topoisomer band are minus and plus one, respectively, and the ones above and below those are minus and plus two, and so on.

The location and intensity of the topoisomer bands can be fit to a Gaussian curve to determine the variance of the topoisomer distribution (Figure 1.6.1). If the DNA molecules were treated with a type IB topoisomerase or nicked and treated with ligase, the distribution of topoisomers will represent an equilibrium distribution. The variance of a topoisomer distribution created by DNA treated with a type II topoisomerase can then be compared against the equilibrium distribution of topoisomers to determine the level of topology simplification. The ratio of the variance of an equilibrium distribution of topoisomers to the variance of a non-equilibrium population of topoisomers generated by treatment of DNA by a type II topoisomerase (R) is referred to as the level of topology simplification.

2.2 Different Type IIA Topoisomerases Simplify Topology to Differing Degrees

Type IIA topoisomerases have been shown to reduce the topological complexity of DNA by preferentially removing knots and catenanes and reducing the absolute level of supercoiling (27,35). These measures of topology simplification are highly correlated for each type IIA topoisomerase, suggesting that they are likely governed by a single underlying process (35). Thus, supercoil relaxation measurements are sufficient to confirm the non-equilibrium activities of these enzymes (27). In order to verify the non-equilibrium activities of the type IIA topoisomerases used for AFM imaging, we measured supercoil relaxation by Topo IV, yTopo II, and hTopo IIα. The absolute level of supercoiling is reflected in the width of the topoisomer distribution, i.e. the relative abundance of each topoisomer. The topoisomer distribution can be resolved on an agarose gel in the presence of chloroquine as shown in Figure 1.6.1. Individual topoisomers differing by a single linking number (Lk) ran as distinct bands in the gel, the relative intensities of which were plotted to obtain the topoisomer distribution. As previously observed, the distribution of topoisomers was narrower for the type IIA topoisomerases than for Topo I, which generates an equilibrium distribution of topoisomers. The width of the topoisomer distribution is quantified by the variance ($\langle \Delta Lk^2 \rangle$), with reduced absolute levels of supercoiling corresponding to reduced variances. The degree of topological simplification was quantified by comparing the variances of the type IIA topoisomerase distributions with that of the Topo IB distribution. The ratio (R) of the variance of Topo IB to each of the type IIA topoisomerases was consistent with reported values (Figure 1.6.1) (27,35). Topo IV

shifted the topology furthest from equilibrium ($R = 1.9 \pm 0.1$; mean ± SD), hTopo IIα shifted the topology to an intermediate extent ($R = 1.8 \pm 0.1$), and yTopo II shifted the topology the least ($R = 1.12 \pm 0.07$).

2.3 Topology Simplification by Topoisomerases with Reported DNA Co-crystal Structures

In 2007, Dong *et al.* (63) published the first type IIA topoisomerase-DNA co-crystal structure. Type IIA topoisomerases had previously been suspected of DNA bending, and a model had been put forth that posited this hypothetical DNA bending was responsible for the non-equilibrium topology simplification activity of these enzymes (59,60). However, until this crystal structure was published, there was no experimental proof of DNA bending by type IIA topoisomerases.

The reported bend angle imposed on the DNA by yTopo II in this crystal structure (~150°) was similar to the bend angle predicted by the bend angle model for a topoisomerase displaying the topology simplification activity of yTopo II (~100°), which lent credence to this model (59,60,63). However, several type IIA topoisomerase-DNA co-crystal structures have been recently reported that show two bacterial type IIA topoisomerases that bend DNA. These structures, of gram positive *Streptococcus pneumoniae* topoisomerase IV (64) and gram negative *Acinetobacter baumannii* topoisomerase IV (66), both co-crystallized with DNA in a covalently bound cleavage complex, indicate that DNA is bent to a similar degree as in the case of yTopo II (Figure 3.2.1).

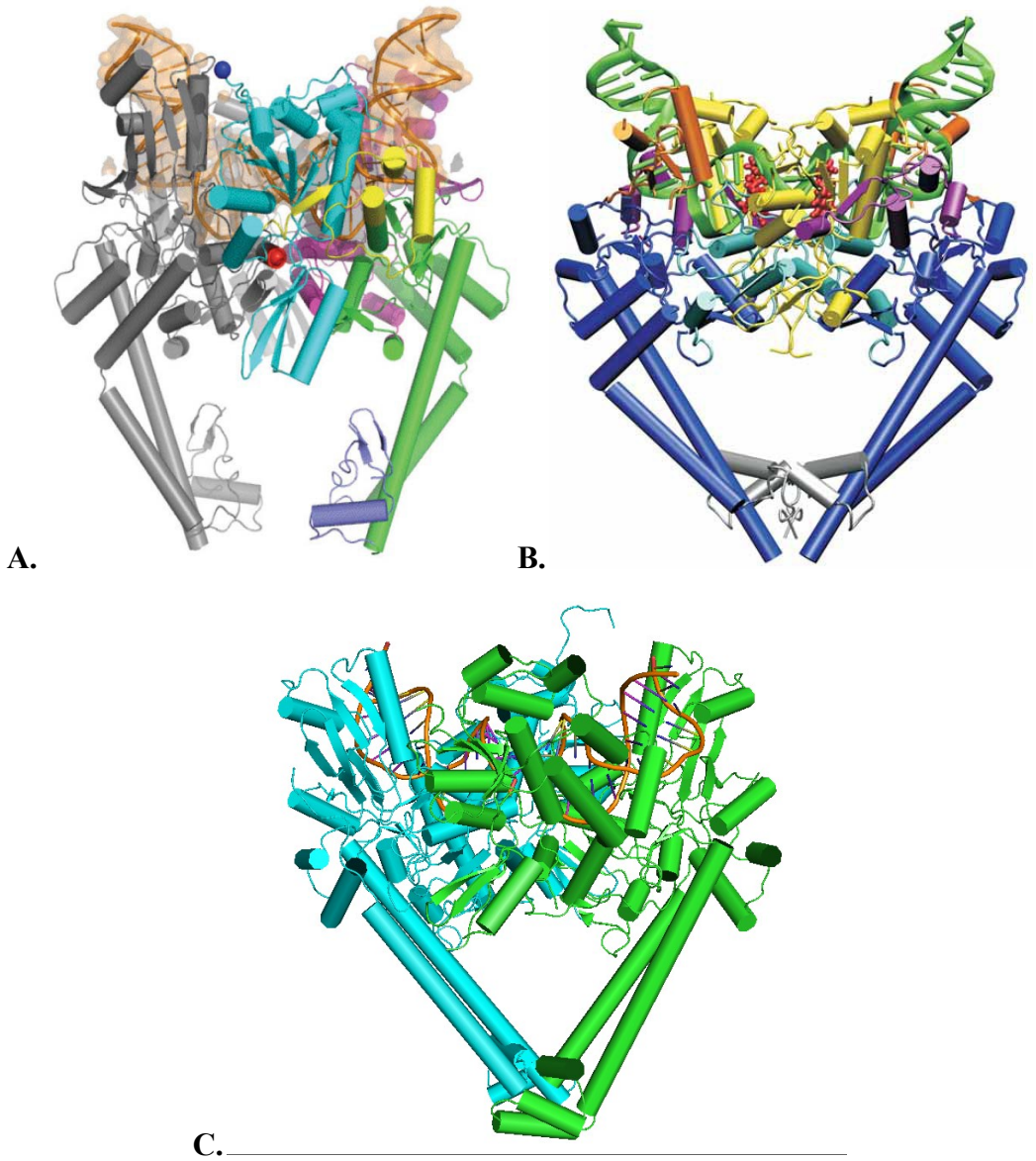

Figure 2.3.1 Type IIA topoisomerases co-crystallized with DNA. **A.** yTopo II, **B.** *Streptococcus pneumoniae* Topo IV, **C.** *Acinetobacter baumannii* Topo IV. All three topoisomerases appear to bend DNA to approximately the same degree, though yTopo II does appear to have a slightly larger bend angle.

As shown in Figure 1.6.1, *E. coli* Topo IV has been shown shift DNA topology the farthest from equilibrium. Because *A. baumannii* Topo IV shares a sequence identity of over 60% with *E. coli* Topo IV, it would be reasonable to predict that the topology simplification activity of these two enzymes would be similar. *S. pneumoniae* Topo IV shares some sequence identity (~25%) with *E. coli* Topo IV, but is actually more similar to *E. coli* gyrase than to Topo IV. Regardless, it would be reasonable to predict that *S. pneumoniae* Topo IV would behave more like another bacterial topoisomerase than a eukaryotic topoisomerase.

To test these predictions, we measured the topology simplification ability of *S. pneumoniae* Topo IV and compared it to the previously measured and reported topology simplification abilities of other type IIA topoisomerases. We found that *S. pneumoniae* Topo IV has a topology simplification activity of $R \approx 1.4 \pm 0.1$. This value is larger than that of yTopo II ($R = 1.12 \pm 0.07$) and is somewhat smaller than hTopo IIα ($R = 1.8 \pm 0.1$) (Figure 2.3.2) (27,35,50). This result is consistent with work we did showing that direct and indirect measurements of DNA bending by type II topoisomerases yield similar DNA bend angle measurements for all topoisomerases studied, regardless of topology simplification activity (see Chapter 3) (50). While DNA bending might not play a key role in determining the full extent of topology simplification by type II topoisomerases, the fact that all studied topoisomerases bend DNA by more than 100° suggests that DNA bending might play some other physiological role. Perhaps DNA bending is part of some conserved mechanism that contributes to the basic level of topology sensing that yTopo II is capable of.

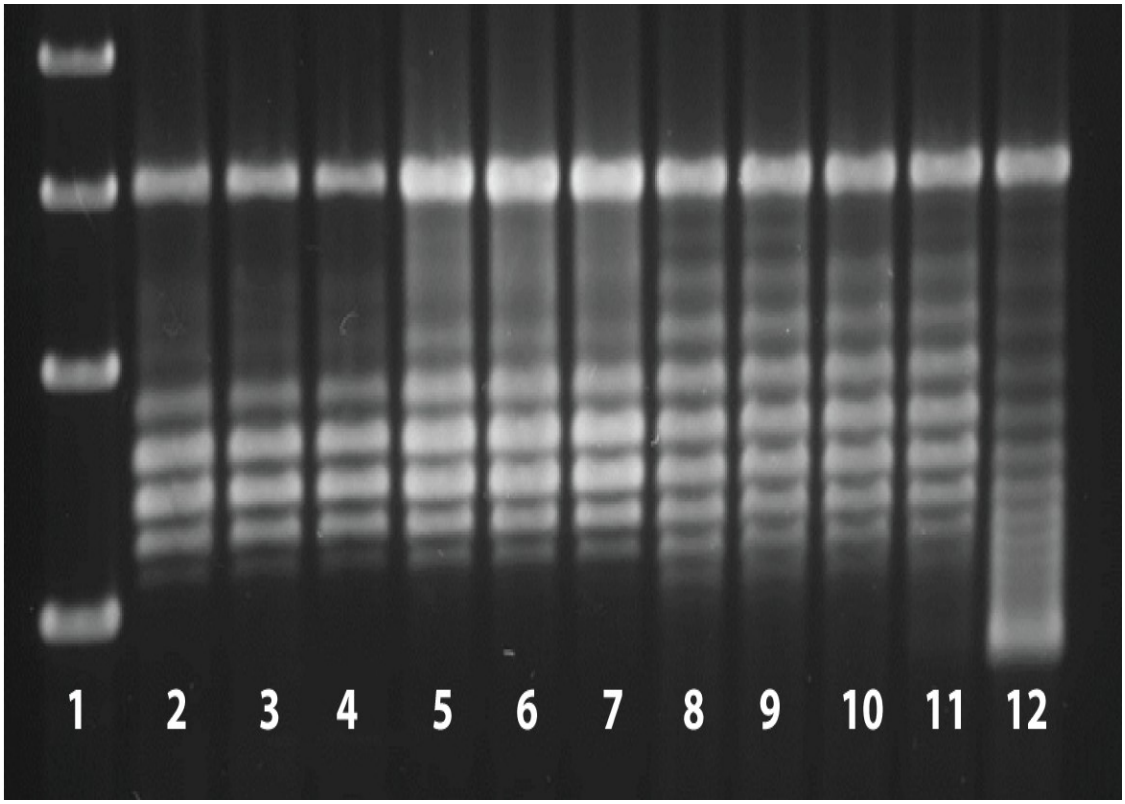

Figure 2.3.2 Topology simplification by *S. pneumoniae* Topo IV. Agarose gel with 1 μg/mL of chloroquine to resolve topoisomers. Lanes 2-4 show a supercoil relaxation reaction of plasmid pBR322 by *E. coli* Topo IV, lanes 5-7 show supercoil relaxation by *S. pneumoniae* Topo IV, and lanes 8-11 show supercoil relaxation by wheat germ Topo I. Lane 1 contains a 1 kb plus ladder (Invitrogen) and lane 12 contains untreated negatively supercoiled pBR322. For *S. pneumoniae*, we found that $R = 1.4 \pm 0.1$. Gels were run under the conditions outlined in the "Relaxation Assays" section of Appendix B.

Chapter 3: Direct Measurement of DNA Bending by Type IIA Topoisomerases: Implications for Topology Simplification

3.1 The Bend Angle Model of Topology Simplification by Type IIA Topoisomerases

The G-segment bend angle model, proposed by Vologodskii *et al.* (59) and expanded upon by Klenin *et al.* (60), postulates that non-supercoiling type IIA topoisomerases introduce a sharp bend in G-segment DNA upon binding (Figure 1.6.3). This bending would tend to be orient the T-segment binding site toward the inside of a circular DNA molecule. This, coupled with the enzyme's unidirectional strand passage could give rise to the preferential unlinking, unknotting, and supercoil relaxation characteristic of type IIA topoisomerases. A main tenet of the bend angle model is that topology simplification activity should scale with the magnitude of the imposed bend angle, providing a mechanistic explanation for the documented variation in non-equilibrium simplification activities among type IIA topoisomerases (27,35).

Recent studies, including structures of gram positive *Streptococcus pneumoniae* topoisomerase IV (64) and gram negative *Acinetobacter baumannii* topoisomerase IV (66), both co-crystallized with DNA in a covalently bound cleavage complex, structures of yeast topoisomerase II (yTopo II) co-crystallized both with noncovalently bound DNA (63) and in a covalently bound DNA cleavage complex (74), and single-molecule magnetic tweezers measurements (75), indicate that DNA is bent by type IIA topoisomerases. Though these studies lend support to the bend angle model, other studies give contradictory results. For instance, recent simulations using an improved worm-like

chain (WLC) model have shown that a sharply bent conformation of the G-segment DNA is not sufficient to reproduce experimental non-equilibrium topology simplification results (67,71). Also, an implication of the bend angle model is that topology simplification activity should depend on DNA circle size. Decreasing the circle size should increase the probability that a bend would orient the active site of the enzyme towards the interior of the circle. This, in turn, would be expected to amplify the effect of the bend angle, thereby enhancing topology simplification activity. However, the non-equilibrium activity of yTopo II and *E. coli* topoisomerase IV (Topo IV) appear to be independent of DNA circle size for circles large enough to adopt more than two topoisomer conformations (27,61). Although these various results either indirectly support or contradict the bend angle model, the specific predictions of the model have not been tested directly (62).

In this study, we used atomic force microscopy (AFM) to image type IIA topoisomerase-DNA complexes and directly measure the bend angles imposed on the DNA by three non-supercoiling type IIA topoisomerases that span the range of topology simplification activity: Topo IV, human topoisomerase IIα (hTopo IIα), and yTopo II, in order of decreasing non-equilibrium topology simplification activity (27,35). We also used single molecule Förster Resonance Energy Transfer (smFRET) to probe the extent of DNA bending by these three topoisomerases. According to the bend angle model, Topo IV, which has the largest simplification activity, should impose the largest bend in DNA, whereas yTopo II, which has the smallest simplification activity, should impose the smallest bend (60). The bend angles imposed on the DNA by each of these proteins measured by AFM and computed from FRET efficiencies were compared to those

predicted by the bend angle model. We found that all three type IIA topoisomerases bent the DNA to a similar degree. Moreover, for each enzyme, with the possible exception of yTopo II, the extent of the bending was less than predicted by the bend angle model, which suggests that G-segment DNA bending is unable to fully account for the topology simplification behavior of these enzymes.

3.2 Methods

3.2.1 Atomic force microscopy (AFM)

Atomic force microscopy is a powerful imaging technique capable of capturing three dimensional topographical images of surfaces with sub-nanometer height resolution (76,77). These images are captured by scanning the surface of a sample with a cantilever that has a very sharp tip with a radius of a few nanometers. As the tip interacts with the surface, either continuously, as in contact mode, or intermittently, as in tapping mode, the deflection of the cantilever is recorded by a laser beam that is reflected off of the cantilever and onto a position sensitive diode (PSD) (Figure 3.2.1). The laser deflection information collected at each point as the tip scans the surface can be translated into the height of the sample at that point (77). As the tip scans a prescribed area of the sample, line by line, the height information collected over that area yields a topographic map of the surface. For most biological samples, tapping mode, as opposed to contact mode, is the preferred method for imaging. This is due to the generally delicate nature of many biological samples. In contact mode, the tip is constantly in contact with the surface and applies a horizontally directed dragging force to the sample as it scans. Conversely, in tapping mode, the cantilever oscillates at near its resonant frequency and only

intermittently comes into contact with the sample, thus minimizing the horizontal forces imposed upon the sample (77). This is a particularly important distinction in the case of DNA imaging by AFM. The widely accepted method for adsorbing DNA molecules onto a surface (typically mica) for scanning utilizes a weak salt bridge generated by magnesium ions between the negative surface of the mica substrate and the uniformly negatively charged DNA molecules. This deposition method has been shown to allow the DNA molecules to fully equilibrate in two dimensions, rather than becoming kinetically pinned in a 2D projection of the DNA's 3D conformation (78). This is of critical importance when quantitative DNA or DNA-protein interaction structural information is desired, as in this study. Further details of the AFM experiments and deposition conditions can be found in Appendix B.

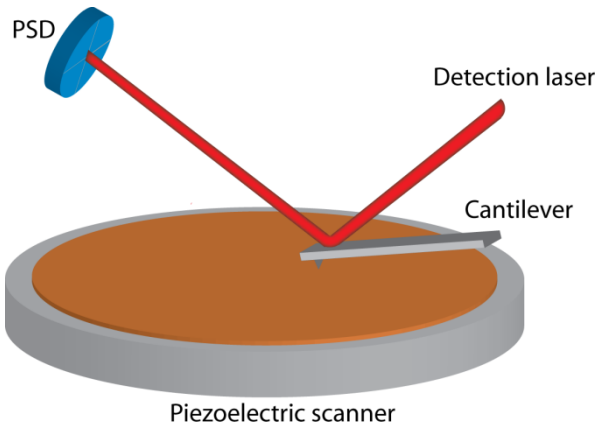

Figure 3.2.1 Diagram of an AFM. The sample is deposited onto a mica surface (brown) and a cantilever with a sharp tip scans the mica as it gently taps the surface while oscillating at close to its resonant frequency. A laser beam is deflected off of the top of the cantilever onto a position sensitive diode (PSD). The laser deflection information can be translated into the height of the sample at that location. Hence, as the tip scans a prescribed area, a topographic map of the mica's surface can be created.

3.2.2 Image analysis

AFM images were flattened to correct for the natural curvature of the mica surface using Nanoscope V software and converted to bitmap files using WSxM software (36). DNA bend angles were measured using three different techniques; Manual tangent overlay, automated tangent overlay, and end-to-end distance (EED) fitting. Manual tangent overlay, was performed as previously described (35,37-39). Briefly, we used the angle measurement tool in ImageJ to measure the angle (ϕ) between two tangent line segments that were drawn along the contour of the ~50 nm DNA fragments emerging from the ~15 nm diameter protein (Figure 3.3.1E and Figure 3.3.3). The bend angle (θ) is defined as $\theta = 180 - \phi$ (Figure 3.3.3). Three types of protein-DNA complexes were identified: enzyme bound to a long substrate (D1 or D2), enzyme bound to a short substrate (D3, D4, or D5), and enzyme bound and joining two short substrates (D3, D4, or D5) (Figure 3.3.2). Protein-DNA complexes were manually selected based on the criteria that only one protein was bound to the DNA, protein was not bound to the ends of the DNA, and the bound DNA did not intersect another DNA molecule. The intrinsic bend angles of free DNA (substrate D6) were determined as described (35,38). Briefly, 15 nm circles were drawn near the middle of each DNA molecule to simulate bound protein and angles were measured as described above for actual protein-DNA complexes. The measured angles (ϕ) determined for unbound DNA were all measured to be less than 180°. Plotting and statistical analysis was performed with IGOR Pro software (Wavemetrics, Oswego, OR). Data were statistically analyzed using the Analysis of Variance (ANOVA) and Tukey Tests in IGOR Pro. Each subset of data for Topo IV, corresponding to different substrate and/or buffer conditions, was compared against all other subsets to ensure that

the populations were statistically indistinguishable in regards to both the variance (ANOVA) and mean (Tukey Test).

The automated tangent overlay bend angle measurement technique was an automated, image processing based implementation of the manual tangent overlay procedure. This program, written in LabVIEW™ (National Instruments, Austin, TX), first applied a pixel threshold and adjusted the brightness, contrast, and gamma values of each image such that free DNA, unbound topoisomerase, and DNA-topoisomerase complex images were above the background threshold value. Secondly, the program applied a size threshold such that only the DNA-topoisomerase complex images were above the threshold value, thus filtering out all free DNA and free topoisomerases from the images. Rectangular regions containing images of the DNA-topoisomerase complexes were extracted and stored as sub-image files. Each sub-image window was individually judged by a human supervisor who would accept or reject complexes based on the same criteria used for manual tangent overlay,

Each selected sub-image was analyzed to determine the bend angle formed by the two DNA segments emerging from the topoisomerase. For each DNA-topoisomerase complex, a circular overlay was fitted to best match the shape of the enzyme, thus estimating its center and radius. Additionally, two concentric circles, centered on the protein, were superimposed on the complex such that the inner circle radius was 2-4 nm larger than the radius of the topoisomerase and the outer circle radius was 30-60 nm larger than the inner circle. Next, the skeleton of the DNA was extracted after applying a binary threshold to the image and removing small objects surrounding the DNA segments. Sections of the DNA skeletons lying between the two superimposed circles

were linearly fitted, and the fits were extrapolated to the point of intersection to determine the angle of intersection, ϕ, which was previously defined as the supplement to the bend angle, θ (Figure 3.2.2 and Figure 3.3.3). We used the methods of maximum likelihood and bootstrapping to determine the mean, standard deviation, and error of the angle distributions.

The end-to-end distance measurement technique assayed a more global property of bending by comparing measured end-to-end distances with simulated end to end distances (EEDs) of bent DNA molecules equilibrated in 2-D. We followed the method of Dame *et al.* (40) with two modifications. Briefly, for each DNA substrate, histograms of the end-to-end distances EED of simulated DNA molecules were generated using worm-like chain (WLC) statistics with a persistence length of 50 nm for a range of imposed bend angles. These histograms were then compared with the histogram of measured EEDs from the AFM images of topoisomerase-DNA complexes containing two DNA molecules joined by a topoisomerase. The χ^2 statistic was calculated using an expression developed specifically for Poisson distributed data, shown in Equation [3.2.1] where $f(x_i, \vec{\alpha})$ are the data from the simulated histogram and n_i are data from the histogram of the experimental data (41). The bend angle was defined as the imposed bend angle of simulated DNA that minimized the χ_P^2 value.

$$\chi_P^2 = \sum_{i=1}^{N} \left[2(f(x_i, \vec{\alpha}) - n_i) + (2n_i + 1) \log\left(\frac{2n_i + 1}{2f(x_i, \vec{\alpha}) + 1} \right) \right] \qquad [3.2.1]$$

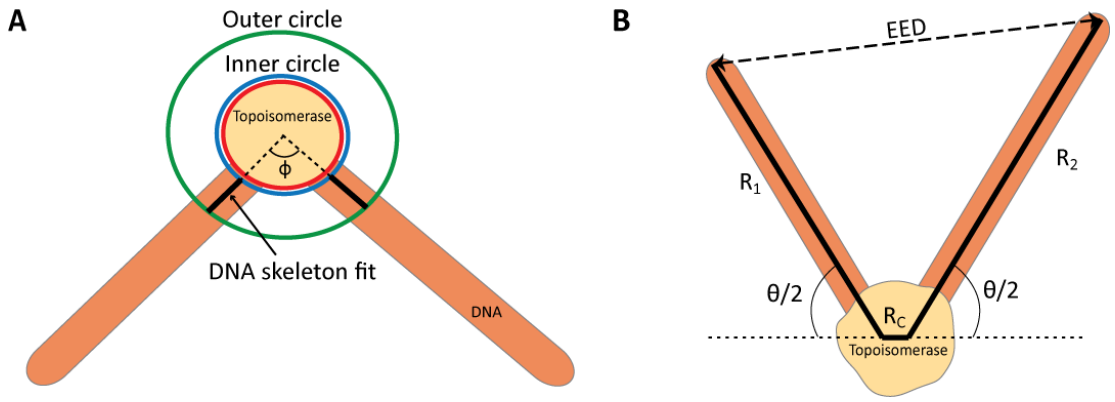

Figure 3.2.2 Alternative bend angle measurement methods. **A.** The method of automated tangent overlay. Here, the red circle represents an approximation of the boundary of the topoisomerase, and the blue inner circle and green outer circle represent the boundaries for the DNA skeleton fit, which is extrapolated to the point of intersection where ϕ, the supplement to the bend angle, is measured. **B.** The two-kink model of bending. R_c represents the section of DNA that is held constant and rigid between the two imposed bends, R_1 and R_2 represent the two fragments of DNA emerging from the topoisomerase, and EED represents the end-to-end distance between the two DNA endpoints.

This method was modified to account for the specific details of the DNA substrate used in this study and the binding geometry of type IIA topoisomerases (23,25,26). As shown in Figure 3.3.2, DNA substrates of varying lengths were used for the AFM imaging. In particular, substrates in which the restriction fragments were of unequal lengths could form three possible complexes with a topoisomerase stabilizing the palindromic four bp junction: the long fragment could bind to the shorter fragment with a probability of 0.5, the long fragment could bind to another long fragment with a probability of 0.25, or the short fragment could bind to another short fragment with a probability of 0.25. We accounted for this ambiguity in the bound substrates by simulating all possibilities and combining the simulations with the appropriate statistical weight (0.5 or 0.25). In other words, each simulated distribution was made up of 50% long-short, 25% long-long, and 25% long-short DNA complexes.

The second alteration of this method involved simulating a two-kink model of DNA bending instead of the one-kink bending model utilized by Dame *et al.* (40). In a one-kink model, the DNA is kinked in one position, creating a "V" shape. In a two-kink model, the DNA is kinked in two positions, creating a flat-bottomed "V", where the length of the flat bottom is held constant, and for the purpose of these simulations was assumed to be rigid (R_c) (Figure 3.2.2). Instead of imposing one bend of θ degrees, we imposed two bends, each $\theta/2$ degrees, on either side of the R_c segment of the DNA. We held the length constant in the R_c region for each simulation, but ran the simulation for four different values of R_c: 0, 2, 4, and 6 nm. Then, as in the original method, we used WLC statistics to model the segments of the DNA from the location of the bends to the ends of the DNA molecules. Because crystal structure data indicate that type IIA

topoisomerases bend DNA by imposing two bends on either side of a straight segment of DNA (23,25,26,42), we reasoned that the two-kink model of DNA bending would be more appropriate for our data than the one-kink model.

In addition to the bend angles determined by comparing the histograms of simulated data to experimental data, we also used a χ^2 statistic (Equation [3.2.3]) to compare the mean square EEDs for the simulated and experimental data (43). Here, $\langle R_{sim}^2 \rangle$ is the mean square EED of the simulated DNA for a given bend angle, $\langle R^2 \rangle$ is the measured mean square EED, and σ^2 is the variance of the mean square EED measurement. Figure 3.2.3 shows a representative histogram of experimental EED data and the best fit histogram of simulated DNA, as well as the plots of χ_P^2 as a function of bend angle for the simulated histogram data and $\chi_{\langle R^2 \rangle}^2$ as a function of bend angle for the mean square EEDs.

$$\chi_{\langle R^2 \rangle}^2 = \frac{\left(\langle R_{sim}^2 \rangle - \langle R^2 \rangle\right)^2}{\sigma^2} \qquad [3.2.2]$$

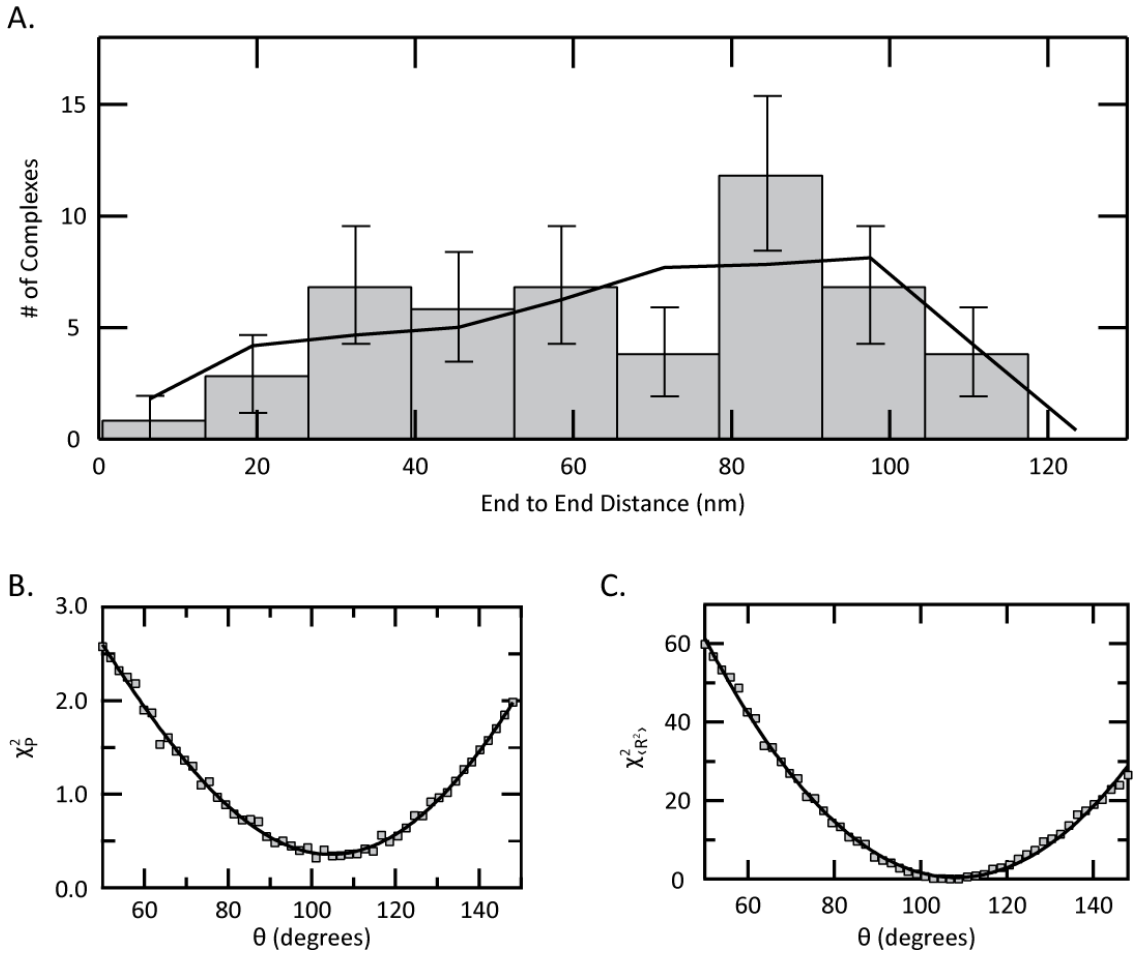

Figure 3.2.3 Representative results of DNA simulations. **A.** A representative histogram of the distribution of EEDs for DNA-yeast topoisomerase II complexes (bars) and the best fit histogram of simulated DNA EEDs (line). Goodness of fit was determined by minimizing the $\boldsymbol{\chi_P^2}$ and $\boldsymbol{\chi^2_{\langle R^2 \rangle}}$ statistics (Equations [3.2.1] and [3.2.3]). **B.** A graph of the $\boldsymbol{\chi_P^2}$ statistic vs. simulated bend angle for the histogram shown in A, fit with a quadratic function (line). C. A graph of the $\boldsymbol{\chi^2_{\langle R^2 \rangle}}$ statistic vs. bend angle, fit with a quadratic function (line).

3.2.3 Single Molecule FRET Experiments

FRET is a powerful spectroscopic technique that is used to determine distances, typically in the 3-10 nm range, by measuring the non-radiative energy transfer between two fluorescent molecules (79-81). The efficiency of this energy transfer, which is due to an induced dipole interaction between the two dyes, can be related to the distance between the two molecules, as shown in Equations [3.2.3] and [3.2.4].

$$E_{FRET} = \frac{I_A}{I_A + I_D} \qquad [3.2.3]$$

$$E_{FRET} = \frac{1}{1 + \left(\frac{r}{R_0}\right)^6} \qquad [3.2.4]$$

In Equations [3.2.3] and [3.2.4], I_A is the fluorescent intensity of the acceptor dye, I_D is the fluorescent intensity of the donor dye, r is the distance separating the two dyes, and R_0, known as the characteristic distance for a fluorophore pair, is the distance at which 50% of the donor molecule's energy is transferred to the acceptor (79,80). This technique is popular in biochemistry and molecular biology labs because the range over which distances can be measured by FRET are highly biologically relevant for probing inter- and intra-molecular nucleic acid and protein interactions. Once molecules are appropriately fluorescently labeled, measuring FRET efficiencies of molecules in bulk solution is also a fairly straightforward task requiring only an instrument that is capable of measuring fluorescent emission at a range of wavelengths.

Though ensemble FRET measurements yield useful data regarding the average distance between the two dyes over a fixed time period, single molecule FRET

(smFRET) measurements allow for monitoring of individual fluorescently labeled molecules as a function of time. This makes it is possible to identify multiple FRET states and probe the dynamics of the molecule being studied without losing information to averaging. However, smFRET is substantially more difficult to perform. Instead of relying on a multifunctional spectrofluorometer, smFRET requires a special instrument that is capable of resolving individual dyes in both time and space. The custom-built instrument used in our experiments relied on total internal reflection (TIR) microscopy, in which an evanescent wave, created by a laser beam that undergoes TIR at the surface of the sample cell, extends only ~100-200 of nm from the surface where the donor dyes are immobilized (80). By using this technique, excitation is achieved with minimal background fluorescence and a large area, measuring up to thousands of square microns, can be illuminated. A charge-coupled device (CCD) camera, which collects emitted light from the donor and acceptor molecules, allows for simultaneous monitoring of, and data collection from, hundreds of individual molecules (80). Prior to reaching the camera, the collimated emitted light beam is spectrally separated using a dichroic mirror and then passes through a lens, which allows each color to be projected upon different halves of the CCD screen and analyzed separately (79). A schematic of our experimental setup is shown in Figure 3.2.4. For details on the instrument configuration and experimental conditions, please see Appendix B: Detailed Methods.

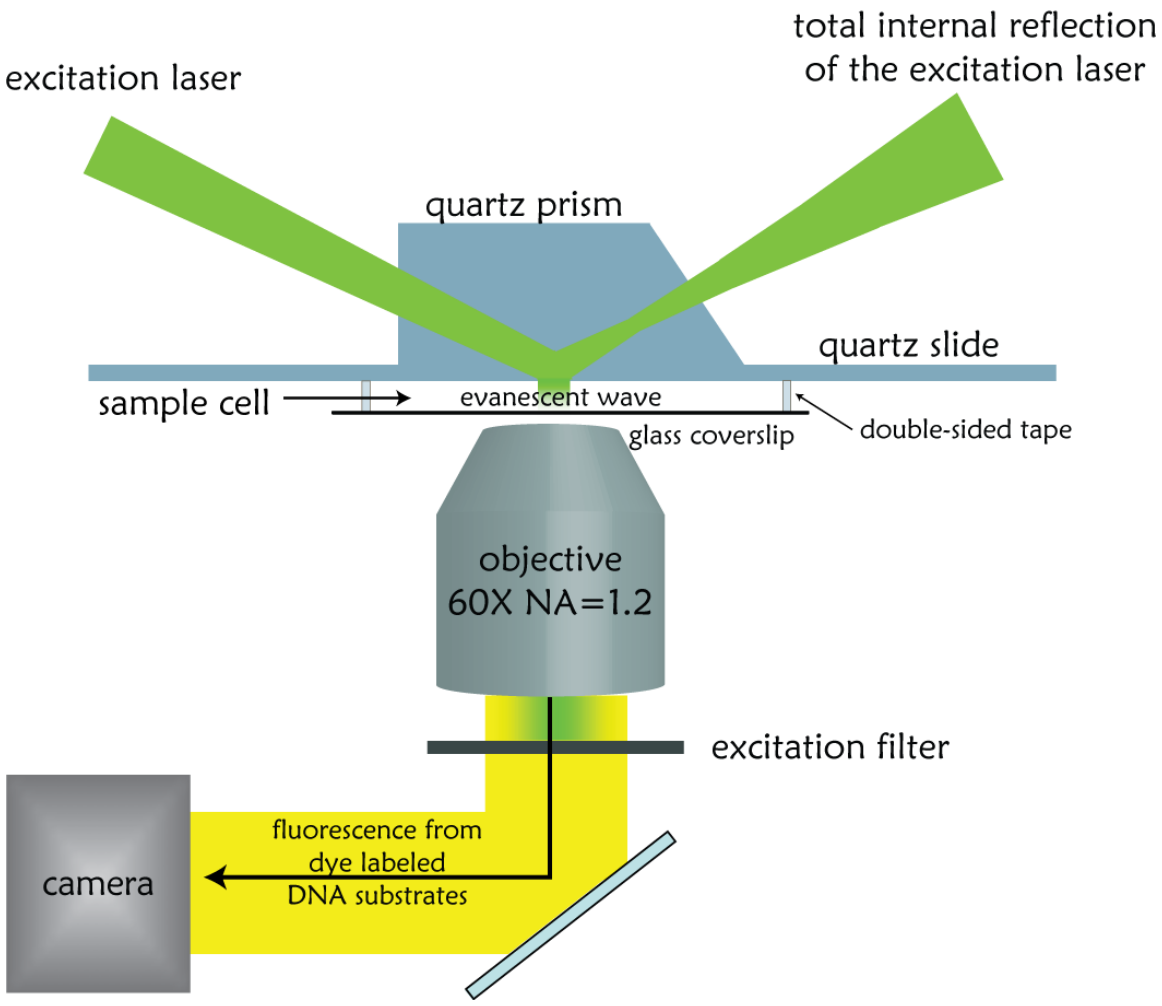

Figure 3.2.4 Schematic of smFRET setup. The excitation laser was totally internally reflected at the interface of the quartz prism and the sample cell creating an evanescent wave that illuminated approximately 250 nm into the sample. Light was collected by an objective with a 60X magnification and a numerical aperture (NA) of 1.2. Excitation light was rejected using a filter and then donor and acceptor light were separated (dichroic mirror separation step not shown) and projected onto a CCD camera.

In our smFRET experiments, we used two DNA substrates, one that contained an acceptor dye (F1) and another that contained the donor dye (F2) (Figure 3.2.5A). These substrates each contain a four bp overhang that is complementary to that of the other substrate. These are also the same substrates as used in DNA-protein co-crystallization experiments done with yTopo II (63) with a single base change in the four bp overhang to disrupt its palindromic symmetry and a 30 bp extension on the donor substrate (F2), well separated from the binding site, to prevent the protein from interacting with the surface of the slide (Figure 3.2.5A). Biotinylated donor substrates (F2, Figure 3.2.5A) were immobilized on the quartz surface of the flow cell using a streptavidin-biotin linker. Since the acceptor was on a separate DNA substrate (F1) we observed FRET only when a topoisomerase bound both the donor and acceptor substrates and introduced a bend (Figure 3.2.5B). A control experiment with both donor and acceptor substrates but no topoisomerase showed no FRET.

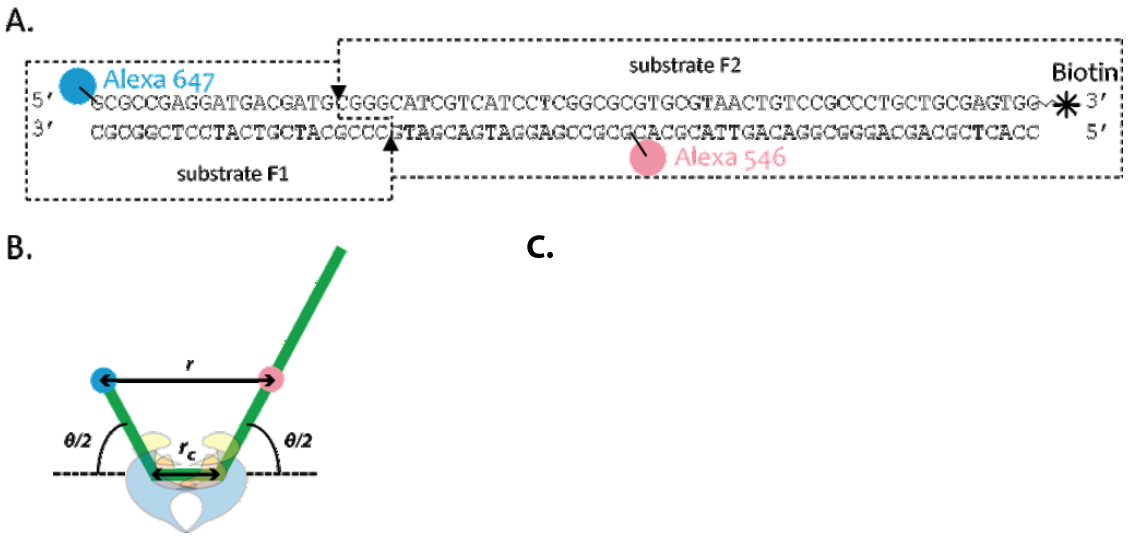

Figure 3.2.5 Schematics of single-molecule FRET experiments **A.** DNA used in single molecule FRET experiments showing locations of the fluorophores, Alexa546 and Alexa647, biotin, and double stranded 4 bp overhang. **B.** Schematic of a type IIA topoisomerase bending the FRET substrate. The distance between the fluorophores (r) was determined from the FRET efficiency measurements (Equation [3.2.4]) and related to the bend angle using the relationship shown in Equation [1.3.6]. Here, r_c is the length of the unbent DNA segment between the two bent DNA segments and r_{tot} (not labeled) is the contour length of DNA between the two fluorophores. **C.** Diagram of the estimated helical pitch (r_{rise}) used in the calculation of θ from the FRET efficiency [Partially reprinted from *The Journal of Molecular Biology*, **320**, Konstantin Klenin, Jorg Langowski, Alexander Vologodskii, "Computational Analysis of the Chiral Action of Type II DNA Topoisomerases", 359-367, Copyright (2002), with permission from Elsevier (60), (Appendix A)].

3.3 Type II Topoisomerases Impose Comparable Bend Angles on DNA

The bend angle model posits that the degree of non-equilibrium topology simplification by type IIA topoisomerases depends on the extent of G-segment DNA bending. In order for DNA bending to account for differences in topology simplification, the type IIA topoisomerases we investigated would impose significantly different bend angles, ranging from ~100° for yTopo II to more than 300° for Topo IV (60). To evaluate the feasibility of this model, we used AFM and single molecule FRET to determine the differences in G-segment DNA bending among type IIA topoisomerases that exhibit a wide range of non-equilibrium relaxation activities (Figure 1.6.1). Figure 3.3.1 shows typical AFM images of topoisomerase IIA-DNA complexes as well as DNA in the absence of protein.

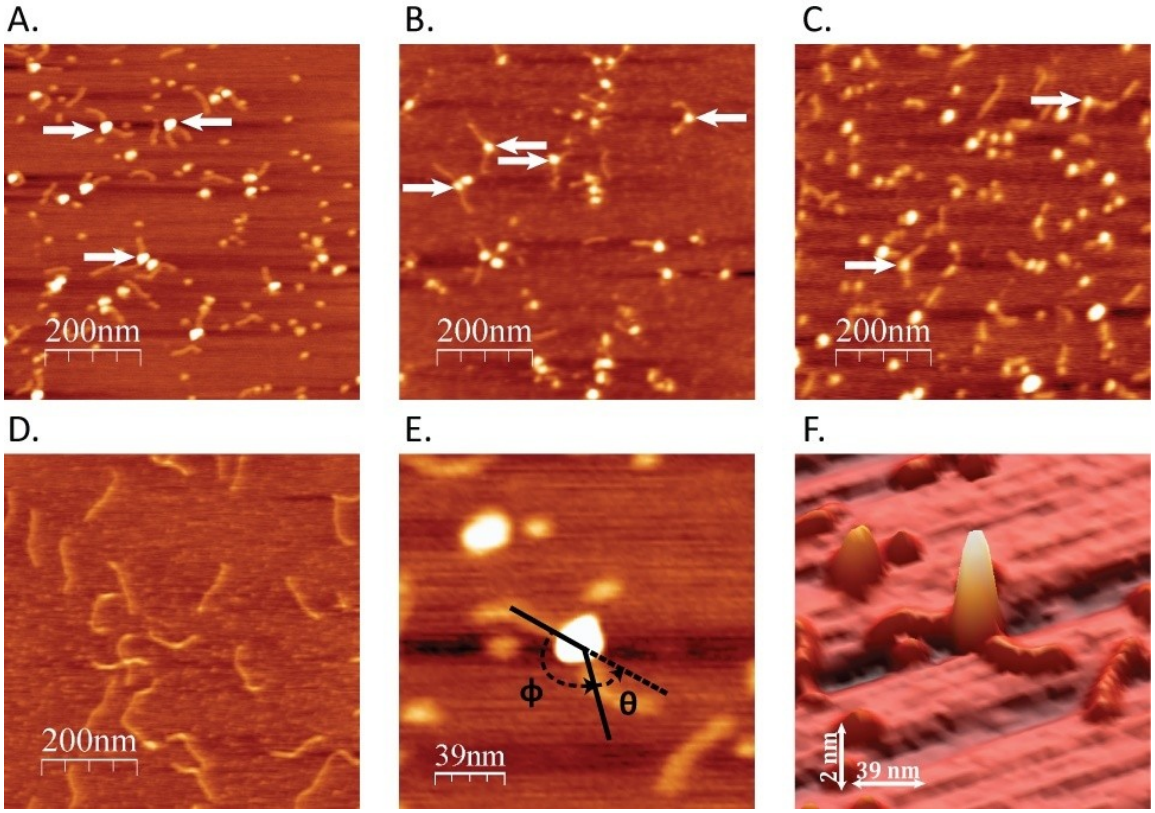

Figure 3.3.1 AFM images of DNA-type IIA topoisomerase complexes. **A.** Representative Topo IV-DNA complexes with DNA substrate D3 (designated by white arrows). **B.** yTopo II-DNA complexes with DNA substrate D5. **C.** hTopo IIα-DNA complexes with DNA substrate D5. **D.** DNA in the absence of protein. **E.** One DNA-Topo IV complex with the measured angle (ϕ) and bend angle (θ) indicated. **F.** Three-dimensional representation of the complex from (E). The vertical scale has been expanded for clarity.

We incubated Topo IV with one of two linear DNA substrates, D1 or D2 (Figure 3.3.2), each of which included a putative Topo IV binding sequence adapted from Marians and Hiasa (82). The complexes were deposited on freshly cleaved mica and imaged in air using tapping mode AFM. These substrates exhibited low binding affinity under the conditions required for AFM imaging of protein-DNA complexes (10-60 nM enzyme). Since type IIA topoisomerases have been shown to preferentially bind and stabilize four bp complementary overhangs (63), we developed substrates D3 and D4 (Figure 3.3.2) that contained complementary four bp overhangs to stabilize binding. This binding configuration further provided a high degree of specificity as complexes consisting of two DNA segments joined by a topoisomerase could be easily distinguished from topoisomerase binding to individual short DNA segments in the AFM images. Furthermore, the sequence of the DNA bound by the topoisomerase in these tripartite complexes was well defined, as were the lengths of the DNA segments on either side of the binding site, thus facilitating further analysis (see section 3.4).

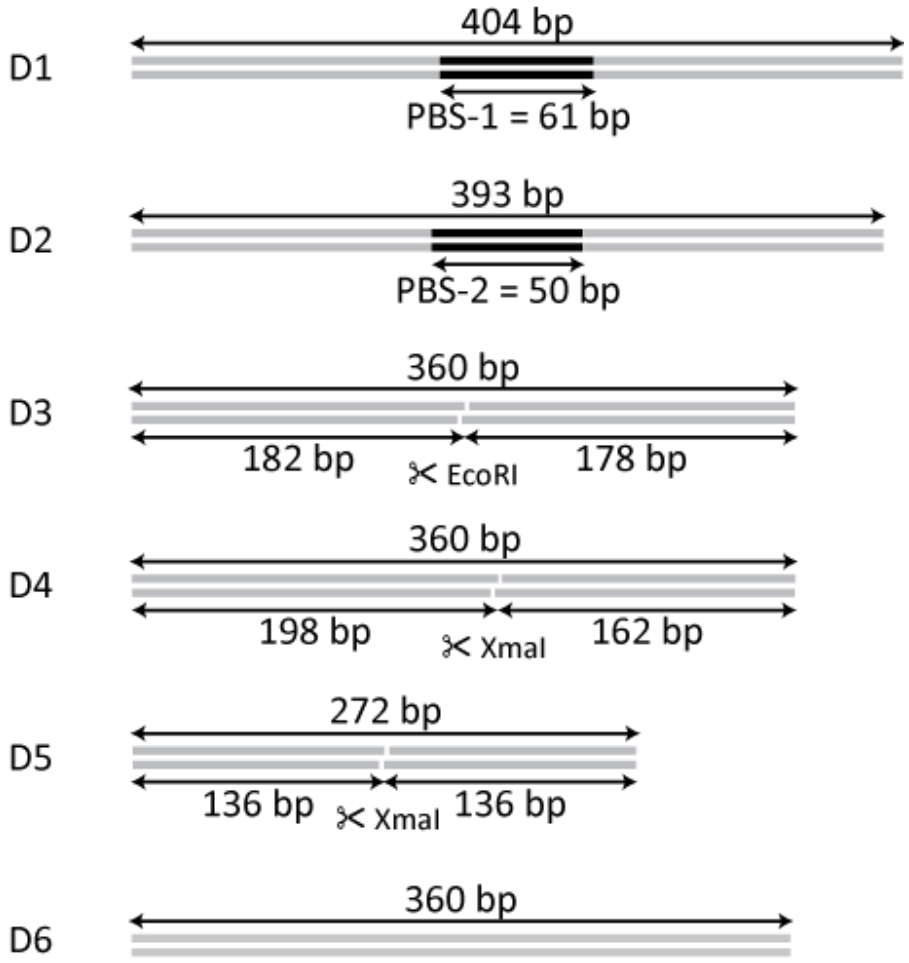

Figure 3.3.2 DNA substrates used for AFM imaging. D1 and D2 contain putative Topo IV binding sequences PBS-1 and PBS-2 respectively (see main text for sequence). D3-D5 were digested with the restriction enzyme noted. D6 is identical in sequence to D3 and D4 but undigested. All DNA substrates were made by PCR, based on the multiple cloning site of pUC19 plasmid. For DNA sequences, see Appendix B.

Substrates D3 and D4 resulted in a higher fraction of Topo IV bound to DNA in the AFM images. Whereas it is conceivable that these substrates could affect the protein induced bending, footprinting experiments suggest that the protein protects ~34 bp (82), and crystal structures of type IIA topoisomerases bound to DNA show that bending occurs ~5 bp away from the cleavage sites (63,64). Furthermore, statistical analysis confirmed that the bend angles imposed on intact and doubly nicked DNA segments by Topo IV were indistinguishable.

For all four DNA substrates, we observed DNA bending when Topo IV was bound (Figure 3.3.1A, E, and F). The included angle (ϕ) between the DNA segments emerging from the protein was measured as previously described (83-86), and the bend angle (θ) was defined as the supplement of ϕ, i.e., $\theta = 180° - \phi$ (Figure 3.3.3 and Figure 3.3.1E). We determined bend angles for Topo IV bound to the four DNA substrates described above under several buffer conditions. Measured bend angles were normally distributed, and ANOVA and Tukey tests (87) of the bend angle distributions for intact and cleaved DNA substrates under all buffer conditions indicate that the populations were statistically indistinguishable (P_{ANOVA} and $P_{Tukey} > 0.05$). Hence, all data for Topo IV were combined and analyzed using maximum likelihood estimation (88) to determine the mean and standard deviation of the bend angle. We found that Topo IV bent the DNA by a mean angle of $80 \pm 3°$ with a standard deviation of $30 \pm 2°$ ($n = 242$) (Figure 3.3.4A). The uncertainties represent the standard errors of the mean obtained by bootstrap analysis (89).

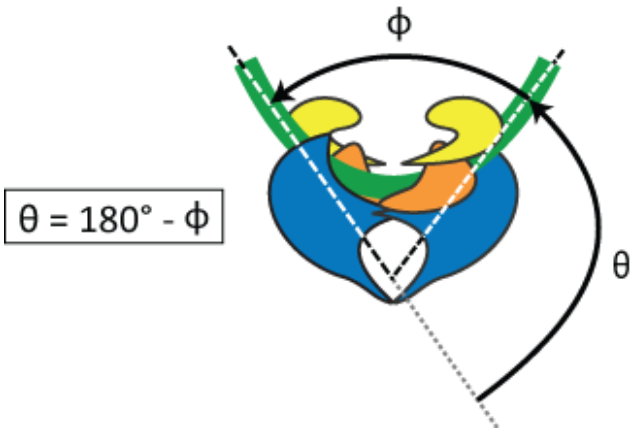

Figure 3.3.3 The bend angle, θ, is defined as the angle through which the DNA is bent from a straight line. The opening angle, ϕ, measured between the two DNA segments emerging from the topoisomerase, is the supplement of the bend angle, hence $\theta = 180 - \phi$.

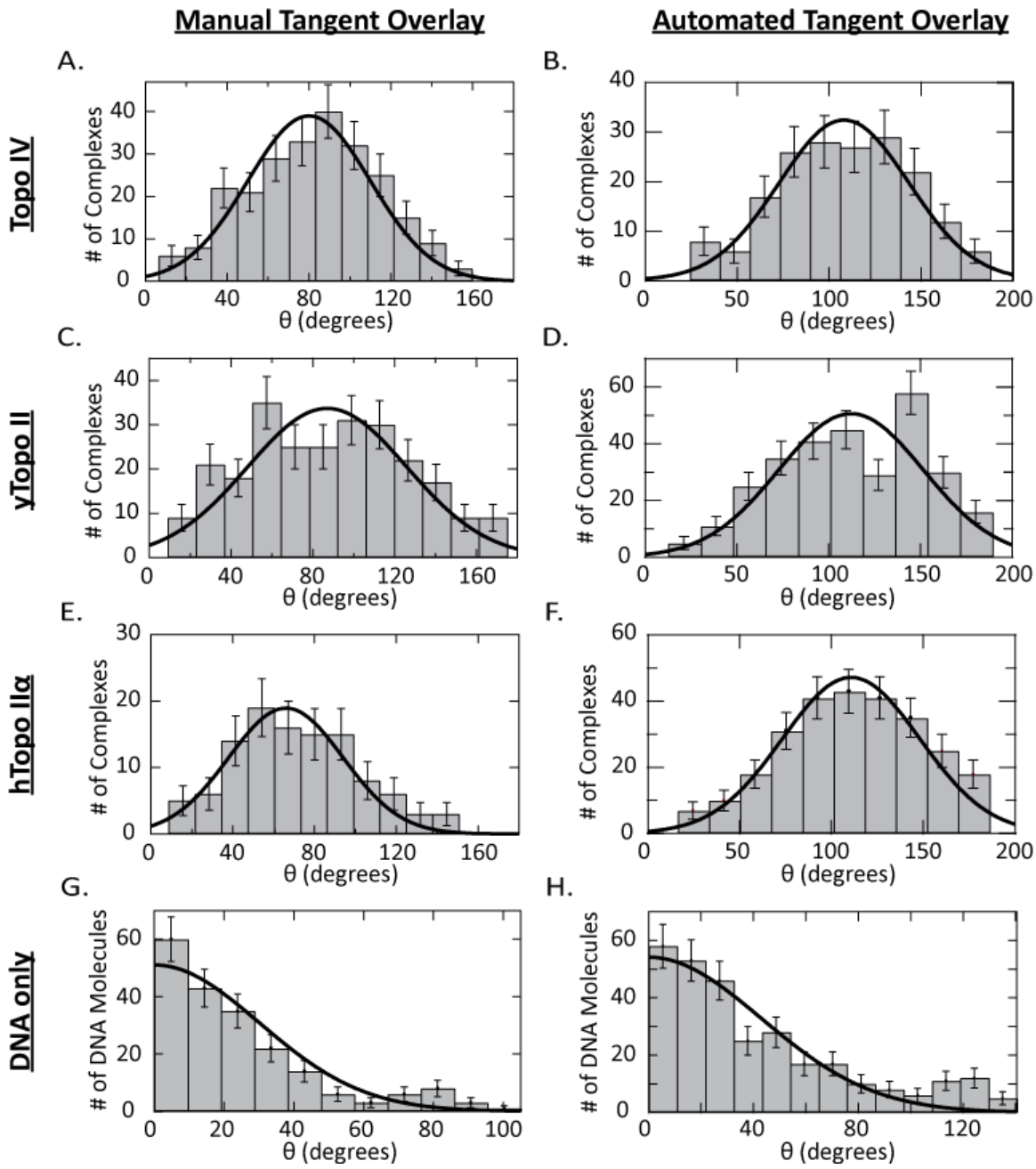

Figure 3.3.4 Distributions of bend angles imposed on DNA by different type IIA topoisomerases. Distribution of bend angles for Topo IV **A.** determined by: manual tangent overlay ($\mu = 80 \pm 3°$, $\sigma = 30 \pm 2°$, $n = 242$) and **B.** automated tangent overlay ($\mu = 100 \pm 4°$, $\sigma = 35 \pm 2°$, $n = 181$). Distribution of bend angles for yTopo II **C.** manual tangent overlay ($\mu = 87 \pm 5°$, $\sigma = 39 \pm 3°$, $n = 251$) and **D.** automated tangent overlay

($\mu = 103 \pm 4°$, $\sigma = 40 \pm 2°$, $n = 295$). Distribution of bend angles for hTopo IIα **E.** manual tangent overlay ($\mu = 66 \pm 4°$, $\sigma = 28 \pm 3°$, $n = 110$) and **F.** automated tangent overlay ($\mu = 102 \pm 5°$, $\sigma = 37 \pm 3°$, $n = 269$). Curves represent Gaussian distributions with parameters obtained from maximum likelihood fitting of the data with errors determined by bootstrapping (88,89). Distribution of bend angles for DNA in the absence of protein **G.** manual tangent overlay ($\mu = 0 \pm 1°$, $\sigma = 30 \pm 4°$, $n = 201$) and **H.** automated tangent overlay ($\mu = 0 \pm 1°$, $\sigma = 43 \pm 13°$, $n = 247$). These curves represent the best fit of a folded Gaussian distribution to the bend angle histograms with means and errors determined by bootstrapping (89-92).

In addition to the manual tangent overlay method, we also used an automated tangent overlay method and an end-to-end distance (EED) analysis to determine bend angles from the AFM images. Using the method of automated tangent overlay, we found that Topo IV bent the DNA by a mean angle of 100 ± 4° with a standard deviation of 35 ± 2° (n = 181) (Figure 3.3.4B). Using EED analysis we found that Topo IV bent DNA by a mean angle of 99 ± 38° (n = 242) or 124 ± 38° (n = 181), for manually and automatically selected populations of protein-DNA complexes, respectively.

Since the bend angles measured for Topo IV were independent of the DNA substrate, we used substrates D4 and D5, which is a symmetric version of D4 (Figure 3.3.2), to measure bending by yTopo II and hTopo IIα. Manual tangent overlay showed that yTopo II imposed a bend angle of 87 ± 5° with a standard deviation of 39 ± 3° (n = 251), automated tangent overlay showed that yTopo II imposed a bend angle of 103 ± 4° with a standard deviation of 40 ± 2° (n = 295), and EED analysis showed that yTopo II imposed a bend angle of 105 ± 35° (n = 251) or 103 ± 35° (n = 295), depending on the population of protein-DNA complexes used (manually or automatically selected, respectively) (Figure 3.3.4C, D). Manual tangent overlay showed that hTopo IIα imposed a bend angle of 66 ± 4° with a standard deviation of 28 ± 3° (n = 110) (Figure 3.3.4E, F), automated tangent overlay showed that hTopo IIα imposed a bend angle of 102 ± 5° with a standard deviation of 37 ± 3° (n = 269), and EED analysis showed that hTopo IIα imposed a bend angle of 84 ± 32° (n = 110) or 127 ± 32° (n = 269), depending on the population of protein-DNA complexes used (manually or automatically selected, respectively). The measured bend angles for each topoisomerase using each method are summarized in Table 3.3.1.

Table 3.3.1 Bend angles measured from AFM images using four different analysis techniques and bend angles measured from single molecule FRET.

	Topo IV(°)	**yTopo II(°)**	**hTopo IIα(°)**
AFM			
Manual Tangent[a]	80 ± 3	87 ± 5	66 ± 4
Automated Tangent[a]	100 ± 4	103 ± 4	102 ± 5
EED Histogram Fit (manual)[b]	99 ± 38	105 ± 35	84 ± 32
Mean EED χ^2 (manual)[b]	102 ± 4	108 ± 7	81 ± 7
EED Histogram Fit (automated)[b]	123 ± 34	103 ± 17	126 ± 25
Mean EED χ^2 (automated)[b]	119 ± 6	102 ± 4	123 ± 4
Weighted Mean of AFM measurements	*94 ± 13*	*100 ± 7*	*95 ± 24*
Single Molecule FRET	126 ± 18	140 ± 16	136 ± 17

[a]Mean ± SEM
[b]θ ± angle at minimum χ^2+1, R_c = 6 nm, see text

To determine the intrinsic bending of DNA on the mica surface, we imaged a 360 bp fragment of linear DNA (substrate D6, Figure 1.2.1) in the absence of protein (Figure 3.3.1D). We measured the bending of the DNA from the AFM images as previously described (83,85). Using ImageJ, circles were drawn near the middle of each DNA molecule to simulate bound protein. The bend angles were then measured using the angle measurement tool in ImageJ, as described above. All measurements of ϕ were taken to be smaller than 180°, resulting in a folded Gaussian distribution bend angles as described by Le Cam *et al.* (91) and Cherny *et al.* (92). Fitting this data to a folded Gaussian (Equation [3.3.1]), we found that the mean bend angle in the absence of protein was 0 ± 1° with a standard deviation of 30 ± 4° (n = 201) for bend angles measured using manual tangent overlay and the mean and standard deviation were 0 ± 1° and 43 ± 13° (n = 247), respectively, for bend angles measured via automated tangent overlay (Figure 3.3.4G, H).

$$f(\mu,\sigma,\theta) = \frac{1}{\sigma\sqrt{2\pi}}\left(e^{-\frac{(\theta-\mu)^2}{2\sigma^2}} + e^{-\frac{(\theta+\mu)^2}{2\sigma^2}}\right) \qquad [3.3.1]$$

In addition to the AFM measurements, we made smFRET measurements to estimate the bend angle imposed on DNA by each topoisomerase. Figure 3.3.4 shows the histograms of FRET efficiency values for each topoisomerase and a graph showing the relationship between FRET efficiency and DNA bend angle. The substrate we used for these experiments in the same substrate as used in the crystallization experiments done with yTopo II (63) with a single base change in the four bp overhang to disrupt its palindromic symmetry and a 30 bp extension, well separated from the binding site, to prevent the protein from interacting with the surface of the slide (Figure 3.2.5). The mean FRET efficiencies for Topo IV, yTopo II and hTopo IIα were 0.225 ± .007 (n = 20941),

0.370 ± .009 (n = 28363), and 0.324 ± .010 (n = 26593) (mean ± SEM), respectively (Figure 3.3.5A).

We calculated the average fluorophore separation (r) from the measured FRET efficiencies using Equation [3.2.4] with a calculated R_0 value of 7.4 nm ± 10% for the Alexa546-Alexa647 fluorophore pair used in the single molecule FRET experiments. To calculate the imposed bend angle, we assumed the DNA geometry was similar to that observed in crystal structures (63-66). Accordingly, we modeled the bend as two symmetric bends (with bend angle $\theta/_2$) on either side of a short DNA segment of length r_c between the two dyes separated by a total distance along the DNA of r_{tot} (Figure 3.2.5). In the analysis of our single molecule FRET data, we included the possibility of a small helical pitch of the DNA. The inclusion of a significant helical pitch was a feature of the bend angle model. Klenin *et. al* determined that the bend angle model was insensitive to the helical pitch when it exceeded a 9 nm helical rise over 150 bp, which corresponds to a rise per bp of only 0.06 nm/bp (60). Because the protein contacts less than 40 bp of DNA, we estimated that the helical rise would be only on the order of ~3 nm over the biologically relevant length of DNA. We incorporated this DNA rise into the FRET calculations by introducing an additional term, r_{rise} (Figure 3.2.5C) into the equation for calculating r. We used a value of r_{rise} = 1.5 ± 1.5 nm as the three possible cases representing zero helical rise, an intermediate 1.5 nm rise, and the ~3 nm helical rise assumed by the bend angle model (60). Equation [1.3.6] describes the relationship between the dye separation, r, and the geometry of the bent DNA.

$$r = \sqrt{\left|r_c + (r_{tot} - r_c) * cos\left(\frac{\theta}{2}\right)\right|^2 + r_{rise}^2} \qquad [3.3.2]$$

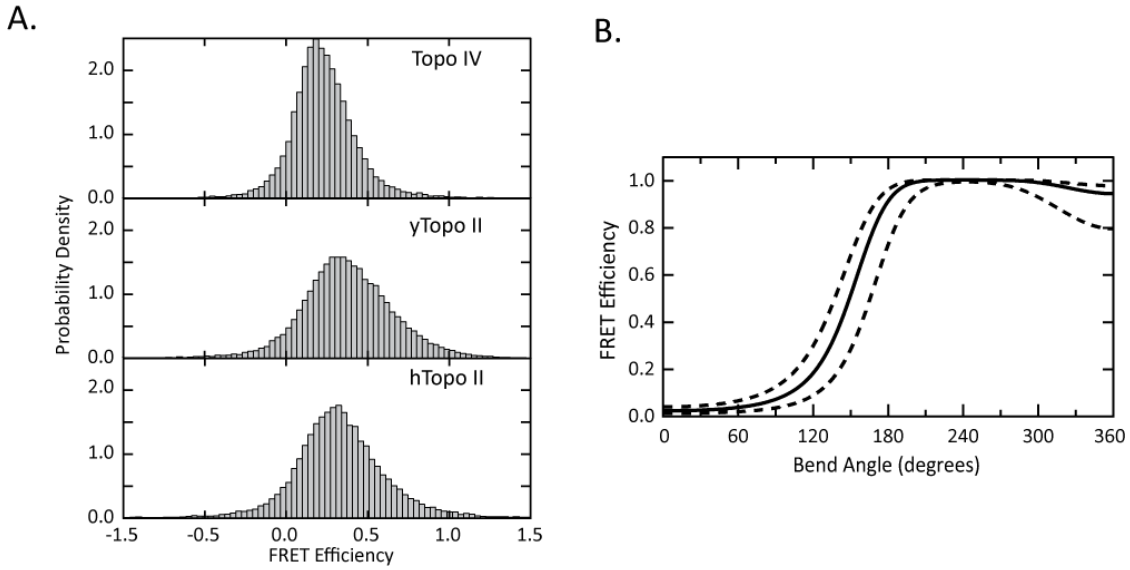

Figure 3.3.5 FRET efficiencies and relationship to DNA bend angle. **A.** Histograms of FRET data for Topo IV (0.225 ± 0.007, n = 20941), yTopo II (0.370 ± 0.009, n = 28363), and hTopo IIα (0.324 ± 0.010, n = 26593) (mean ± SEM). **B.** Plots showing FRET efficiency as a function of bend angle (Equations [3.2.4] and [1.3.6]) for the DNA substrate used in the FRET experiments using R_0 = 7.4, r_c = 4.8 nm, r_{tot} = 14 nm, and r_{rise} = 1.5 nm (solid line) and the FRET efficiency vs. bend angle relationship when experimental uncertainties, such as uncertainties in R_0 (± 10%) and r_{rise} (± 1.5 nm), are taken into account (dashed lines). See Appendix C for sample smFRET traces.

We calculated the separation between dyes on the DNA substrate, r_{tot} = 14 nm, assuming a length per base of 0.334 nm and based on the yTopo II crystal structure we set r_c = 4.8 nm (63). The resulting relationship between FRET efficiency and the bend angle θ is plotted in Figure 3.3.5B. With this model, the computed bend angles were 126 ± 18° for Topo IV, 140 ± 16° for yTopo II, and 136 ± 17° for hTopo IIα (Table 3.3.1).

Although these bend angles are larger than those determined from the AFM images, the differences in the bend angles among the topoisomerases are very similar. These larger bend angles are also more consistent with DNA bends determined from crystal structures (63-66). Importantly, the single molecule FRET bend angle measurements were made in the same buffer in which the relaxation experiments were performed. We have observed that the composition of the buffer, particularly the ionic strength, changes not only the affinity but also the bend angle imposed by the topoisomerases (data not shown). It is possible that the AFM deposition buffer, which was optimized to achieve equilibrated binding of the protein DNA complexes onto the mica surface, contributed to the somewhat lower bend angles measured from the AFM images. Nevertheless, the FRET data and AFM data agree that the three type IIA topoisomerases investigated here bend DNA to a similar degree.

3.4 Verification of 2-D Equilibration of Protein-DNA Complexes on the Surface of the Mica in AFM Experiments

To accurately measure the DNA bend angle imposed by a bound protein from AFM images, the DNA must be deposited on the mica surface under conditions that favor two-

dimensional (2-D) equilibration of the DNA in the plane of the mica rather than a kinetically pinned 2-D projection of a three-dimensional (3-D) conformation (78,93,94). Reliable 2-D equilibration of DNA on the surface of mica for AFM imaging is consistently achieved using divalent magnesium cations in the deposition buffer to form an electrostatic salt bridge between the negatively charged surface of the mica and the negatively charged DNA (78,93,95-97). Using these deposition conditions, DNA-protein interactions are routinely probed with AFM and measured protein induced DNA bend angles have been extensively confirmed by other techniques including gel shift assays (84,94,98,99), crystal structures (83,84,94), transient electric birefringence measurements (94,98,100), and cyclization experiments (94,100). We used established deposition conditions that favor 2-D equilibration on the mica surface (78,93,96,97). Nevertheless, we verified that, under our deposition conditions, the DNA molecules achieved a 2-D equilibration rather than a 2-D projection by analyzing the polymer statistics of the deposited DNA. We utilized the fast marching algorithm and custom MATLAB (MathWorks, Natick, MA) program, DIPimage, developed by Faas *et al*. to determine the backbone coordinates of DNA molecules with no protein bound in AFM images (96). The polymer statistical quantities: $\langle D^4 \rangle = \frac{\langle R^4 \rangle - \langle R^2 \rangle^2}{L^4}$, $\langle R^2 \rangle$, $\langle \cos\theta \rangle$, and $\langle \theta^2 \rangle$ as a function of L, the contour length along the DNA, were obtained from the backbone coordinates. We were able to fit the plots of these polymer statistics using the expressions derived by Faas *et al.* (96) for the 2-D equilibration case and for the 2-D projection of a 3-D conformation case, using the persistence length as the only fitting parameter (Figure 3.4.1). Though the persistence lengths determine from the $\langle R^2 \rangle$, $\langle \cos\theta \rangle$, and $\langle \theta^2 \rangle$ statistics all scale with increasing dimensionality, it is not possible to use these alone to

determine the state of DNA equilibration. However, the $\langle D^4 \rangle$ statistic does not scale with increased dimensionality. Thus, by comparing the persistence lengths obtained by fitting the $\langle D^4 \rangle$ statistic for the case of both a 2-D equilibration and 3-D projection to those quantities obtained by fitting the other three statistics, we were able to determine the dimensionality of the deposited DNA. We found that the 2-D equilibration equations gave a consistent persistence length of ~50 nm for all four cases, while the 3-D projection equations gave persistence lengths that were as small as ~60 nm in the $\langle D^4 \rangle$ case and as large as ~100 nm in the case of $\langle R^2 \rangle$, $\langle \cos \theta \rangle$, and $\langle \theta^2 \rangle$ (Figure 3.4.1,Table 3.4.1). The agreement of the calculated persistence length in the 2-D equilibration case is evidence that the DNA had fully equilibrated on the surface of the mica in the AFM images.

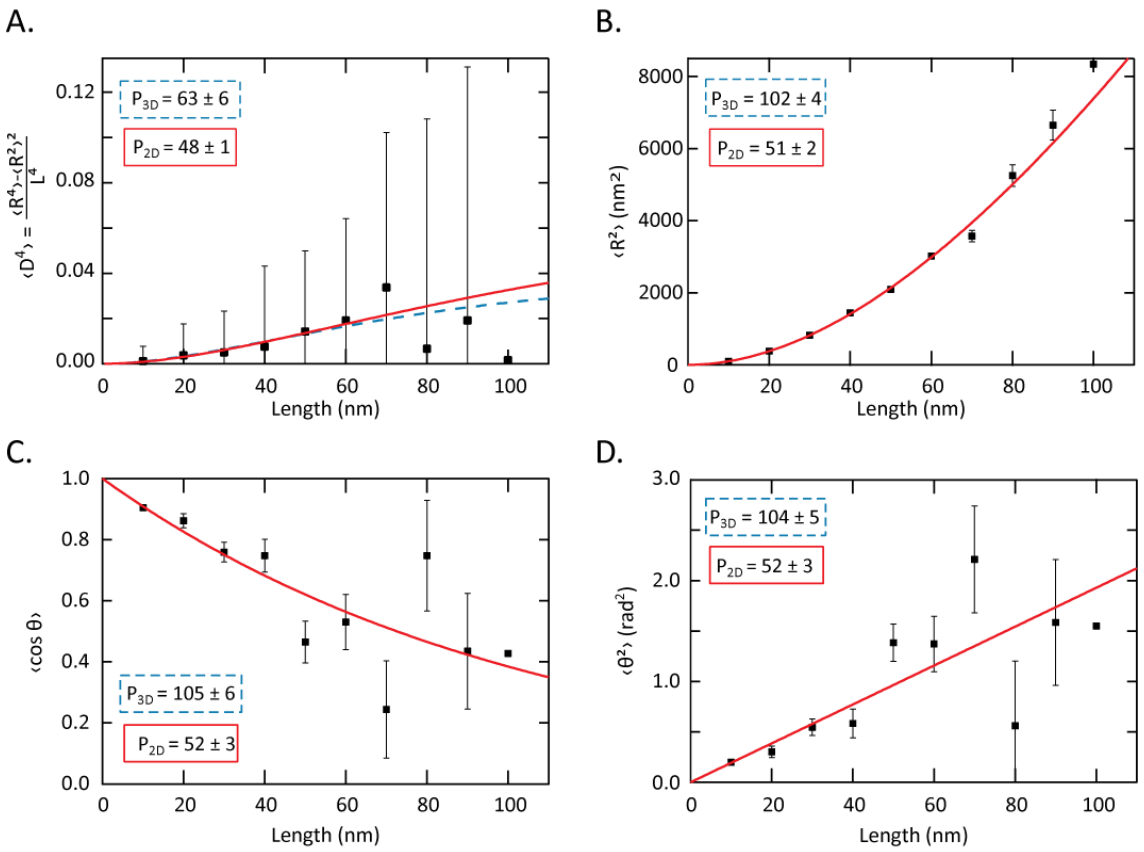

Figure 3.4.1 DNA persistence lengths determined by 2-D (P_{2D}) and 3-D (P_{3D}) fits to polymer statistical measures (96). **A.** The $\langle \boldsymbol{D^4} \rangle$ statistic as a function of contour length was fit to the equations for 2-D equilibration (red line) and 2-D projection of a 3-D conformation (blue dashed line). The persistence length was the only fitting parameter. Plots of **B.** the $\langle \boldsymbol{R^2} \rangle$ statistic, **C.** the $\langle \boldsymbol{\cos \theta} \rangle$ statistic, **D.** and the $\langle \boldsymbol{\theta^2} \rangle$ statistic plotted as a function of the DNA contour length fit to the equations for 2-D equilibration (red line) and 2-D projection (not shown). The two fits are identical but the 2-D projection returns a persistence length twice that of the 2-D equilibration for all three statistics.

Table 3.4.1 DNA persistence lengths determined by fits to polymer statistical measures (Figure 3.4.1) for 2-D equilibration vs. 2-D projection of a 3-D conformation onto the surface of the mica.

	$P_{2\text{-}D}$ (nm)[a]	$P_{3\text{-}D}$ (nm)[a]
$\langle R^2 \rangle$	51 ± 2	102 ± 4
$\langle \theta^2 \rangle$	52 ± 3	104 ± 6
$\langle \cos\ \theta \rangle$	52 ± 3	104 ± 6
$\langle D^4 \rangle$	48 ± 1	63 ± 6

[a]Fit parameter ± fitting uncertainties

To further confirm that the DNA-protein complexes were equilibrated in 2-D, we determined the DNA and topoisomerase height profiles as a function of bend angle (Figure 3.4.2). If the DNA-protein complex equilibrated in such a manner that the plane of the DNA bend did not lie in the plane of the mica, the height profile would likely be distorted in a bend-angle dependent manner due to the large persistence length of DNA. In a simple geometric model, measured bend angles would be maximal and the topographical height variation minimal, for bends lying in the plane of the mica, whereas the measured bend would be near zero and the height variation would be maximal for bends lying in a plane orthogonal to the mica. However, there was no correlation ($R \sim 0$) between the height of the topoisomerases and the bend angle (Figure 3.4.2). Furthermore, we determined the difference in height for two points on the DNA located 3 and 16 nm from the enzyme and plotted these with respect to bend angle (Figure 3.4.2). These data were also uncorrelated, suggesting that the DNA and protein both fully equilibrated in 2-D onto the surface of the mica.

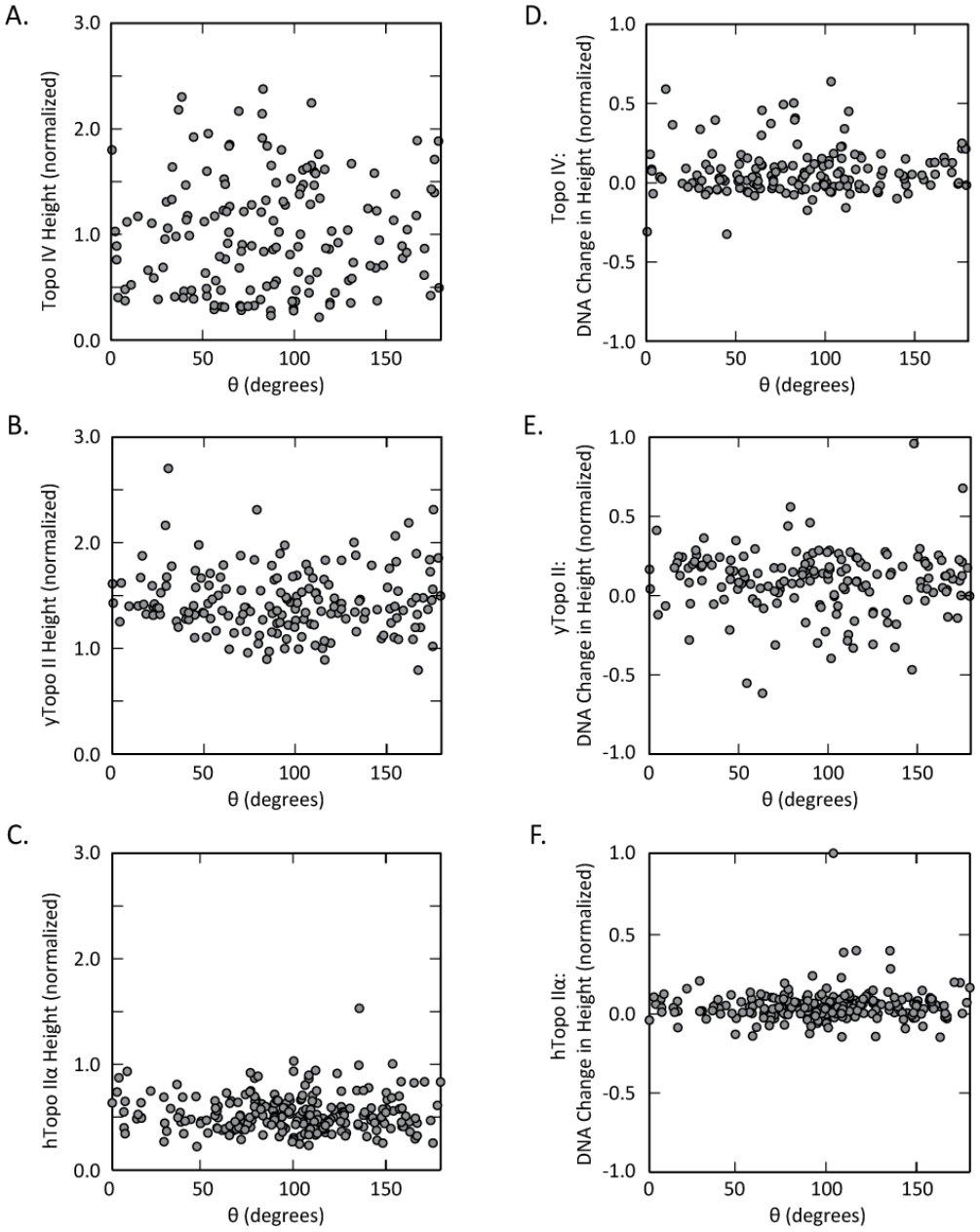

Figure 3.4.2 Protein and DNA intensity profiles as a function of bend angle. The normalized intensity (height) as a function of bend angle for **A.** Topo IV, **B.** yTopo II, and **C.** hTopo IIα. $R_{correlation} < 0.05$ for each enzyme. The change in normalized intensity (height) of DNA between 3 and 16 nm from the enzyme plotted as a function of bend angle for **D.** Topo IV, **E.** yTopo II, and **F.** hTopo IIα. $R_{correlation} < 0.1$ for each enzyme.

Our claim of 2-D DNA equilibration is further supported by the agreement among bend angles determined by both the local measurement of the bend angle (both manual and automated) and the more global measurement of the EEDs. Were the DNA not equilibrated in 2-D, these measurements would not have been as consistent as the simulations assumed a 2-D equilibration of the DNA on the surface.

3.5 Additional Evidence Contradicting the Bend Angle Model

Though the bend angle model was developed to explain non-equilibrium topology simplification, the sharp DNA bending predicted by the model has other implications. Klenin *et al.* (60) used Monte Carlo simulations to calculate the effects of sharply bent G-segment DNA on topoisomerase binding and activity. In addition to offering a possible mechanism by which topoisomerases could couple ATP hydrolysis to preferential DNA strand passage, the simulations revealed other, unexpected, predictions concerning type IIA topoisomerase behavior. Many of these predictions have been addressed in subsequent publications, but their significance with respect to the bend angle model has not been discussed. For instance, the bend angle model suggests that a sharp bend imposed on DNA by Topo IV would result in a twenty fold higher binding affinity for positively supercoiled ((+)sc) DNA than for negatively supercoiled ((–)sc) DNA. However, the binding affinity of Topo IV for (+)sc and (–)sc DNA is the same or at most a factor of ~3 larger for (+)sc DNA (34,101,102). A large bend angle imposed by Topo IV would also provide a mechanism to explain the higher efficiency of Topo IV in relaxing (+)sc DNA than (–)sc DNA (34,101,102). However, recent work suggests that chiral discrimination by Topo IV results from differences in processivity rather than

initial binding differences (101). Moreover, hTopo IIα has also been shown to relax (+)sc DNA an order of magnitude more efficiently than (–)sc DNA, yet its binding affinity is slightly higher for (–)sc DNA (52). The bend angle model also predicts that Topo IV should localize at apices of supercoils 87% of the time for (–) supercoils, but only 28% of the time for (+) supercoils (60). Whereas this prediction has not been directly tested, data from magnetic tweezers pulling assays suggest that Topo IV has a 50% or higher affinity for (+) supercoil plectoneme apices (75). Furthermore, recent simulation data using an improved WLC model for DNA has shown that a DNA hairpin, i.e., a sharp bend formed by a topoisomerase, is not sufficient to reproduce the experimentally observed degree of topology simplification (67,71).

Measurements of the DNA circle size dependence of non-equilibrium relaxation provide additional evidence suggesting that the bend angle model does not completely describe non-equilibrium topological relaxation (27,45,61). The impact of DNA bending, and therefore the efficiency of the non-equilibrium relaxation process, would be expected to increase as the DNA circle size decreases. However, experiments with yTopo II and Topo IV show that the topology simplification activity decreases with circle size for small DNA circles and is independent of circle size for larger DNA circles.

The ensemble of the available evidence from previous studies and from the measurements of the bend angle presented here suggests that the bend angle model cannot fully account for the observed non-equilibrium relaxation activity of type IIA topoisomerases. However, it is possible that non-equilibrium relaxation results from G-segment bending in combination with a second mechanism. All three topoisomerases were found to impose comparable bends onto DNA, which suggests that the bend angle

model is incapable of explaining the measured differences between the topology simplification abilities of these three enzymes. However, these bend angles are somewhat consistent with the degree of bending expected from the least capable topology simplifier, yTopo II. Thus, it is conceivable that DNA bending is a conserved mechanism that is able to account for the base level of topology simplification achievable by type IIA topoisomerases. Further levels of topology simplification, as found in Topo IV and hTopo IIα, must arise from an additional enzyme specific mechanism, likely unrelated to DNA bending.

3.6 Conclusions/Discussion

We have shown that the DNA bend angles imposed by Topo IV, hTopo IIα, and yTopo II are similar and are not correlated with the extent of their topology simplification activities. This result is inconsistent with the bend angle model, in which the degree of topology simplification scales with the magnitude of the imposed bend angle (60). The relationship between topology simplification and bend angle determined by Klenin *et al.* (60) suggests that Topo IV should impose the largest bend angle (~310°), hTopo IIα should impose a smaller angle (~230°), and yTopo II should impose the smallest angle (~100°). (A detailed description of the derivation of the relationship between predicted bend angle and topology simplification are described in Appendix D.) However, our AFM and single molecule FRET data indicate that the three topoisomerases impose similar bend angles. Our AFM data suggested that yTopo II imposed the largest bend angle (100 ± 7°), followed by hTopo IIα (95 ± 24°), and lastly Topo IV (94 ± 13°). Our FRET data suggest larger angles of 140 ± 16° for yTopo II, 136 ± 17° for hTopo IIα, and

126 ± 18° for Topo IV (Table 3.3.1, Figure 3.6.1). Within each technique, all three bend angles are within 15° of one another, which we consider to be within our experimental uncertainty. Also, the angles follow the opposite order of the predicted bend angles, and there is no evidence of the ~3-fold difference in bend angles required by the bend angle model (Figure 3.6.1) (60). This leads us to conclude that while DNA bending is prevalent in all topoisomerases and may be an indicator of some conserved topology shifting mechanism, bending alone, within the context of the bend angle model, cannot solely explain topology simplification by type IIA topoisomerases.

Though AFM measurements have consistently been shown to accurately measure protein-DNA interactions and conformations (83,84,94,99,100,103), we verified that deposition conditions favored 2-D equilibration of the DNA molecules on the mica surface and hence that the data accurately represent the conformations of both the DNA and the protein-DNA complexes (78,96,104) (Figure 3.4.1 and Table 3.4.1). 2-D DNA equilibration is further supported by the agreement of bend angles determined by tangent measurements (both manual and automated) and EED measurements. Furthermore, the lack of correlation between the height of the DNA segments emerging from the protein and the measured bend angle is additional evidence that the protein-DNA complex equilibrated in 2-D Figure 3.4.2.

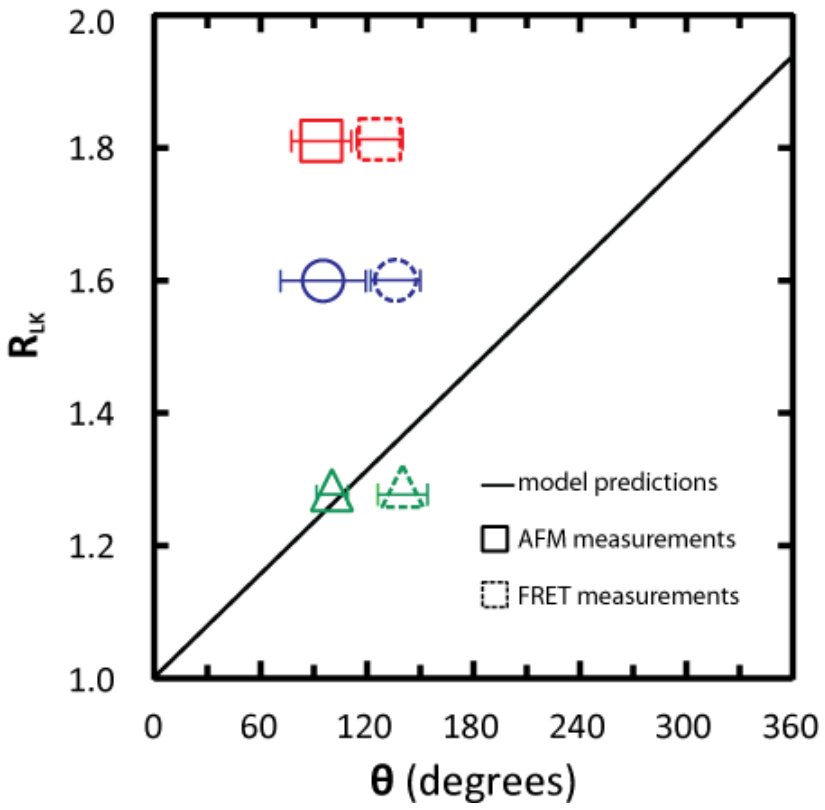

Figure 3.6.1 Comparison of measured and predicted bend angles imposed by type IIA topoisomerases. Shown is a plot of topology simplification ability (R_{LK}) as a function of measured and predicted bend angles for Topo IV (red squares), yTopo II (green triangles), and hTopo IIα (blue circles). Bend angles measured from AFM images (outlined shapes) and FRET efficiencies (dashed outlined shapes) are plotted along with predicted bend angles extrapolated from the bend angle model (60) (line) using the non-equilibrium unknotting and supercoil relaxation data from Rybenkov *et al.* (35).

Although direct visualization of DNA-type IIA topoisomerase complexes and measurement of bend angles have not been previously reported, other methods, such as protein-DNA co-crystalization, single molecule DNA manipulation, and DNA cyclization have been employed to probe topoisomerase-induced DNA bending. Crystal structures of several type IIA topoisomerase-DNA complexes have been reported in the literature. These include the TOPRIM fold, which is a conserved domain required for DNA cleavage, and primary DNA-binding domain of yTopo II (63,74), the breakage-reunion and TOPRIM domains of *S. pneumoniae* topoisomerase IV in the presence of the quinolones moxifloxacin and clinafloxacin (64), and the ParE28-ParC58 fusion of *Acinetobacter baumannii* topoisomerase IV in the presence of the quinolone moxifloxacin (66). The yTopo II-DNA structure reported a DNA bend angle of ~150°, and we estimated similar bend angles from the *S. pneumoniae* topoisomerase IV-DNA crystal structure and the *A. baumannii* topoisomerase IV-DNA crystal structure. In fact, the bend angle imposed on DNA by *A. baumannii* topoisomerase IV, which has a high degree of sequence identity (61%) with *E. coli* Topo IV, was slightly smaller than the bend angle imposed on DNA by yTopo II, which is consistent with our results.

Our measurement of the bend angle imposed by yTopo II from AFM images ($100 \pm 7°$) is smaller than the angle measured from the crystallized protein-DNA complex, though the angle measured from FRET experiments ($140 \pm 16°$) is much closer to this value (~150°) (63). The discrepancy could arise from several effects, including different buffer conditions used in AFM and single molecule FRET experiments that could have affected the bend angles. FRET experiments were performed under the exact buffer conditions as the relaxation assays whereas AFM experiments had to be performed

in a buffer optimized for AFM deposition. We observed that monovalent salt concentration, in particular, had a strong influence on bend angle in our single molecule FRET experiments (data not shown). Regardless of the discrepancies, our AFM and FRET data both show that type IIA topoisomerases bend DNA to a similar extent. This result is consistent with published DNA-topoisomerase crystal structures, which show that all crystallized protein-DNA complexes reveal comparable DNA bending by type IIA topoisomerases from very different organisms (63-66,74). Though the exact role of DNA bending in the mechanism of type IIA topoisomerases has not been determined, one study suggests that these enzymes require the DNA to be under considerable strain in order for cleavage to occur (105). Perhaps DNA bending provides the necessary distortion of the double helix that allows the cleavage reaction and thereby the relaxation reaction to proceed.

The extent of DNA bending by Topo IV has also been estimated from single molecule measurements of the size of plectonemic loops in supercoiled DNA with Topo IV bound, which indicate that Topo IV imposes a radius of curvature of ~6.4 nm onto DNA (75). The radius of curvature can be related to a bend angle given assumptions about the distance over which the circular curvature approximation holds. A reasonable assumption is that the radius of curvature holds for an arc length equal to the number of DNA base pairs that interact with the protein. Estimating this length from footprinting data showing ~34 bp of protected DNA (82), we calculated the bend angle could be as large as ~135° (assuming the protein bends the DNA over 45 bp) or as small as ~75° (assuming the protein bends the DNA over 25 bp). Our measured angle for Topo IV is consistent with this range. It should also be noted that the radius of curvature determined

from the magnetic tweezers experiment is not consistent with a bend angle larger than 180° and certainly not as large as the ~310° angle suggested by the bend angle model. DNA bending by type IIA topoisomerases has also been probed through DNA cyclization experiments (59,61). Though these experiments have shown that Topo IV bends DNA and yTopo II does not, we noted in our AFM images, and others have observed (62), that type IIA topoisomerases have a high affinity for DNA ends. This renders the cyclization data difficult to interpret since the presence of a topoisomerase on the ends would likely confound the ligation reaction necessary to achieve cyclization.

Several other models have been proposed to explain the topology simplification mechanism of type IIA topoisomerases (62). A tracking model proposes that the enzyme binds to a DNA crossing and tracks along the DNA to trap T-segments that are catenated or knotted (35). However, an experiment that placed tightly bound protein "roadblocks" at several locations along supercoiled circular DNA did not affect non-equilibrium supercoil relaxation (27). A three segment binding model postulates that the topoisomerase binds two potential T-segments prior to selecting one for strand passage based on local geometry (61). However, this model predicts an asymmetric removal of positive versus negative supercoils that would result in a skewed topoisomer distribution, which we did not observe for any of the type IIA topoisomerases studied (Figure 1.6.1). Other studies have also failed to detect asymmetric supercoil removal by type IIA topoisomerases (27), so while this model may hold in certain cases, it does not explain the more general mechanism of topology simplification. Two compelling possibilities are the hooked juxtaposition model and the kinetic proofreading model. The hooked juxtaposition model postulates that type IIA topoisomerases detect and relax specific

juxtapositions of catenated, knotted, and supercoiled DNA in which the G- and T-segments are bent towards one another (57). Simulations based on lattice and WLC models indicate that strand passage at these hooked juxtapositions is sufficient to produce non-equilibrium topology simplification (67-71). The kinetic proofreading model suggests that upon binding to the G-segment of DNA and encountering an initial T-segment, the topoisomerase becomes transiently activated, perhaps by binding one of the two ATP molecules. The T-segment is released and strand passage will occur if a second T-segment is captured while the enzyme remains in the active state (58,72). It is possible that one of these models, perhaps coupled with the small effect arising from the bend angles imposed by the topoisomerase, could account for the non-equilibrium topology simplification activity of type IIA topoisomerases. The relatively sharp bend imposed on the G-segment DNA by type IIA topoisomerases is consistent with the hooked juxtaposition model, though it remains to be determined if bent T-segments are preferentially captured and passed. Further experiments are necessary to test these models to determine which, if either, can explain this fascinating phenomenon.

Chapter 4: Kinetic Proofreading by Type IIA Topoisomerases

4.1 The Kinetic Proofreading Model

Several models have been proposed to attempt to characterize the mechanism of energy coupling to topology simplification. Two of the contenders, a DNA tracking model and a bend angle model, have been disproved experimentally (27,50). Two others, a kinetic proofreading model and a hooked juxtaposition model, remain to be tested to see which, if either, correctly characterizes the energy-dependent topology simplification by type IIA topoisomerases.

The kinetic proofreading model, proposed by Yan *et al.,* features a two step activation process for the topoisomerase in which a random occurrence, in this case an interaction between the topoisomerase and a prospective T-segment must occur twice before the process of strand passage is initiated (58,72). The term "kinetic proofreading" was coined by J.J. Hopfield (106) who showed that a multiple step binding process, with each step separated by an irreversible process, could explain why some biological binding processes are far less error prone than would be expected based on the free energy difference between "correct" and "incorrect" binding. In essence, the requirement of a second binding encounter "proofreads" the first step by amplifying the probability that strand passage will occur if the T-segment and G-segment are topologically constrained with respect to one another, i.e. linked, catenated, or supercoiled. The schematic for this model, shown in Figure 4.1.1, demonstrates how kinetic proofreading would work in the case of a single trefoil knot (58,72).

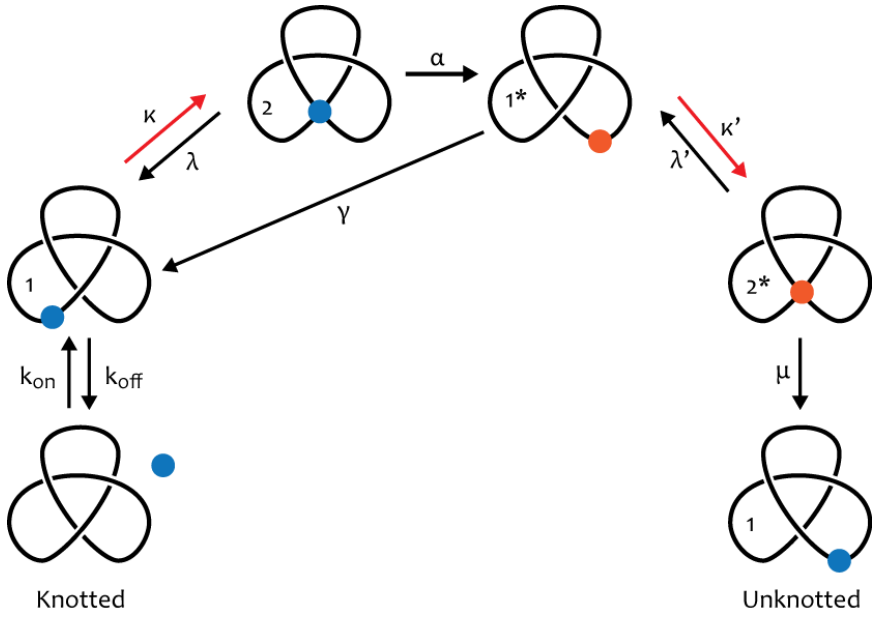

Figure 4.1.1 A schematic for the kinetic proofreading model (58,72). In this model, a topoisomerase, shown initially in blue, binds to a DNA molecule in a trefoil knot topology with binding constant k_{on}. Once bound, the topoisomerase will encounter a putative T-segment at a rate κ, which is dependent on topology. Upon this initial encounter with a possible T-segment, the topoisomerase becomes activated with a topology independent rate of α. If, prior to decaying back to the inactive state at a topology independent rate of γ, the topoisomerase encounters a second possible T-segment at a rate κ', it will initiate strand passage with a topology independent rate of μ. Topology dependent rates are shown with red arrows and topology independent rates are shown with black arrows. According to this model, the overall rate of strand passage (R) is proportional to $\kappa \cdot \kappa'$. Given that the topology and thermal fluctuations are the same at both topoisomerase-DNA encounters, $R \propto \kappa^2$. [Adapted from (58)]

According to the kinetic proofreading model, a topoisomerase, indicated initially by a blue circle, binds to a DNA knot. This step, like all other steps indicated with a black arrow, is independent of the DNA's topological state. Once bound, the topoisomerase will either unbind (with a rate of k_{off}) or capture a potential T-segment (with a topology dependent rate of κ). At this point, the topoisomerase will dissociate from this potential T-segment and may become "activated" through a topology independent, irreversible process with a rate of α. The authors suggest that this step could arise from the binding of one of the two requisite ATP molecules (58,72). However, the binding of one ATP molecule has been linked to the closing of one half of the N-gate, which could be problematic for this model, as a partially closed N-gate would serve to block a substantial portion of the T-segment binding site. (Figure 1.5.2) (45,107,108). Once the topoisomerase has been activated, it can either encounter a second potential T-segment (with a topology dependent rate of κ'), or decay back into its inactive state (with a rate of γ). Hence, strand passage by the topoisomerase would require two topology dependent steps making the overall rate of strand passage proportional to $\kappa \cdot \kappa'$, rather than just κ. Assuming that the topology and thermal fluctuations would be the same for both encounters between the G-segment bound topoisomerase and potential T-segments, $\kappa \cdot \kappa'$ would simplify to κ^2.

In this study, we used magnetic tweezers to test the model of kinetic proofreading. For these experiments, we double tethered a magnetic bead to a coverslip with two parallel DNA molecules. By rotating the magnets in the magnetic tweezers setup, we were able to rotate the bead and vary the proximity, and hence, the collision rate between the two DNA molecules. As shown in Figure 4.1.2, when a topoisomerase acts on a DNA

crossing, the strand passage reaction results in a measurable height change of the bead. Although a crossing of one full turn is shown in the figure, smaller and larger rotations can also create DNA crossings that can be relaxed (in steps of 1 turn) by type IIA topoisomerases. We measured the time for strand passage by Topo IV at multiple bead rotations, ranging from -0.6 turns to -1.4 turns, for several different double tether geometries. Then, we used simulations to determine the collision probability of the two DNA molecules at each rotation for each double tether geometry. This allowed us to determine how the rate of strand passage by Topo IV was dependent on the collision probability of the DNA molecules. By measuring both the rate of strand passage and collision probability for multiple rotations and geometries, we were able to characterize the relationship between the rate of strand passage and the collision probability of the two DNA molecules. This allowed us to determine whether the relationship was quadratic, as predicted by the kinetic proofreading model, linear, as would be expected for a single step binding process, or some higher order polynomial, which could be indicative of a more complicated kinetic scheme.

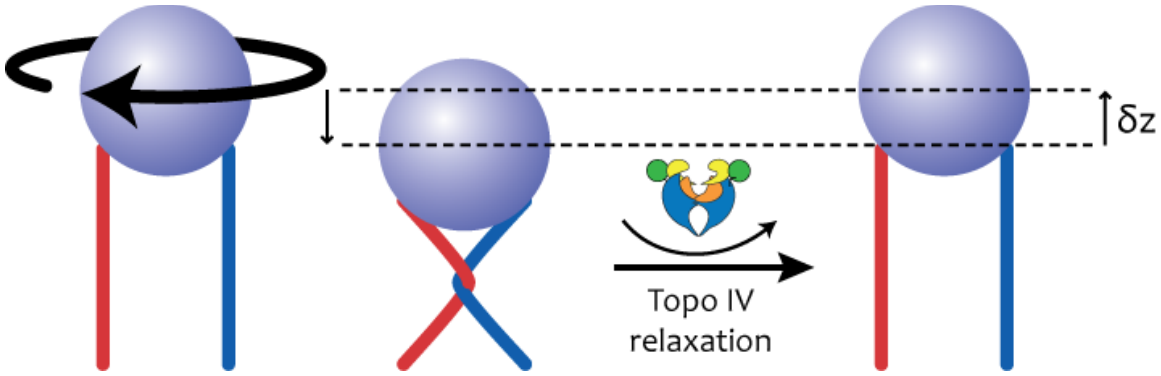

Figure 4.1.2 Cartoon showing Topo IV acting on a doubly tethered paramagnetic bead in a magnetic trap. Here, the bead has an imposed rotation of n = -1. When the topoisomerase acts, it increases n by 1, hence returning the DNA to its original parallel conformation with a measureable change in extension of δz.

4.2 Methods

4.2.1 Magnetic Tweezers Experimental Setup

Magnetic tweezers, are powerful tools for manipulating and probing DNA topology at the single-molecule level. Magnetic tweezers utilize two small magnets, with their opposite poles separated by a small gap of ~1 mm (109), whose height relative to the flow cell can be precisely controlled. When one end of two parallel linear DNA molecules are tethered to the surface of a flow cell and the other ends are anchored to a paramagnetic bead, a controlled force can be applied to, and a rotation imposed on, the DNA molecules by adjusting the position of the magnets relative to the flow-cell and the rotation of the magnets, respectively (Figure 4.2.1). This allows precise control over the topology and measurement of the extension of the DNA molecule. The position of the bead can be determined by video tracking, which is based on the appearance of the bead's concentric diffraction rings. Video tracking works by first creating a calibration of the diffraction pattern of the bead as it is moved through precise steps in the vertical direction. This calibration creates a set of images that can be compared with the diffraction pattern of the bead during the experiment to determine its distance from the focal plane. Magnetic traps can impose forces ranging from a few fN to more than 100 pN (110,111) and can measure the axial displacement of the bead with ~ nm accuracy at 100 Hz (110).

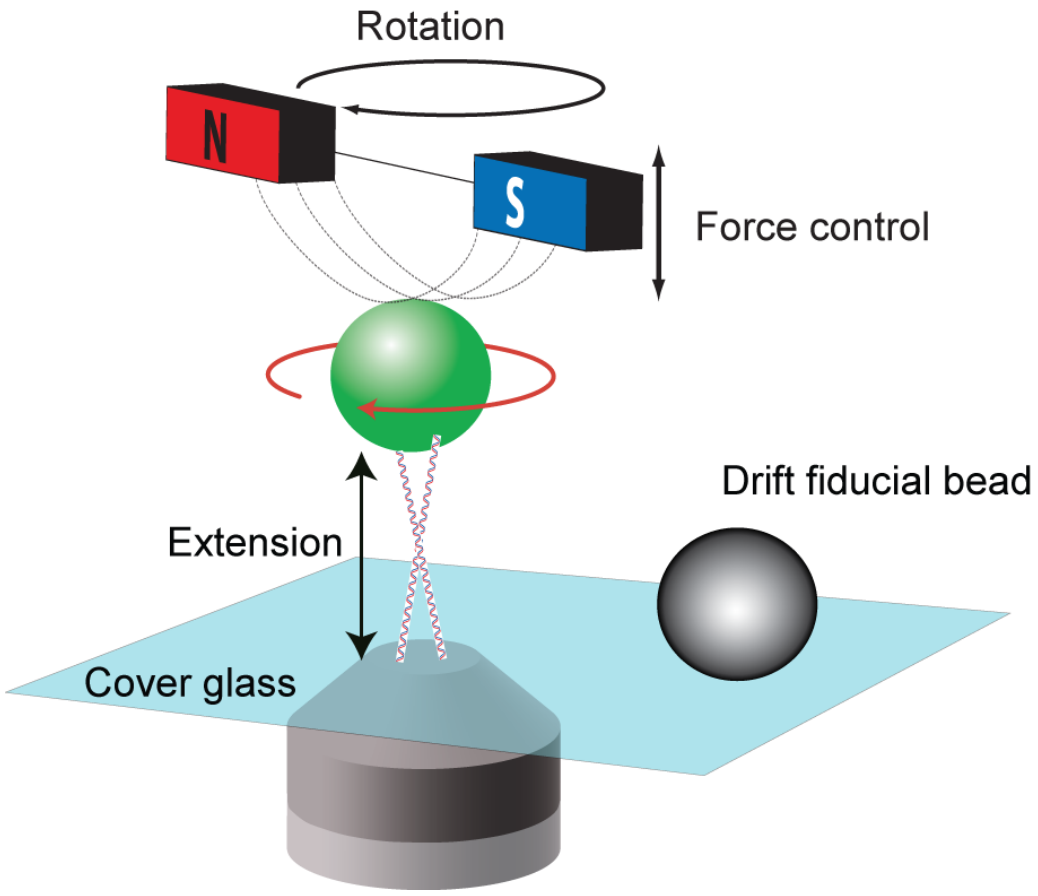

Figure 4.2.1 Diagram of a magnetic bead double tethered by DNA molecules in a magnetic trap (not to scale). Magnets, shown in red and blue, are separated by a small gap. Rotation of the magnets induces a rotation in the paramagnetic bead which, in turn, twists the DNA molecules around one another. DNA molecules are attached to the cover slip using a digoxigenin-antidig linker and to the bead via a biotin-streptavidin linker. The rotation of the bead is known and the extension of the DNA molecules can be measured by video tracking, where the diffraction pattern of the bead is compared with a set of calibration images to determine the height of the bead relative to the focal plane, and using a stuck bead as a fiducial marker to eliminate drift.

We created our DNA substrate using commercially available custom DNA oligos modified to contain either a biotin or digoxigenin molecule as forward and reverse primers, respectively, in a PCR reaction with the pFC-94 plasmid (112) as the template. The resulting DNA substrate was 4.1 kb in length and contained a digoxigenin on one end and a biotin on the other. In our DNA micromanipulation experiments, one end of the DNA molecule was tethered to the surface of an antidig coated glass coverslip via a digoxigenin-antidig linker motif and the other end was anchored to a streptavidin coated magnetic bead through the biotin-streptavidin linker motif.

Tethered 1 μm paramagnetic beads (Dynabeads® MyOne™ Streptavidin C1, Invitrogen) were first tested to determine if they were attached to the surface by one or more DNA molecules by rotating the bead and monitoring the extension. Beads tethered by a single DNA molecule are insensitive to rotation because the linkages are rotationally unconstrained, whereas a bead tethered by multiple DNA molecules will decrease in height due to the twisting of the DNA molecules around each other. Once a double tether was confirmed, an extension vs. rotation curve was generated for double-tethered bead (Figure 4.2.2). This plot, called a hat curve, could be fit by Equations [4.2.1] and [4.2.2],

$$L = \sqrt{L_0^2 - 4e^2 \sin^2(n\pi)} - r + \sqrt{r^2 - e^2}, \quad |n| < 0.5 \qquad [4.2.1]$$

$$L = \sqrt{L_0^2 - (2e + \pi D_e(|n| - \frac{1}{2}))} - r + \sqrt{r^2 - e^2}, \quad |n| > 0.5 \qquad [4.2.2]$$

where L is the measured extension, L_0 is the maximum extension, e is one-half the DNA molecule separation, n is the rotation, r is the bead radius, and D_e is the effective DNA

diameter. An analysis of the hat curve by fitting to these equations allowed for the determination of the $2e/L$ parameter that defines the geometry and was used in the simulations. All hat curves were generated using a 2 pN force and beads with asymmetric hat curves were not considered, as they were likely not tethered by two parallel DNA molecules.

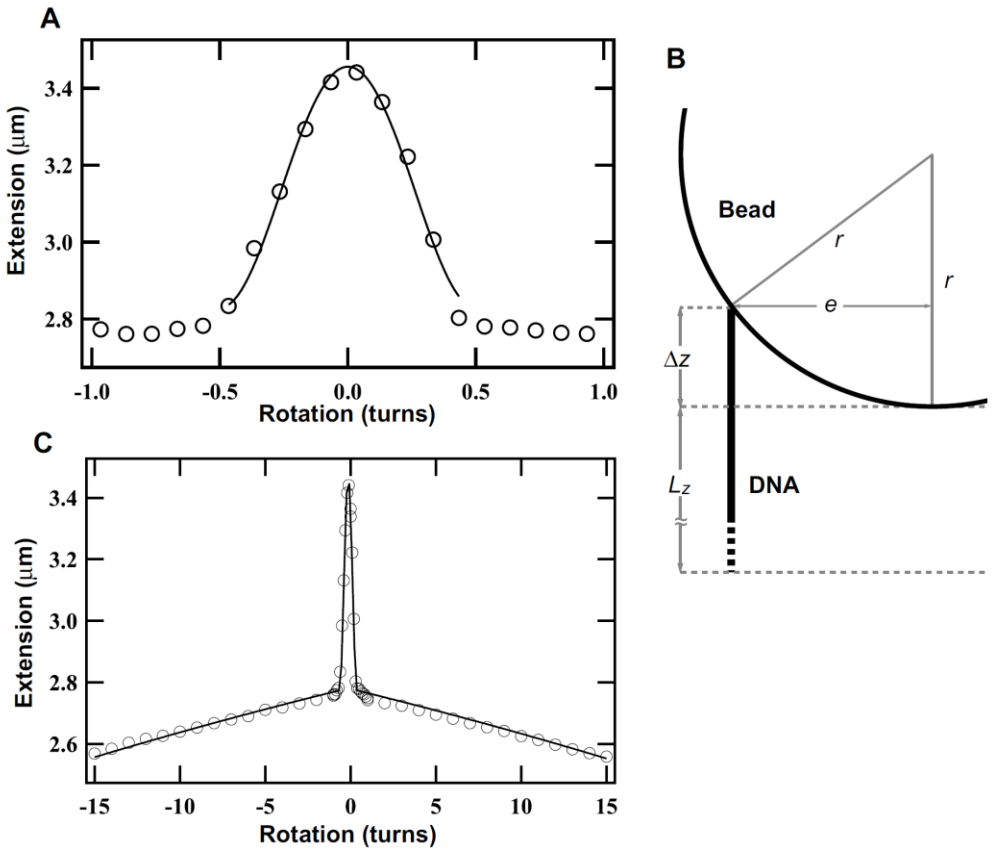

Figure 4.2.2 A sample extension vs. rotation "hat" curve. **A.** The hat curve is fit to a geometric model plus two terms that correct for the spherical shape of the bead as shown in Equation [4.2.1] (113), where L is the measured extension, L_0 is the maximum extension, e is one-half the DNA molecule separation, n is the rotation, and r is the bead radius. Equation [4.2.1] is applicable for rotations from -0.5 to 0.5 turns. **B.** The origin of the correction terms for a spherical bead. Since the extension of the bead is measured at its lowest point, a correction term is necessary to account for the distance between the end of the DNA molecule and the bottom of the bead (Δz). **C.** For rotations with $|n|$ larger than 0.5 turns, the hat curve can be fit with a geometric winding model as shown in Equation [4.2.2] (113,114). Here D_e is the effective DNA diameter. [Figure S2 from (101), Copyright (2009) National Academy of Sciences, USA. Permission not required]

Once the double tether was fully characterized, Topo IV was injected into the flow cell, achieving a final concentration of around 2 nM, which is well above its K_d of ~ 0.15 nM (75) and ensured that the DNA collisions would be the rate limiting step, rather than Topo IV binding. The magnets were rotated by -*n* turns and when Topo IV performed strand passage, thus increasing *n* by one, the extension increase was automatically detected (Figure 4.1.2) and the bead was rotated one full turn to return it to the pre-relaxation conformation. This was repeated for 100-200 strand passage events. Then, the bead rotation was "zeroed out" and the DNA molecules were returned to their original parallel conformation. From this point, a new, second rotation was imposed and the process was repeated. Each double tether was subjected to a variety of rotations, generally ranging from -0.6 to -1.4 turns.

The extension vs. time traces were processed such that each strand passage event was manually fit with a user driven step finding function where $t_{1/2}$ was the time at the midpoint of the extension transition. The time to strand passage, t_{relax}, was defined as the time lag between the bead rotation and $t_{1/2}$ (Figure 4.2.3). For each tether, relaxation experiments were performed at n = -0.8, -1, and -1.2 turns. Relaxation experiments were also performed at n = 1.4 for most tethers and at -0.6 for two tethers. It was very difficult to detect relaxations at -0.6 turns because a strand passage event would result in a new *n* of +0.4 turns, and a net difference of only 0.2 turns yielded a very small net extension change. The trace shown in Figure 4.2.3 is an example of data collected for a rotation of n = -1 turn. While the steps in this case appear obvious, the transition from n = -0.6 to 0.4 would produce an extension change of roughly one-fifth the size shown, making automatic detection of strand passage unreliable for many geometries.

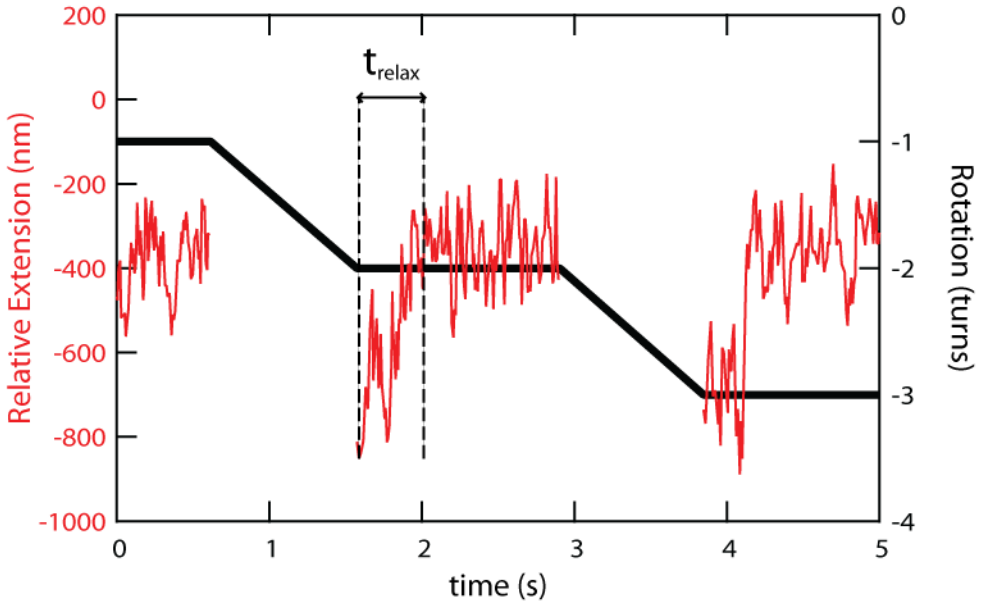

Figure 4.2.3 Sample plot of extension vs. time and rotation vs. time for an unlinking experiment. Here, t_{relax} is measured from the time the bead has achieved the full imposed number of turns until the midpoint of the transition that occurs when the topoisomerase acts relaxes the crossing. See Appendix E for further relaxation traces.

4.2.2 Simulations

Simulations were performed using a DNA Metropolis Monte Carlo (MC) algorithm that has been previously published (101,102,114,115). Briefly, two ~1.35 μm self-avoiding discrete wormlike chains (WLCs) were modeled to represent two 4.1 kb DNA molecules. These chains were held a distance of 2*e* apart, where the ratio of separation to length (2*e*/*L*) was determined experimentally. A rotation, ranging from 0.6 to 1.4 turns was initially imposed upon the chains, and the algorithm generated distributions of roughly 10^8 chain conformations. The topology of the chains was maintained by eliminating moves that altered the initial topological constraints. A juxtaposition event was determined to occur when the chains passed within 10 nm of one another. For each 1000 simulation steps, information about the juxtapositions, such as number of juxtapositions, number of non-juxtapositions (from which the probability of at least one juxtaposition occurring could be calculated), average angle of juxtaposition, and the vector quantities of the chains including the point of juxtaposition and ±3 WLC segments, was recorded for each experimentally determined tether geometry, force, and rotation set. Small perturbations in input parameters (5-10%) did not yield significant perturbations in the conformation distributions for either number of juxtapositions, probability of at least a single juxtaposition, or average angle of juxtaposition.

4.3 Results

4.3.1 Relaxation by Topo IV for Different DNA geometries and rotations

As shown in Figure 4.2.2, rotation vs. extension hat curves for a double tethered DNA molecules have a well defined shape that is well fit by in a piecewise manner by

Equations [4.2.1] and [4.2.2]. The fit to this curve allows extraction of the $2e/L$ parameter, which defines the geometry and is a necessary input for the MC simulations. Of the twelve prospective double tethers that relaxation data was collected for, six were found to have symmetric hat curves that could be well fit. The distribution of relaxation times were exponentially distributed and were well fit by a single decaying exponential. Figure 4.3.1 shows representative example of the relaxation data for a single geometry and crossing. In general, we found that the characteristic relaxation time was proportional to the inverse of the rotation for rotations of -0.6, -0.8, and -1 turns, and that the relaxation time tended to saturate at around -1 turn, so characteristic relaxation times for -1.2 and -1.4 turns were similar to and often within error of the characteristic relaxation time for -1 turn, though some tethers behaved unpredictably. Figure 4.3.2 shows data from the two tethers that contained data for the n = -0.6 turns rotation and a third tether that exhibited similar behavior. We decided to include only these tethers in our kinetic proofreading analysis for multiple reasons: two of the three data sets contained the critical and elusive n = -0.6 turns data point, their hat curves were among the most symmetric, their data sets were among the most straight-forward to analyze due to relatively large extension changes, and the three discarded tethers behaved in a markedly non-physical manner when compared with the simulation data. Though unfortunate, it was not entirely surprising that only three of twelve data sets were useable. These are very difficult experiments to perform and the data can be difficult to analyze when the extension changes are small. Further, it is very difficult to find a tether with a perfectly symmetric hat curve that can be well fit to Equations [4.2.1] and [4.2.2].

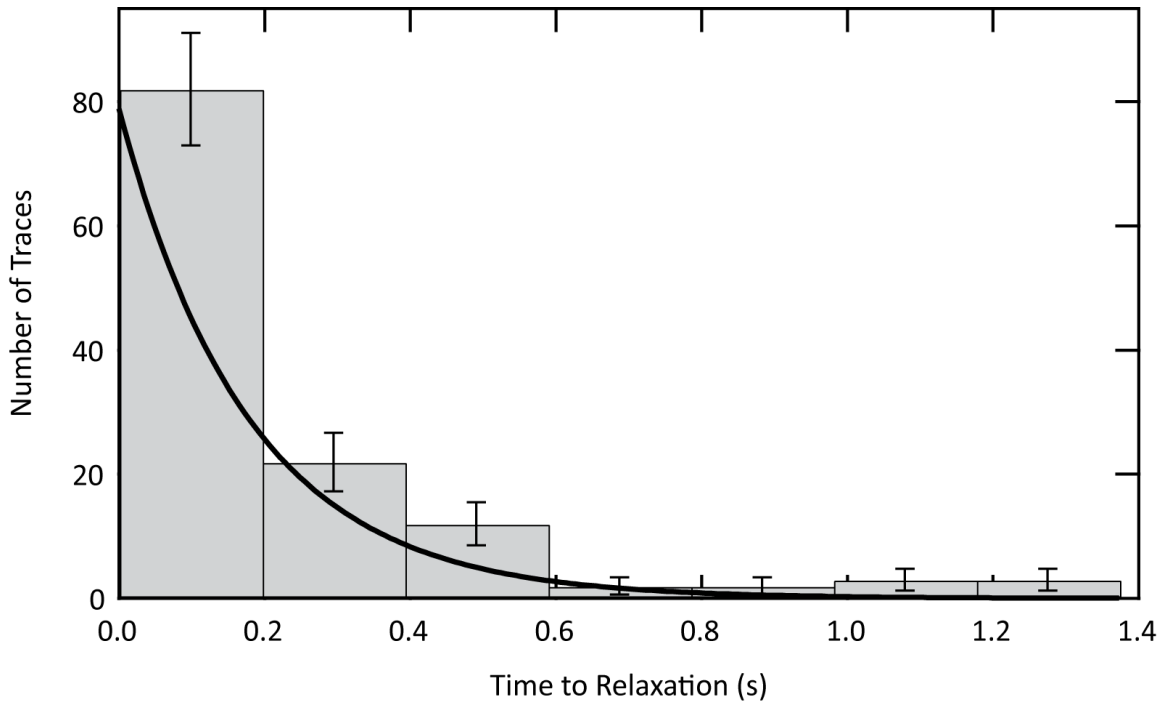

Figure 4.3.1 Sample relaxation data for a tether with $2e/L = 0.65$ and $n = 1$ turn, fit to a single exponential function. The characteristic time for this fit was $\tau = 0.18 \pm 0.02$ s. The number of bins for this and every data set was determined using the Sturges formula: $N_{Bins} = 1 + \log_2(N)$, where N is the number of data points (116).

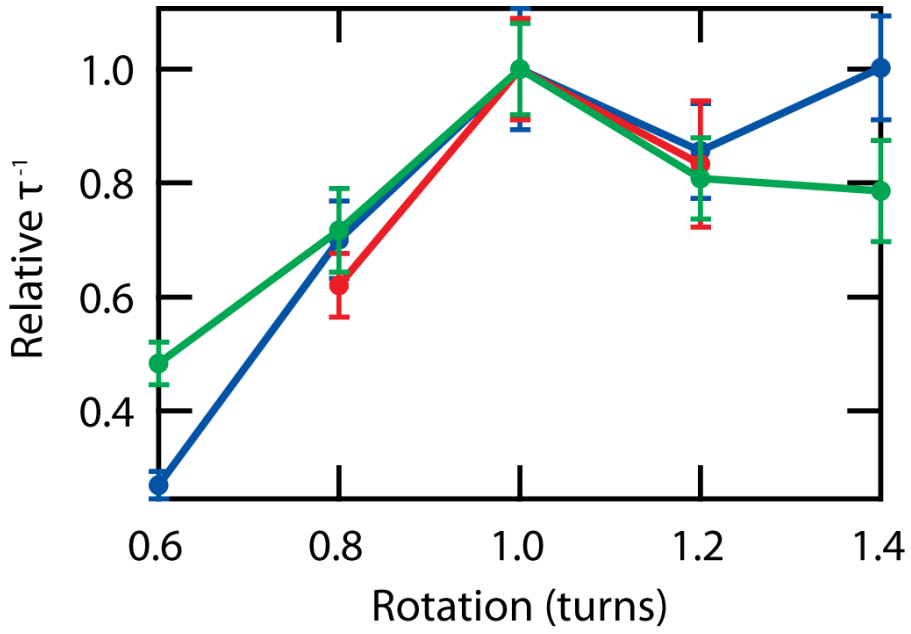

Figure 4.3.2 Plot of relative τ^{-1} (relaxation rate) values (normalized by τ^{-1} at $n = 1$ turn) vs. rotation for three different double tethers with geometries: $2e/L$ = 0.52 (red), 0.65 (blue), and 0.62 (green). For these tethers, the relaxation rate by Topo IV increased with increasing number of turns until $n = 1$ turn, at which the relaxation rate saturated.

4.3.2 Relationship between Rotation and Collision Probability

The kinetic proofreading model postulates that the relaxation time for a type II topoisomerase should scale as the square of the juxtaposition probability of two DNA segments. As such, previously published MC simulations (101,102,114,115) were used to simulate DNA molecules and determine the relative probabilities of collision for different double tether geometries and bead rotations. The simulations returned two types of data for each 1000 simulation steps that correspond to juxtaposition probability: the number of juxtapositions (N_{juxt}) and the number of non-juxtapositions (N_{nojuxt}). The number of non-juxtapositions gives the probability of at least one juxtaposition occurring over the 1000 steps, since $P_{juxt} = 1 - N_{juxt}/1000$. Further, these simulations yielded a distribution of crossing angles for each geometry. This information could be related to the juxtaposition and non-juxtaposition data to yield the number of juxtapositions (N_{ang}) or probability of a single juxtaposition (P_{ang}) at any range of crossing angles. Since Topo IV has been shown to prefer a crossing angle of ~85° (101), N_{ang} and P_{ang} at a crossing angle between 80° and 90° were considered in addition to N_{juxt} and P_{juxt}. Simulation data were all normalized to the $n = 1$ data point in the same way as the experimental data were normalized. Figure 4.3.3 shows the four normalized juxtaposition probability measurements vs. rotation for a single tether overlaid with the normalized experimental data.

As exhibited in Figure 4.3.3, the experimental data shown best correlates with N_{juxt}. The experimental data from the two other tethers shown in Figure 4.3.2 also correlate best with the N_{juxt} simulation values for those tethers. Figure 4.3.4 shows a plot of all three tethers that were considered and the corresponding normalized N_{juxt} simulation data.

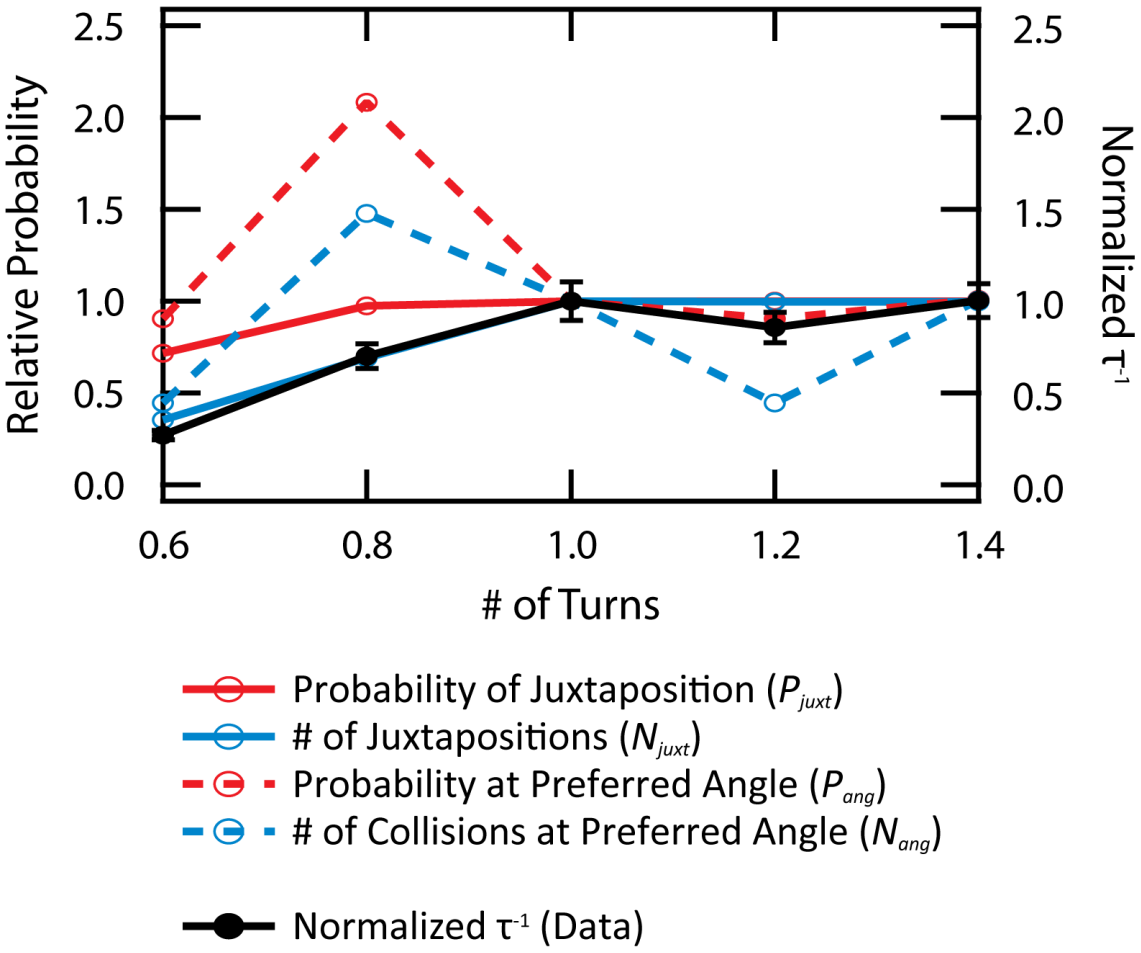

Figure 4.3.3 Plot of the four different juxtaposition probability measures and the τ^{-1} experimental data vs. rotation, all normalized to the $n = 1$ turn data point.

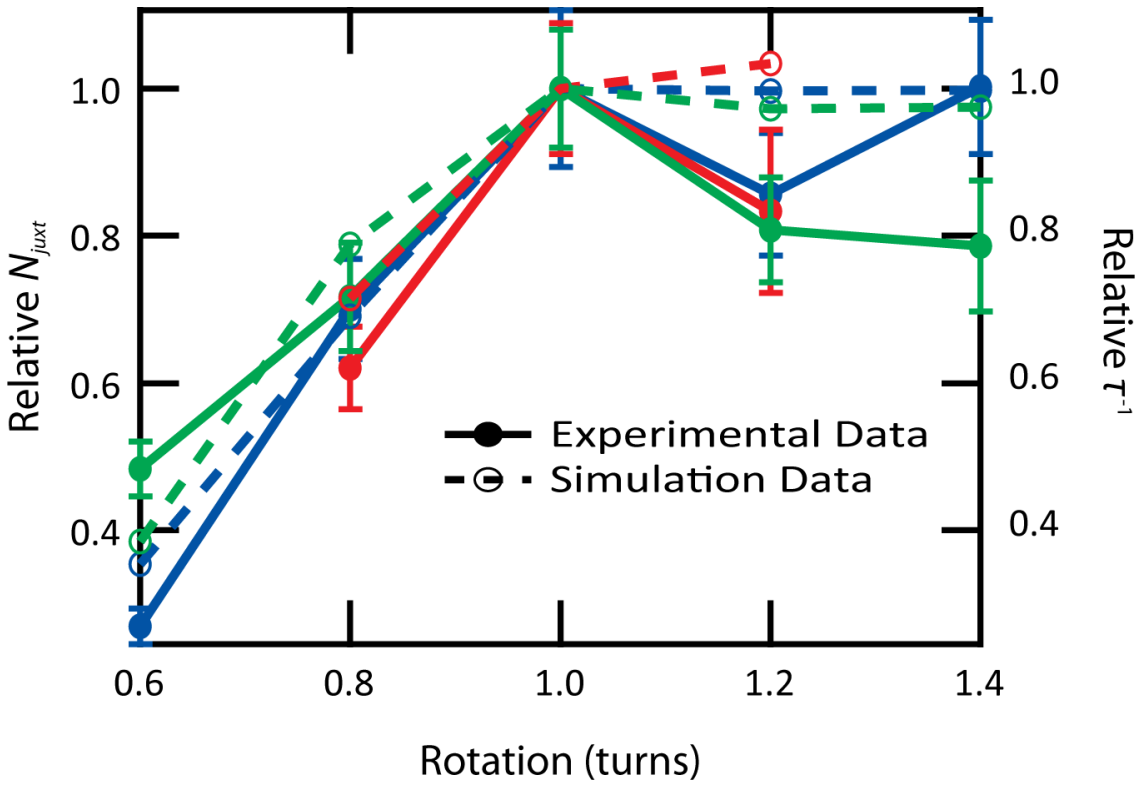

Figure 4.3.4 Experimental and simulated N_{juxt} data for three different tether geometries: $2e/L$ = 0.52 (red), 0.65 (blue), and 0.62 (green)..

4.3.3 Strand Passage rate by Topo IV is Linearly Correlated with Collision Probability

As shown in Figure 4.3.4, the relaxation rates for all three tethers appear to match the trend of the N_{juxt} simulated data. This immediately suggests that the relationship between τ^{-1} and N_{juxt} is probably closer to a linear relationship than the quadratic relationship predicted by the kinetic proofreading model. Shown in Figure 4.3.5 is a plot of the experimental data as a function of the simulation data for all three tethers. Three possible fits to the data are presented: a linear fit (red), quadratic fit (blue) and a power fit (green). Qualitatively, the linear fit is much better than the quadratic fit. Quantitatively, when the data is fit with a power function, the fit parameter returns a power of 0.906 ± 0.15, which is a clear indication of a linear or near-linear relationship between the relaxation rate and the juxtaposition probability.

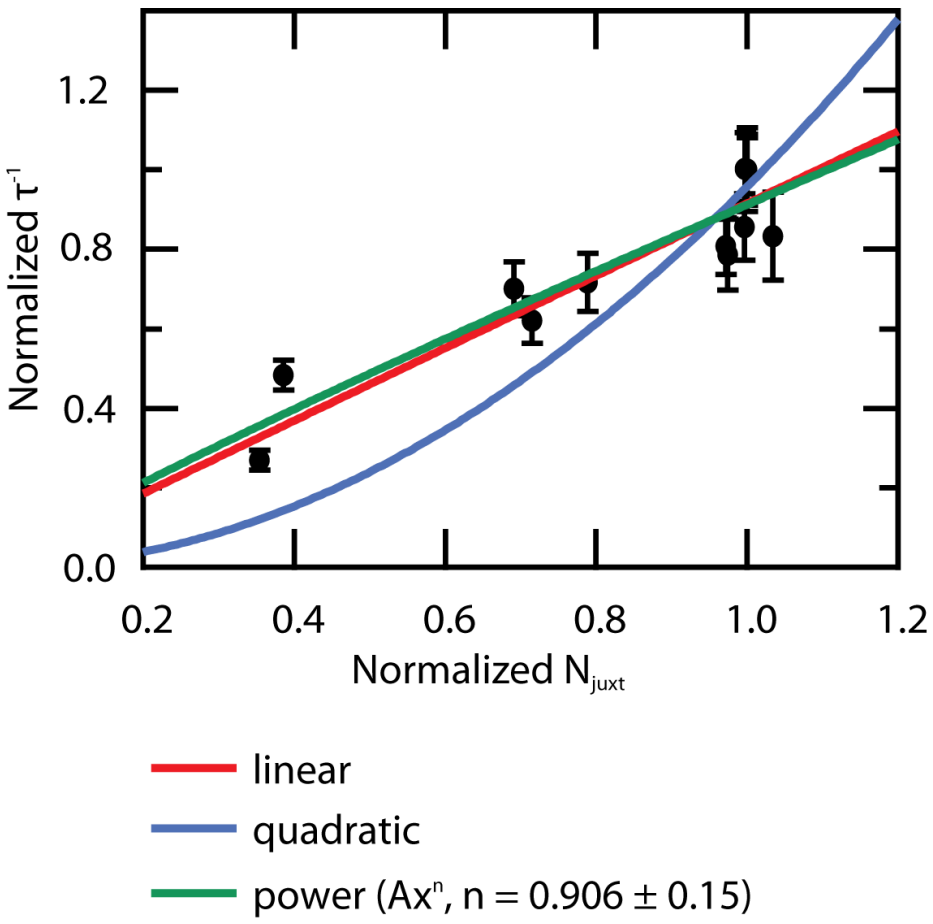

Figure 4.3.5 Plot of normalized τ^{-1} as a function of N_{juxt}. Although the kinetic proofreading model predicts that the relationship between inverse relaxation time and rate of DNA segment juxtaposition should be quadratic, our data show that the relationship is linear.

4.4 Conclusions/Discussion

The kinetic proofreading model predicts that the relationship between the rate of a relaxation event occurring and the rate of strand collision should be quadratic. However, our data show that the relationship between the relative inverse time to relaxation of a DNA crossing by Topo IV is linearly related to the relative number of DNA segment juxtapositions. The inverse relative time to relaxation of a DNA crossing, τ^{-1}, is the relative rate of strand passage. Likewise, the rate of collision of two DNA segments separated by a distance of 2*e* and twisted around one another by a rotation of *n* turns is linked to the number of DNA juxtapositions at equilibrium. The higher the collision rate, the more juxtapositions should occur in direct proportion. Hence, our data, which indicate that τ^{-1} and N_{juxt} are linearly related, are not consistent with the kinetic proofreading model.

Because Topo IV is the most capable topology simplifier (Figure 1.6.1, Figure 3.6.1), if the kinetic proofreading model described topology simplification by type IIA topoisomerases, the effects would be most pronounced in the case of Topo IV. Since our data with Topo IV indicate a linear, rather than quadratic, relationship between the rate of strand passage and the topology-dependent rate of DNA segment collisions, we must conclude that the kinetic proofreading model does not accurately characterize how type IIA topoisomerases couple the energy of ATP hydrolysis to preferential strand passage aimed and simplifying DNA topology.

Now that the bend angle model and the kinetic proofreading model have been experimentally discounted, one promising model remains: the hooked juxtaposition model. This model states that type IIA topoisomerases have an inherent binding

preference for some DNA segment juxtapositions over others (57,67-71). Like the bend angle and kinetic proofreading models prior to this dissertation work, this model has not yet been experimentally tested. Fortunately, the MC simulations that yielded information about the relative number of juxtapositions also provided full characterization of the vector positions of each juxtaposed segment in the simulated DNA, as well as the vector positions of the three nearest neighbor segments on both sides of the juxtaposition on each chain. A future direction for this project would be to use the wealth of juxtaposition information obtained in the MC simulations to characterize the "hookedness" of juxtapositions in a uniform way and then to determine if the topoisomerase acts more efficiently on those DNA conformations than on conformations that do not have the preferred juxtaposition conformations.

Appendices

Appendix A: Permissions

Permission for Figure 1.2.1, Figure 1.2.2, Figure 1.3.1, Figure 1.3.2, Figure 1.3.3, and Figure 1.3.4

Hardin, Ashley (NIH/NHLBI) [F]

Subject: FW: Academic Permissions Request Form

From: Academic Permissions [mailto:Academic.permissions@oup.com]
Sent: Monday, October 31, 2011 5:38 AM
To: ahhardin@umd.edu
Subject: FW: Academic Permissions Request Form

Dear Ashley,
Thank you for your enquiry. You have our permission to use the OUP Material you list in your email below in your thesis for submission to The University of Maryland.

If at some future date your thesis is published it will be necessary to re-clear this permission.
Please also note that if the material to be used is acknowledged to any other source, you will need to clear permission with the rights holder.

Best wishes,

Ben Kennedy
Permissions Manager
Academic Rights & Journals
Permissions
Oxford University Press
Great Clarendon Street
Oxford
OX2 6DP
Direct tel. +44 (0)1865 354728
Direct fax +44 (0)1865 353429
e mail: ben.kennedy@oup.com

From: noreply@oup.com [mailto:noreply@oup.com]
Sent: 29 October 2011 19:04
To: Academic Permissions
Subject: Academic Permissions Request Form

0_URL	/academic/rights/permissions/request
Z_firstname	Ashley
Z_lastname	Hardin
Z_Company	The University of Maryland, College Park
Z_Address	204 Wendhurst Ct. Apex, NC
Z_zip	27502
Z_PhoneNo	919-623-2304
Z_country	USA
Z_FaxNo	
Z_Email	ahhardin@umd.edu
Z_VATnumber	
Z_TheirTitle	PhD Dissertation - USING SINGLE MOLECULE TECHNIQUES TO DETERMINE THE MECHANISM OF TOPOLOGY SIMPLIFICATION BY TYPE II TOPOISOMERASES
Z_Author	Ashley H. Hardin

1

Z_Publisher	The University of Maryland, College Park
Z_Covers	Unspecified
Z_PrintRunHard	6
Z_pubDate	Nov 2011
Z_Territory	USA
Z_Language	English
Z_Notes	I would like to use parts of several figures for my PhD dissertation
Z_Media1	illustration
Z_Author1	Andrew Bates and Anthony Maxwell
Z_Title1	DNA Topology
Z_editedby1	
Z_Material1	Figures: 1.1, 1.2, 2.1, 2.6, 2.11, 2.19
Z_ISBN1	978-0-19-850655-3
Z_OUPpubDate1	10 February 2005
Z_Media2	Text
Z_Author2	
Z_Title2	
Z_editedby2	
Z_Material2	
Z_ISBN2	
Z_OUPpubDate2	
Z_Media3	Text
Z_Author3	
Z_Title3	
Z_editedby3	
Z_ISBN3	
Z_Material3	
Z_OUPpubDate3	
Z_Additional	Thank you!!

Permission for Figure 1.5.1

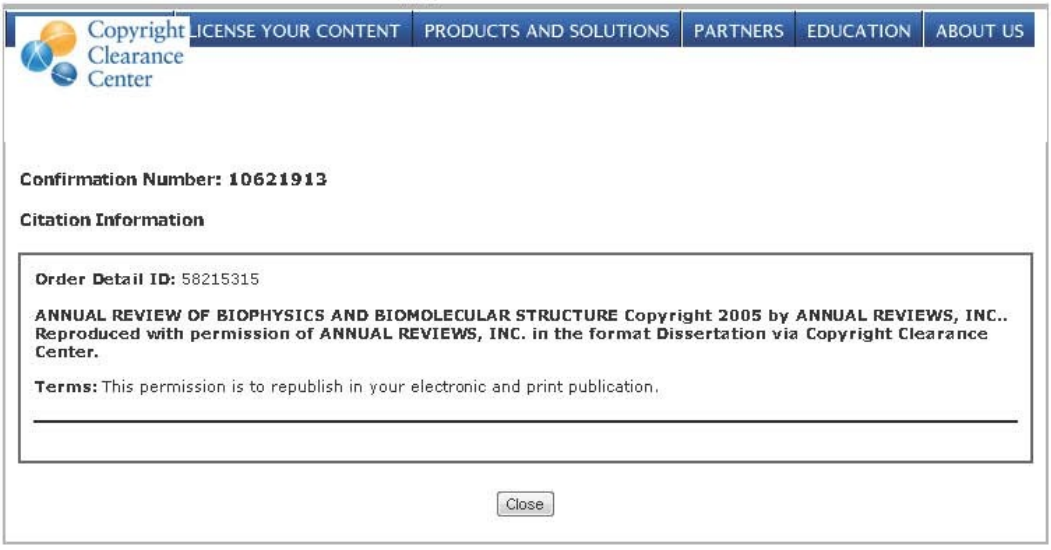

Copyright Clearance Center

LICENSE YOUR CONTENT | PRODUCTS AND SOLUTIONS | PARTNERS | EDUCATION | ABOUT US

Confirmation Number: 10621913

Citation Information

Order Detail ID: 58215315

ANNUAL REVIEW OF BIOPHYSICS AND BIOMOLECULAR STRUCTURE Copyright 2005 by ANNUAL REVIEWS, INC.. Reproduced with permission of ANNUAL REVIEWS, INC. in the format Dissertation via Copyright Clearance Center.

Terms: This permission is to republish in your electronic and print publication.

Close

Permission for Figure 1.5.3

NATURE PUBLISHING GROUP LICENSE TERMS AND CONDITIONS

Oct 29, 2011

This is a License Agreement between Ashley H Hardin ("You") and Nature Publishing Group ("Nature Publishing Group") provided by Copyright Clearance Center ("CCC"). The license consists of your order details, the terms and conditions provided by Nature Publishing Group, and the payment terms and conditions.

All payments must be made in full to CCC. For payment instructions, please see information listed at the bottom of this form.

License Number	2778360029072
License date	Oct 29, 2011
Licensed content publisher	Nature Publishing Group
Licensed content publication	Nature
Licensed content title	Mechanochemical analysis of DNA gyrase using rotor bead tracking
Licensed content author	Jeff Gore, Zev Bryant, Michael D. Stone, Marcelo Nöllmann, Nicholas R. Cozzarelli, Carlos Bustamante
Licensed content date	Jan 5, 2006
Type of Use	reuse in a thesis/dissertation
Requestor type	academic/educational
Format	print and electronic
Portion	figures/tables/illustrations
Number of figures/tables/illustrations	1
High-res required	no
Figures	Figure 3
Author of this NPG article	no
Your reference number	37
Title of your thesis / dissertation	USING SINGLE MOLECULE TECHNIQUES TO DETERMINE THE MECHANISM OF TOPOLOGY SIMPLIFICATION BY TYPE II TOPOISOMERASES
Expected completion date	Nov 2011
Estimated size (number of pages)	130
Total	**0.00 USD**
Terms and Conditions	

Terms and Conditions for Permissions

Nature Publishing Group hereby grants you a non-exclusive license to reproduce this material for this purpose, and for no other use, subject to the conditions below:

1. NPG warrants that it has, to the best of its knowledge, the rights to license reuse of this material. However, you should ensure that the material you are requesting is original to Nature Publishing Group and does not carry the copyright of another entity (as credited in the published version). If the credit line on any part of the material you have requested indicates that it was reprinted or adapted by NPG with permission from another source, then you should also seek permission from that source to reuse the material.

2. Permission granted free of charge for material in print is also usually granted for any electronic version of that

work, provided that the material is incidental to the work as a whole and that the electronic version is essentially equivalent to, or substitutes for, the print version. Where print permission has been granted for a fee, separate permission must be obtained for any additional, electronic re-use (unless, as in the case of a full paper, this has already been accounted for during your initial request in the calculation of a print run). NB: In all cases, web-based use of full-text articles must be authorized separately through the 'Use on a Web Site' option when requesting permission.

3. Permission granted for a first edition does not apply to second and subsequent editions and for editions in other languages (except for signatories to the STM Permissions Guidelines, or where the first edition permission was granted for free).

4. Nature Publishing Group's permission must be acknowledged next to the figure, table or abstract in print. In electronic form, this acknowledgement must be visible at the same time as the figure/table/abstract, and must be hyperlinked to the journal's homepage.

5. The credit line should read:
   Reprinted by permission from Macmillan Publishers Ltd: [JOURNAL NAME] (reference citation), copyright (year of publication)
   For AOP papers, the credit line should read:
   Reprinted by permission from Macmillan Publishers Ltd: [JOURNAL NAME], advance online publication, day month year (doi: 10.1038/sj.[JOURNAL ACRONYM].XXXXX)

   Note: For republication from the *British Journal of Cancer*, the following credit lines apply.
   Reprinted by permission from Macmillan Publishers Ltd on behalf of Cancer Research UK: [JOURNAL NAME] (reference citation), copyright (year of publication) For AOP papers, the credit line should read:
   Reprinted by permission from Macmillan Publishers Ltd on behalf of Cancer Research UK: [JOURNAL NAME], advance online publication, day month year (doi: 10.1038/sj.[JOURNAL ACRONYM].XXXXX)

6. Adaptations of single figures do not require NPG approval. However, the adaptation should be credited as follows:

   Adapted by permission from Macmillan Publishers Ltd: [JOURNAL NAME] (reference citation), copyright (year of publication)

   Note: For adaptation from the *British Journal of Cancer*, the following credit line applies.
   Adapted by permission from Macmillan Publishers Ltd on behalf of Cancer Research UK: [JOURNAL NAME] (reference citation), copyright (year of publication)

7. Translations of 401 words up to a whole article require NPG approval. Please visit http://www.macmillanmedicalcommunications.com for more information. Translations of up to a 400 words do not require NPG approval. The translation should be credited as follows:

   Translated by permission from Macmillan Publishers Ltd: [JOURNAL NAME] (reference citation), copyright (year of publication).

   Note: For translation from the *British Journal of Cancer*, the following credit line applies.
   Translated by permission from Macmillan Publishers Ltd on behalf of Cancer Research UK: [JOURNAL NAME] (reference citation), copyright (year of publication)

We are certain that all parties will benefit from this agreement and wish you the best in the use of this material. Thank you.
Special Terms:
v1.1

If you would like to pay for this license now, please remit this license along with your payment made payable to "COPYRIGHT CLEARANCE CENTER" otherwise you will be invoiced within 48 hours of the license date. Payment should be in the form of a check or money order referencing your account number and this invoice number RLNK0.

Once you receive your invoice for this order, you may pay your invoice by credit card. Please follow instructions provided at that time.

Make Payment To:
Copyright Clearance Center
Dept 001
P.O. Box 843006
Boston, MA 02284-3006

For suggestions or comments regarding this order, contact RightsLink Customer Support:
customercare@copyright.com or +1-877-622-5543 (toll free in the US) or +1-978-646-2777.

Gratis licenses (referencing $0 in the Total field) are free. Please retain this printable license for your reference. No payment is required.

Permission for Figure 1.6.4

NATURE PUBLISHING GROUP LICENSE TERMS AND CONDITIONS

Oct 29, 2011

This is a License Agreement between Ashley H Hardin ("You") and Nature Publishing Group ("Nature Publishing Group") provided by Copyright Clearance Center ("CCC"). The license consists of your order details, the terms and conditions provided by Nature Publishing Group, and the payment terms and conditions.

All payments must be made in full to CCC. For payment instructions, please see information listed at the bottom of this form.

License Number	2778360174006
License date	Oct 29, 2011
Licensed content publisher	Nature Publishing Group
Licensed content publication	Nature
Licensed content title	A kinetic proofreading mechanism for disentanglement of DNA by topoisomerases
Licensed content author	Jie Yan, Marcelo O. Magnasco, John F. Marko
Licensed content date	Oct 28, 1999
Type of Use	reuse in a thesis/dissertation
Requestor type	academic/educational
Format	print and electronic
Portion	figures/tables/illustrations
Number of figures/tables/illustrations	1
Figures	figure 4
Author of this NPG article	no
Your reference number	44
Title of your thesis / dissertation	USING SINGLE MOLECULE TECHNIQUES TO DETERMINE THE MECHANISM OF TOPOLOGY SIMPLIFICATION BY TYPE II TOPOISOMERASES
Expected completion date	Nov 2011
Estimated size (number of pages)	130
Total	0.00 USD
Terms and Conditions	

Terms and Conditions for Permissions

Nature Publishing Group hereby grants you a non-exclusive license to reproduce this material for this purpose, and for no other use, subject to the conditions below:

work, provided that the material is incidental to the work as a whole and that the electronic version is essentially equivalent to, or substitutes for, the print version. Where print permission has been granted for a fee, separate permission must be obtained for any additional, electronic re-use (unless, as in the case of a full paper, this has already been accounted for during your initial request in the calculation of a print run). NB: In all cases, web-based use of full-text articles must be authorized separately through the 'Use on a Web Site' option when requesting permission.

3. Permission granted for a first edition does not apply to second and subsequent editions and for editions in other languages (except for signatories to the STM Permissions Guidelines, or where the first edition permission was granted for free).

4. Nature Publishing Group's permission must be acknowledged next to the figure, table or abstract in print. In electronic form, this acknowledgement must be visible at the same time as the figure/table/abstract, and must be hyperlinked to the journal's homepage.

5. The credit line should read:
   Reprinted by permission from Macmillan Publishers Ltd: [JOURNAL NAME] (reference citation), copyright (year of publication)
   For AOP papers, the credit line should read:
   Reprinted by permission from Macmillan Publishers Ltd: [JOURNAL NAME], advance online publication, day month year (doi: 10.1038/sj.[JOURNAL ACRONYM].XXXXX)

   Note: For republication from the *British Journal of Cancer*, the following credit lines apply.
   Reprinted by permission from Macmillan Publishers Ltd on behalf of Cancer Research UK: [JOURNAL NAME] (reference citation), copyright (year of publication) For AOP papers, the credit line should read:
   Reprinted by permission from Macmillan Publishers Ltd on behalf of Cancer Research UK: [JOURNAL NAME], advance online publication, day month year (doi: 10.1038/sj.[JOURNAL ACRONYM].XXXXX)

6. Adaptations of single figures do not require NPG approval. However, the adaptation should be credited as follows:

   Adapted by permission from Macmillan Publishers Ltd: [JOURNAL NAME] (reference citation), copyright (year of publication)

   Note: For adaptation from the *British Journal of Cancer*, the following credit line applies.
   Adapted by permission from Macmillan Publishers Ltd on behalf of Cancer Research UK: [JOURNAL NAME] (reference citation), copyright (year of publication)

7. Translations of 401 words up to a whole article require NPG approval. Please visit http://www.macmillanmedicalcommunications.com for more information. Translations of up to a 400 words do not require NPG approval. The translation should be credited as follows:

   Translated by permission from Macmillan Publishers Ltd: [JOURNAL NAME] (reference citation), copyright (year of publication).

   Note: For translation from the *British Journal of Cancer*, the following credit line applies.
   Translated by permission from Macmillan Publishers Ltd on behalf of Cancer Research UK: [JOURNAL NAME] (reference citation), copyright (year of publication)

We are certain that all parties will benefit from this agreement and wish you the best in the use of this material. Thank you.
Special Terms:
v1.1

If you would like to pay for this license now, please remit this license along with your payment made payable to "COPYRIGHT CLEARANCE CENTER" otherwise you will be invoiced within 48 hours of the license date. Payment should be in the form of a check or money order referencing your account number and this invoice number RLNK0.

Adapted by permission from Macmillan Publishers Ltd: [JOURNAL NAME] (reference citation), copyright (year of publication)

Note: For adaptation from the *British Journal of Cancer*, the following credit line applies.
Adapted by permission from Macmillan Publishers Ltd on behalf of Cancer Research UK: [JOURNAL NAME] (reference citation), copyright (year of publication)

7. Translations of 401 words up to a whole article require NPG approval. Please visit http://www.macmillanmedicalcommunications.com for more information. Translations of up to a 400 words do not require NPG approval. The translation should be credited as follows:

   Translated by permission from Macmillan Publishers Ltd: [JOURNAL NAME] (reference citation), copyright (year of publication).

   Note: For translation from the *British Journal of Cancer*, the following credit line applies.
   Translated by permission from Macmillan Publishers Ltd on behalf of Cancer Research UK: [JOURNAL NAME] (reference citation), copyright (year of publication)

We are certain that all parties will benefit from this agreement and wish you the best in the use of this material. Thank you.

Special Terms:

v1.1

If you would like to pay for this license now, please remit this license along with your payment made payable to "COPYRIGHT CLEARANCE CENTER" otherwise you will be invoiced within 48 hours of the license date. Payment should be in the form of a check or money order referencing your account number and this invoice number RLNK500655019. Once you receive your invoice for this order, you may pay your invoice by credit card. Please follow instructions provided at that time.

Make Payment To:
Copyright Clearance Center
Dept 001
P.O. Box 843006
Boston, MA 02284-3006

For suggestions or comments regarding this order, contact RightsLink Customer Support: customercare@copyright.com or +1-877-622-5543 (toll free in the US) or +1-978-646-2777.

Gratis licenses (referencing $0 in the Total field) are free. Please retain this printable license for your reference. No payment is required.

Permission for Figure 3.2.5

ELSEVIER LICENSE
TERMS AND CONDITIONS

Nov 21, 2011

This is a License Agreement between Ashley H Hardin ("You") and Elsevier ("Elsevier") provided by Copyright Clearance Center ("CCC"). The license consists of your order details, the terms and conditions provided by Elsevier, and the payment terms and conditions.

All payments must be made in full to CCC. For payment instructions, please see information listed at the bottom of this form.

Supplier	Elsevier Limited The Boulevard,Langford Lane Kidlington,Oxford,OX5 1GB,UK
Registered Company Number	1982084
Customer name	Ashley H Hardin
Customer address	National Institutes of Health Bethesda, MD 20892
License number	2793941326669
License date	Nov 21, 2011
Licensed content publisher	Elsevier
Licensed content publication	Journal of Molecular Biology
Licensed content title	Computational Analysis of the Chiral Action of Type II DNA Topoisomerases
Licensed content author	Konstantin Klenin,Jörg Langowski,Alexander Vologodskii
Licensed content date	5 July 2002
Licensed content volume number	320
Licensed content issue number	2
Number of pages	9
Start Page	359
End Page	367
Type of Use	reuse in a thesis/dissertation
Portion	figures/tables/illustrations
Number of figures/tables/illustrations	1
Format	both print and electronic
Are you the author of this Elsevier article?	No
Will you be translating?	No
Order reference number	

Order reference number	
Title of your thesis/dissertation	USING SINGLE MOLECULE TECHNIQUES TO DETERMINE THE MECHANISM OF TOPOLOGY SIMPLIFICATION BY TYPE II TOPOISOMERASES
Expected completion date	Nov 2011
Estimated size (number of pages)	130
Elsevier VAT number	GB 494 6272 12
Permissions price	0.00 USD
VAT/Local Sales Tax	0.0 USD / 0.0 GBP
Total	0.00 USD
Terms and Conditions	

INTRODUCTION

1. The publisher for this copyrighted material is Elsevier. By clicking "accept" in connection with completing this licensing transaction, you agree that the following terms and conditions apply to this transaction (along with the Billing and Payment terms and conditions established by Copyright Clearance Center, Inc. ("CCC"), at the time that you opened your Rightslink account and that are available at any time at http://myaccount.copyright.com).

GENERAL TERMS

2. Elsevier hereby grants you permission to reproduce the aforementioned material subject to the terms and conditions indicated.

3. Acknowledgement: If any part of the material to be used (for example, figures) has appeared in our publication with credit or acknowledgement to another source, permission must also be sought from that source. If such permission is not obtained then that material may not be included in your publication/copies. Suitable acknowledgement to the source must be made, either as a footnote or in a reference list at the end of your publication, as follows:

"Reprinted from Publication title, Vol /edition number, Author(s), Title of article / title of chapter, Pages No., Copyright (Year), with permission from Elsevier [OR APPLICABLE SOCIETY COPYRIGHT OWNER]." Also Lancet special credit - "Reprinted from The Lancet, Vol. number, Author(s), Title of article, Pages No., Copyright (Year), with permission from Elsevier."

4. Reproduction of this material is confined to the purpose and/or media for which permission is hereby given.

5. Altering/Modifying Material: Not Permitted. However figures and illustrations may be altered/adapted minimally to serve your work. Any other abbreviations, additions, deletions and/or any other alterations shall be made only with prior written authorization of Elsevier Ltd. (Please contact Elsevier at permissions@elsevier.com)

6. If the permission fee for the requested use of our material is waived in this instance, please be advised that your future requests for Elsevier materials may attract a fee.

7. Reservation of Rights: Publisher reserves all rights not specifically granted in the combination of (i) the license details provided by you and accepted in the course of this licensing transaction, (ii) these terms and conditions and (iii) CCC's Billing and Payment terms and conditions.

8. License Contingent Upon Payment: While you may exercise the rights licensed immediately upon issuance of the license at the end of the licensing process for the transaction, provided that you have disclosed complete and accurate details of your proposed use, no license is finally effective unless and until full payment is received from you (either by publisher or by CCC) as provided in CCC's Billing and Payment terms and conditions. If full payment is not received on a timely basis, then any license preliminarily granted shall be deemed automatically revoked and shall be void as if never granted. Further, in the event that you breach any of these terms and conditions or any of CCC's Billing and Payment terms and conditions, the license is automatically revoked and shall be void as if never granted. Use of materials as described in a revoked license, as well as any use of the materials beyond the scope of an unrevoked license, may constitute copyright infringement and publisher reserves the right to take any and all action to protect its copyright in the materials.

9. Warranties: Publisher makes no representations or warranties with respect to the licensed material.

10. Indemnity: You hereby indemnify and agree to hold harmless publisher and CCC, and their respective officers, directors, employees and agents, from and against any and all claims arising out of your use of the licensed material other than as specifically authorized pursuant to this license.

11. No Transfer of License: This license is personal to you and may not be sublicensed, assigned, or transferred by you to any other person without publisher's written permission.

12. No Amendment Except in Writing: This license may not be amended except in a writing signed by both parties (or, in the case of publisher, by CCC on publisher's behalf).

13. Objection to Contrary Terms: Publisher hereby objects to any terms contained in any purchase order, acknowledgment, check endorsement or other writing prepared by you, which terms are inconsistent with these terms and conditions or CCC's Billing and Payment terms and conditions. These terms and conditions, together with CCC's Billing and Payment terms and conditions (which are incorporated herein), comprise the entire agreement between you and publisher (and CCC) concerning this licensing transaction. In the event of any conflict between your obligations established by these terms and conditions and those established by CCC's Billing and Payment terms and conditions, these terms and conditions shall control.

14. Revocation: Elsevier or Copyright Clearance Center may deny the permissions described in this License at their sole discretion, for any reason or no reason, with a full refund payable to you. Notice of such denial will be made using the contact information provided by you. Failure to receive such notice will not alter or invalidate the denial. In no event will Elsevier or Copyright Clearance Center be responsible or liable for any costs, expenses or damage incurred by you as a result of a denial of your permission request, other than a refund of the amount(s) paid by you to Elsevier and/or Copyright Clearance Center for denied permissions.

LIMITED LICENSE

The following terms and conditions apply only to specific license types:

15. **Translation**: This permission is granted for non-exclusive world **English** rights only unless your license was granted for translation rights. If you licensed translation rights you may only translate this content into the languages you requested. A professional translator must perform all translations and reproduce the content word for word preserving the integrity of the article. If this license is to re-use 1 or 2 figures then permission is granted for non-exclusive world rights in all languages.

16. **Website**: The following terms and conditions apply to electronic reserve and author websites:
Electronic reserve: If licensed material is to be posted to website, the web site is to be password-protected and made available only to bona fide students registered on a relevant course if:
This license was made in connection with a course,
This permission is granted for 1 year only. You may obtain a license for future website posting,
All content posted to the web site must maintain the copyright information line on the bottom of each image,
A hyper-text must be included to the Homepage of the journal from which you are licensing at http://www.sciencedirect.com/science/journal/xxxxx or the Elsevier homepage for books at http://www.elsevier.com , and
Central Storage: This license does not include permission for a scanned version of the material to be stored in a central repository such as that provided by Heron/XanEdu.

17. **Author website** for journals with the following additional clauses:

All content posted to the web site must maintain the copyright information line on the bottom of each image, and
he permission granted is limited to the personal version of your paper. You are not allowed to download and post the published electronic version of your article (whether PDF or HTML, proof or final version), nor may you scan the printed edition to create an electronic version,
A hyper-text must be included to the Homepage of the journal from which you are licensing at http://www.sciencedirect.com/science/journal/xxxxx , As part of our normal production process, you will receive an e-mail notice when your article appears on Elsevier's online service ScienceDirect (www.sciencedirect.com). That e-mail will include the article's Digital Object Identifier (DOI). This number provides the electronic link to the published article and should be included in the posting of your personal version. We ask that you wait until you receive this e-mail and have the DOI to do any posting.
Central Storage: This license does not include permission for a scanned version of the material to be stored in a central repository such as that provided by Heron/XanEdu.

18. **Author website** for books with the following additional clauses:
Authors are permitted to place a brief summary of their work online only.
A hyper-text must be included to the Elsevier homepage at http://www.elsevier.com

All content posted to the web site must maintain the copyright information line on the bottom of each image

You are not allowed to download and post the published electronic version of your chapter, nor

may you scan the printed edition to create an electronic version.
Central Storage: This license does not include permission for a scanned version of the material to be stored in a central repository such as that provided by Heron/XanEdu.

19. **Website** (regular and for author): A hyper-text must be included to the Homepage of the journal from which you are licensing at http://www.sciencedirect.com/science/journal/xxxxx. or for books to the Elsevier homepage at http://www.elsevier.com

20. **Thesis/Dissertation**: If your license is for use in a thesis/dissertation your thesis may be submitted to your institution in either print or electronic form. Should your thesis be published commercially, please reapply for permission. These requirements include permission for the Library and Archives of Canada to supply single copies, on demand, of the complete thesis and include permission for UMI to supply single copies, on demand, of the complete thesis. Should your thesis be published commercially, please reapply for permission.

21. **Other Conditions**:

v1.6

If you would like to pay for this license now, please remit this license along with your payment made payable to "COPYRIGHT CLEARANCE CENTER" otherwise you will be invoiced within 48 hours of the license date. Payment should be in the form of a check or money order referencing your account number and this invoice number RLNK500669320. Once you receive your invoice for this order, you may pay your invoice by credit card. Please follow instructions provided at that time.

Make Payment To:
Copyright Clearance Center
Dept 001
P.O. Box 843006
Boston, MA 02284-3006

For suggestions or comments regarding this order, contact RightsLink Customer Support: customercare@copyright.com or +1-877-622-5543 (toll free in the US) or +1-978-646-2777.

Gratis licenses (referencing $0 in the Total field) are free. Please retain this printable license for your reference. No payment is required.

Appendix B: Detailed Methods

Purification of Topoisomerases

yTopo II and hTopo IIα were purified as previously described (30,31). ParC and ParE subunits of Topo IV were purified as previously described (32) with minor modifications. Briefly, the cell pellet was resuspended in 20 mM HEPES (pH 7.5), 400 mM NaCl, 10% glycerol, and 2 mM beta-mercaptoethanol, lysed by sonication and centrifuged. The supernatant was loaded onto a HisTrap HP column (GE Healthcare, Piscataway, NJ) and the protein was eluted with a linear gradient of 0 to 200 mM imidazole. The protein containing fractions were pooled and desalted on a HiPrep desalting column (GE Healthcare). The His-tag was removed by overnight incubation with AcTEV (33) at 4°C using an OD_{280nm} ratio of 1:100 AcTEV:protein, and the cleaved protein was filtered through a HisTrap HP column. The protein was concentrated and further purified on a Superdex 200 10/300 GL column (GE Healthcare). ParC and ParE were quantified by UV absorption, and the complexes were assembled by incubating equimolar quantities of ParC and ParE subunits on ice.

DNA Substrates for AFM Experiments

The AFM DNA substrates are illustrated in Figure 3.3.2. Substrates D1 and D2 are 404 and 393 base pairs (bp) long, respectively, and each contains one of two putative Topo IV binding sequences as determined by Marians and Hiasa (34). Putative binding sequence one (PBS-1) is 5′-GGGCCACTCCTAAAAATCCGGGGTATACCCCGGATTTTTAGG AGTGGCCCGAACCGTTCG-3′, and putative binding sequence two (PBS-2) is 5′-CGCACGGGCCCTAAATAGGGGGGTATACCCCCCTATTTAGAACCGGTTCG-

3′. Substrate D1 was developed by inserting PBS-1 into pUC19 plasmid (New England Biolabs, Ipswitch, MA) between the EcoRI and BamHI restriction sites. The resulting plasmid was amplified by PCR using Phusion DNA polymerase (New England Biolabs), with oligonucleotide primers FOR-1 (5′-GGAGAAAATACCGCATCAGGCGCC-3′) and REV-1 (5′-TGTGAGTTAGCTCACTCATTAGGCACCC-3′). Substrate D2 was constructed in the same manner as D1, but contained PBS-2. Substrates D3 and D4 were designed to improved binding affinity. They are 360 bp long but include a four bp staggered double stranded break at or near the middle of the molecule. Position 217 to 576 of plasmid pUC19 was amplified by PCR, using primers FOR-1 and REV-1 as described above, and digested with either EcoRI to make D3, XmaI to make D4, or left intact as a control, D6. EcoRI and XmaI were used to vary the sequence of the four bp overhang. D5 is composed of position 279 to 550 of pUC19, amplified by PCR using oligonucleotide primers FOR-2 (5′-TCGGTGCGGGCCTCTTCGC-3′) and REV-2 (5′-CCCAGGCTTTACACTTTATGCTTCCGGCTCG-3′). This substrate is 272 bp long and was digested by XmaI at its restriction site, producing equal 136 bp fragments. This is a symmetric version of D4 since it contains much of the same sequence and is cut with the same restriction enzyme. All restriction endonucleases were obtained from New England Biolabs.

DNA Substrates for Single Molecule FRET Experiments

DNA substrates used in single molecule FRET experiments, F1 and F2, were adapted from Dong *et al.* (25) but were lengthened to prevent interaction between the protein and the surface of the glass slide. As shown in Figure 3.2.5A, fluorescent DNA substrates F1

and F2 contain a complementary 4 bp overhang that allowed the transiently annealed region to be stabilized by a bound topoisomerase and thus generate a FRET signal. Substrate F1 contains an Alexa647 fluorophore at the 5' blunt end of the segment. The sequence of the top strand of F1 is: 5′-[Alexa647]-GCGCCGAGGATGACGATG-3′. The sequence of the complementary bottom strand of this substrate is: 3′-CGCGGCTCCTACTGCTAC'GCCC-5′, where the " ' " denotes the beginning of the 4 bp overhang (Figure 3.2.5A). Substrate F2 contains an internal Alexa546 fluorphore, located the same distance from the 4 bp overhang as the Alexa647 on F1 and a biotin at the 3′ blunt end. The sequence of the top strand of F2 is: 5′-CGGG'CATCGTCATCCTCGGCGCCGTGCGTAACTGTCCGCCCTGCTGCGAGT GG-[Biotin]-3′, where the " ' " denotes the beginning of the 4 bp overhang. The sequence of the complementary bottom strand is 3′- GTAGCAGTAGGAGCCGCG-[Alexa546]-GCACGCATTGACAGGCGGGACGACGCTCACC-5′ (Figure 3.2.5A). Each of these oligos, including the fluorophores and biotin, was synthesized by Eurofins MWG Operon (Huntsville, AL).

Relaxation Assays

Wheat germ topoisomerase I (Topo IB) (Promega, Madison, WI), Topo IV, yTopo II, and hTopo IIα were incubated with plasmid pBR322 (New England Biolabs) at protein:DNA concentrations of 25 nM:50 nM in a 60 µl reaction containing 40 mM Tris-HCl (pH 7.5), 6 mM $MgCl_2$, 100 mM KOAc, 1 mM DTT, 1 mM ATP, 0.1 mM EDTA, and 10 mg/ml bovine serum albumin (BSA) (New England Biolabs). Unless otherwise noted, all chemicals were obtained from Sigma-Aldrich (St. Louis, MO). Reactions were incubated

overnight at 37°C and stopped with a buffer containing 0.1% SDS, 10 mM EDTA, and TrackIt™ Cyan/Yellow Loading Buffer (Invitrogen, Carlsbad, CA). 10 µl of each reaction was loaded onto a 1% Tris-Acetate EDTA (TAE) agarose gel containing 1 µg/ml chloroquine to resolve topoisomers. Gels were run overnight at 2.5 V/cm at 4°C in 1X TAE supplemented with 1 µg/ml chloroquine, destained in water for 2 hours to remove chloroquine, and stained for 40 minutes in a solution of 1X SYBR® Green I nucleic acid stain prior to imaging with a Biospectrum® AC Imaging System (UVP, Upland, CA). VisionworksLS (UVP) and ImageJ (National Institutes of Health, Bethesda, MD) software were used to obtain and analyze gel intensity profiles.

Protein-DNA Complex Formation for AFM Experiments

Topo IV (300 nM-2.4 µM) and DNA (60 nM-480 nM) were incubated on ice for 30 minutes, at a protein:DNA ratio of 5:1 for all reactions. Binding buffers 1-4: BB1 (50 mM HEPES (pH 7.5), 5 mM $MgCl_2$, 50 mM NaCl, and 5% v/v glycerol), BB2 (50 mM Tris-HCl (pH 7.5), 10 mM $MgCl_2$, 20 mM KCl, 5 mM DTT, and 2.5% v/v glycerol), BB3 (50 mM Tris-HCl (pH 7.5), 10 mM $MgCl_2$, 10 mM KCl, 5 mM DTT, and 2.5% v/v glycerol), and BB4 (50 mM Tris-HCl (pH 7.5), 10 mM CaOAc, 12.5 mM sodium malonate, 5 mM DTT, and 5% v/v glycerol) were used for the incubation reactions of Topo IV with DNA substrates D1-D5. Some of the Topo IV-DNA reactions in BB1 and BB2 were supplemented with 50 µM quinolone (norfloxacin, ciprofloxacin, or levofloxacin). yTopo II and hTopo IIα were incubated with DNA substrates D4 and D5 under the same conditions as Topo IV, but they were incubated exclusively in BB4. In the binding reactions, the salt concentration of the enzyme storage buffers increased

the concentration of NaCl by ~1 mM for Topo IV, whereas the yTopo II and hTopo IIα storage buffers increased the NaCl concentration by ~50 mM.

AFM Experiments

Complexes were assembled as described above and diluted 8-12 fold in deposition buffer (50 mM HEPES (pH 7.5), 5 mM $MgCl_2$, 50 mM NaCl, and 2-5% v/v glycerol) to a final protein:DNA concentration of 60 nM:12 nM in a total volume of 20 μL (35). The entire 20 μL sample was immediately deposited on a freshly cleaved mica surface (Spruce Pine Mica Company, Spruce Pine, NC) and allowed to adsorb for ~30 seconds at room temperature before being gently rinsed with Milli-Q water for 30 seconds. Residual water was wicked from the mica using a strip of filter paper, and the mica was gently blown dry with compressed air (Whoosh-Duster™, Control Company, Houston, TX). Images were captured using Multimode JV and EV scanners and Nanoscope IIIa and V controllers (Veeco Metrology, Santa Barbara, CA). Data were collected using tapping mode in air. SSS-NCHR (tip radius <5 nm) (Nanosensors, Neuchatel, Switzerland) and AC160TS (tip radius <10 nm) (Olympus, Tokyo, Japan) tapping mode silicon probes were used for imaging. Both cantilever probes had spring constants of ~42 N/m and resonance frequencies of ~300 kHz. Images were collected at a rate of 2-3 Hz and had a resolution of 512x512 pixels per square micron.

Single Molecule FRET Experiments

A custom-built prism-type total internal reflection (TIR) fluorescence microscope based on an Olympus IX71 was used to measure bend angles at the single molecule level. A flow cell was constructed with double-sided tape (SA-S-1L 0.12 mm Grace BioLabs

(Bend, OR) Secure-Seal adhesive double sided tape) sandwiched between a coverslip (Gold Seal (Thermo Scientific, Portsmouth, NH) #1 22 mm x 40 mm) and a quartz slide (SPI (West Chester, PA) 25 mm x 76 mm x 1 mm). Both the coverslip and the quartz slide were cleaned extensively using NaOH, ethanol, and acetone. TIR of the excitation laser was achieved using a quartz prism (CVI (Albuquerque, NM) PLBC-5.0-79.5-SS) and occurred at the interface of the quartz slide and the buffer in the flow cell. The evanescent wave at the interface generated due to TIR was used to excite fluorescently labeled substrates within a thin layer of ~250 nm. The excitation laser, with a power of ~3 mW at 532 nm (CrystaLaser (Reno, NV) GCL-025-L-0.5%), was focused onto an area of approximately 150 x 150 μm^2 to excite Alexa546 labeled donor substrates. Alexa647 labeled acceptor substrates were used to detect FRET between two substrates due to imposed bending by different type II topoisomerases. Fluorescence was collected by a water immersion objective with 60X magnification and 1.2 numerical aperture (Olympus (Center Valley, PA) UPLSAPO60XWIR). Additional magnification of 1.6X in the Olympus IX71 was used to obtain a total magnification of 96X. Excitation light was rejected using a HQ550LP filter (Chroma, Bellows Falls, VT). Donor emission and acceptor emission were separated using a Dual View (Photometrics (Tucson, AZ) DV2-SYS with 06-EML2 Optical Filter Set) and detected using an EMCCD camera (Andor (South Windsor, CT) DV897DCS-BV). Andor iQ 1.8 software was used to control the camera and record movies with 100 ms time resolution. Fluorescence intensities of both donor and acceptor as a function of time for individual molecules were extracted for further analysis.

The buffer used in single molecule FRET experiments was the same used for ensemble activity assays: 40 mM Tris-HCl (pH 7.5), 6 mM $MgCl_2$, 1 mM DTT, 100 mM potassium acetate, 50 μg/ml BSA and 0.1 mM EDTA. For these experiments, a mixture of 25 nM Alexa546 (donor) labeled DNA substrate F1 (Figure 3.2.5A), 25 nM Alexa647 (acceptor) labeled DNA substrate F2 (Figure 3.2.5A) and 1 μM type IIA topoisomerase was incubated on ice for 30 min. 3 μL of this mixture was diluted in 1 mL buffer, flowed into the flow cell, and incubated for 10 min to immobilize the donor substrates prior to recording movies.

Appendix C: Sample smFRET Traces

Sample Yeast Topo II Traces

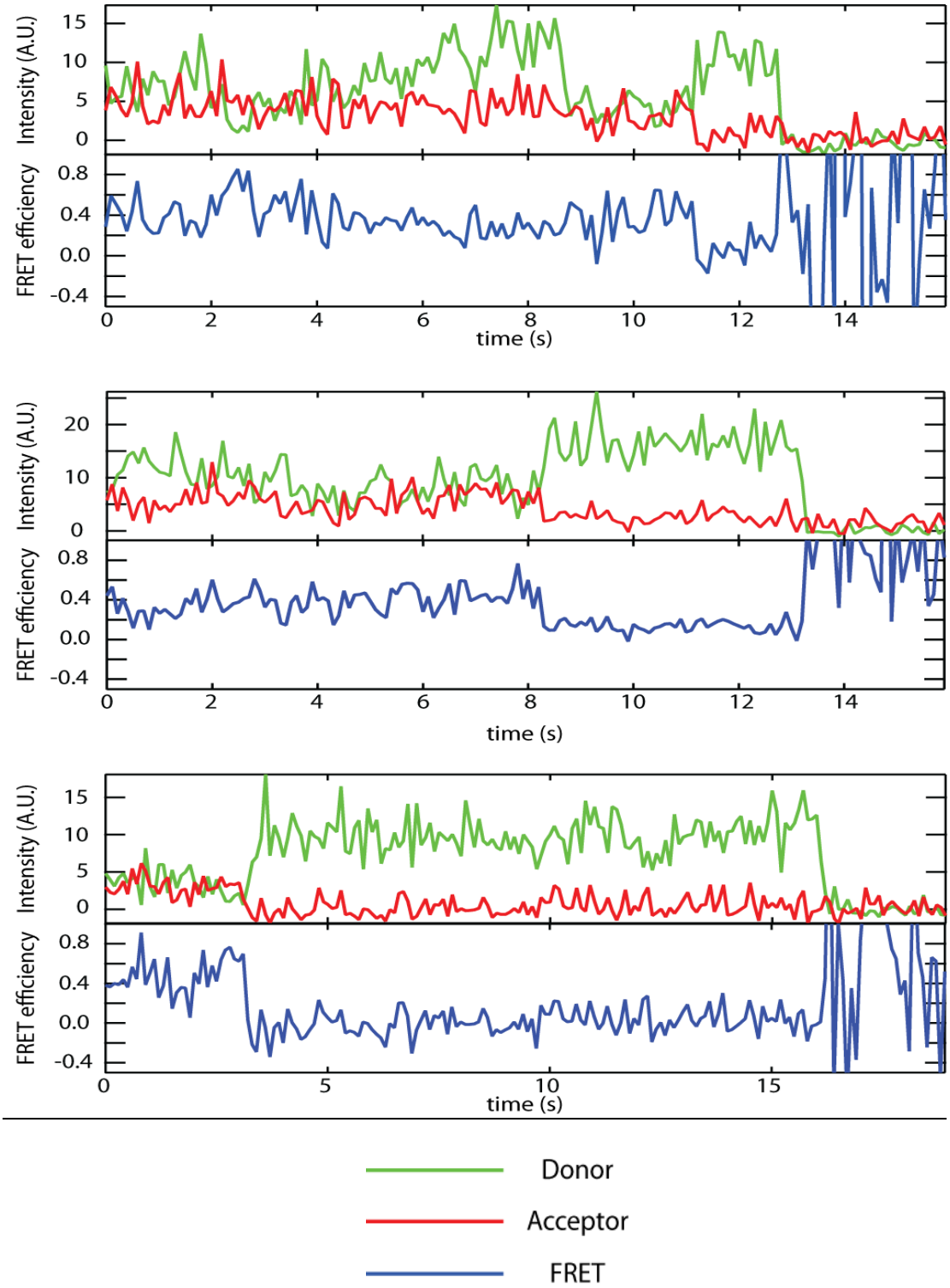

Sample Human Topo IIα Traces

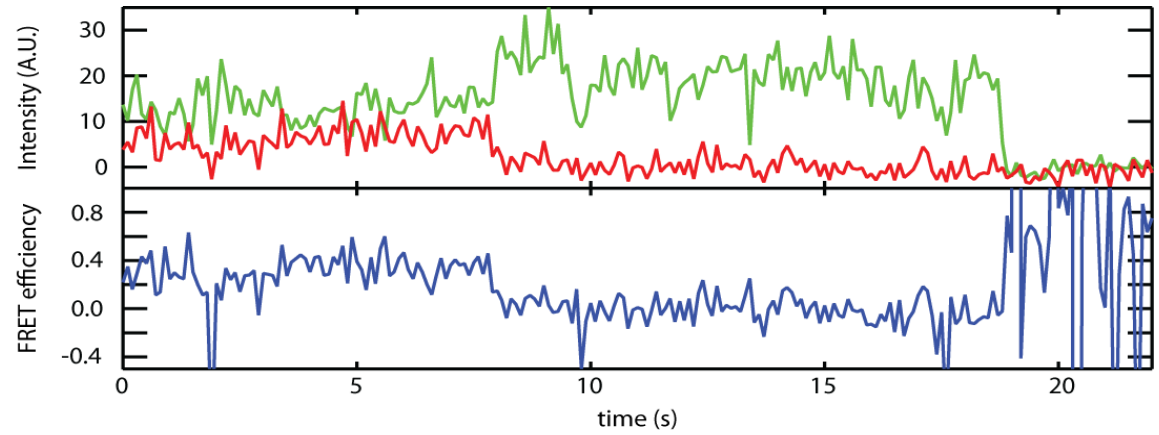

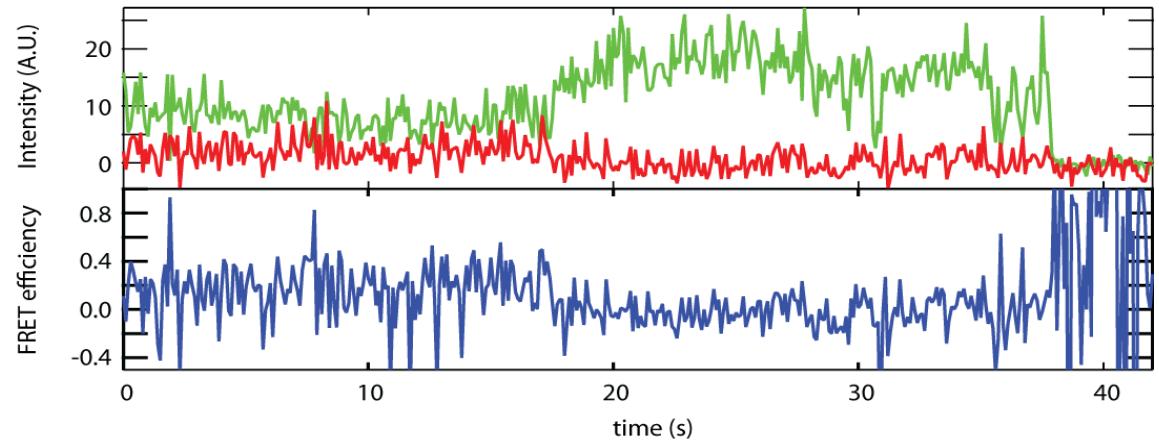

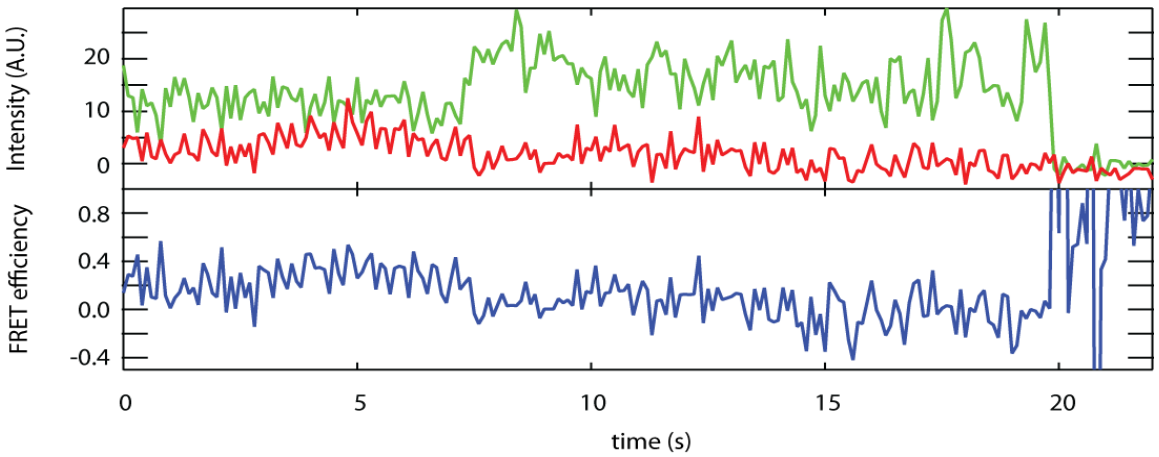

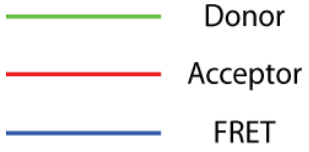

Sample *E. coli* Topo IV Traces

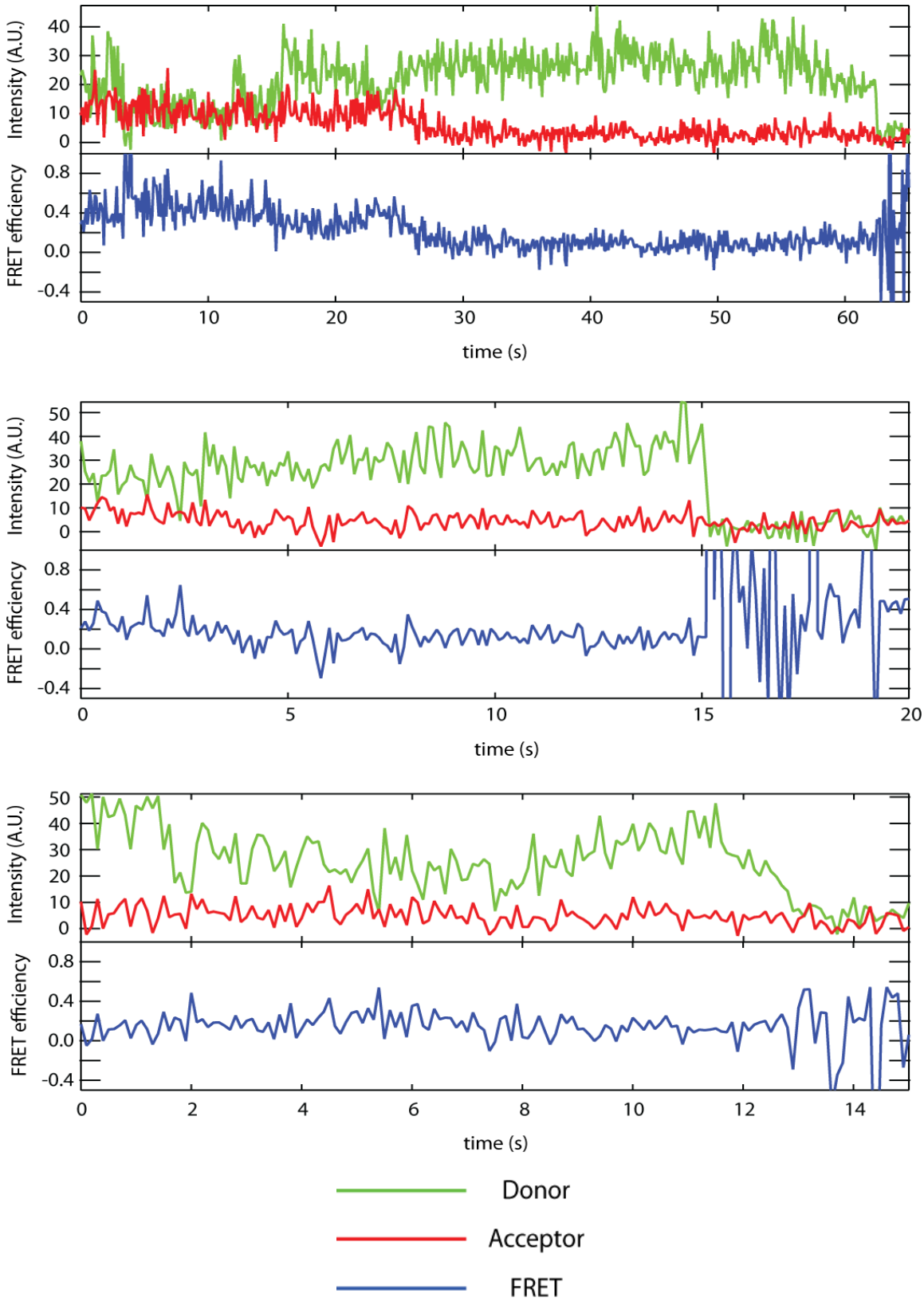

Appendix D: Relationship between Topology Simplification Ability of Type II Topoisomerases and Predicted DNA Bending

We obtained the relation between topology simplification activity determined from the narrowing of the topoisomer distribution (R_{Lk}) and the degree of DNA bending (θ) predicted by the bend angle model. Klenin *et al.* simulated the ratio of equilibrium to non-equilibrium steady-state knotting probability (R_{kn}) as a function of the imposed bend angle (12). To relate R_{Lk} to θ, we needed to determine the relationship between R_{Lk} and R_{kn}. Rybenkov *et al.* showed that non-equilibrium unknotting (R_{kn}), decatenation (R_{cat}), and unlinking (R_{Lk}) activities are highly correlated (13). Using the experimentally determined relationships among these measures of topology simplification from Rybenkov *et al.* (13) and the results of the bend angle simulations from Klenin *et al*. (12), we determined the relationship between R_{Lk} and θ shown in Figure 8 of the main text.

We re-plotted and fit the experimental relationships between R_{kn} and R_{cat} (Equation [A1]) and between R_{Lk} and R_{cat} (Equation [A2]) from Figure 3 of Rybenkov *et al.* (13) (Figure A.0.1A and B). These two equations were solved to establish the relationship between R_{kn} and R_{Lk} (Equation [A3]).

$$R_{kn} = (R_{cat})^{1.5} \quad \text{[A1]}$$

$$R_{Lk} = 1 + 0.28 * \ln(R_{cat}) \quad \text{[A2]}$$

$$R_{Lk} = 1 + 0.19 * \ln(R_{kn}) \quad \text{[A3]}$$

We extracted and fit the data relating R_{kn} and θ from Figure 5 of Klenin *et al.* (12) to determine the relationship between R_{kn} and θ (Equation [A4]) (Figure A.0.1C). Combining Equations [A3] and [A4], we solved for the relation between R_{Lk} and θ (Equation [A5]). Because the relationship between R_{Lk} and R_{kn} is logarithmic (Equation [A3]) and the relationship between R_{kn} and θ is exponential (Equation [A4]), the relationship between R_{Lk} and θ is linear (Equation [A5]) (Figure A.0.1D).

$$R_{kn} = e^{(0.014*\theta)} \quad [A4]$$

$$R_{Lk} = 1 + 0.0026 * \theta \quad [A5]$$

We used the relationship shown in Eq. S5 and the average of our measured and previously published values of R_{Lk} for Topo IV (1.81), yTopo II (1.27), and hTopo IIα (1.6) to determine the predicted bend angles for each enzyme: ~310°, ~100°, and ~230°, respectively, as shown in Figure 3.6.1.

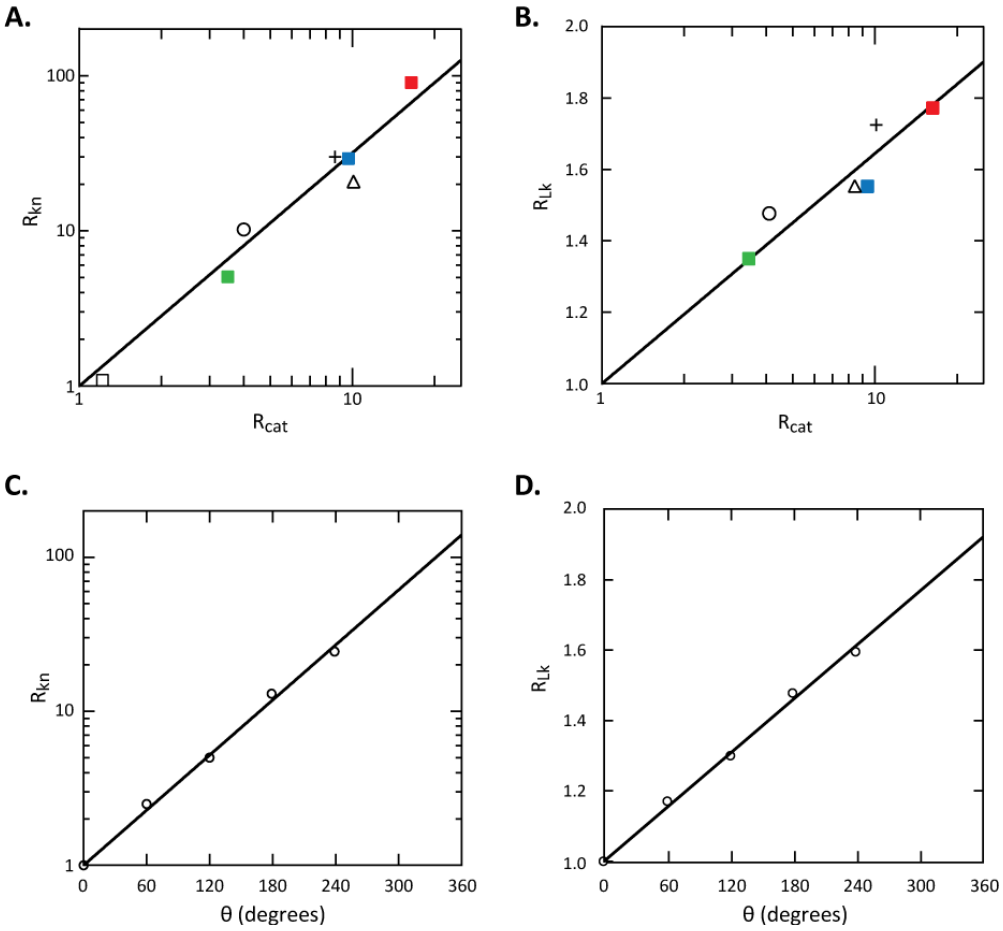

Figure A.0.1 Relationships among measures of non-equilibrium topology simplification and the predicted imposed bend angle. **A.** Log-log plot of the measured ratio of equilibrium to steady state knotting probability (R_{kn}) as a function of the measured ratio of equilibrium to steady state catenation probability (R_{cat}), re-plotted from Figure 3 of Rybenkov *et al.* (13). (Reprinted with permission from AAAS.) The line is the fit to the data: $R_{kn} = (R_{cat})^{1.5}$. **B.** Lin-log plot of the measured ratio of equilibrium to steady-state topoisomer variance (R_{Lk}) as a function of R_{cat} re-plotted from Figure 3 of Rybenkov *et al.* (13). (Reprinted with permission from AAAS.) The line is the fit to the data: $R_{Lk} = 1 + 0.28 \cdot \ln(R_{cat})$. The points are measurements for different type IIA topoisomerases: Topo IV (red squares), hTopo IIα (blue squares), yTopo II (green

squares), phage T2 topoisomerase (○), *D. melanogaster* topoisomerase II (+), yTopo II with a C-terminal deletion (Δ), and topoisomerase III (□). **C.** Log-lin plot of R_{kn} as a function of the imposed bend angle from simulations. The line is a fit to the data: $R_{kn} = \exp(0.014 \cdot \theta)$. (Reprinted from *The Journal of Molecular Biology*, Volume 320, Klenin, K., Langowski, J. and Vologodskii, A., Computational analysis of the chiral action of type II DNA topoisomerases. Pages 359-367, (2002), with permission from Elsevier.) **D.** Plot of R_{Lk} as a function of θ derived from the data and the fits to the data in panels A, B, and C (see text). The line is the derived fit to the data (see text): $R_{Lk} = 1 + 0.0026 \cdot \theta$.

Appendix E: Sample Magnetic Tweezers Relaxation Traces

Sample magnetic tweezers traces from a bead with a geometry of $2e/L = 0.65$:

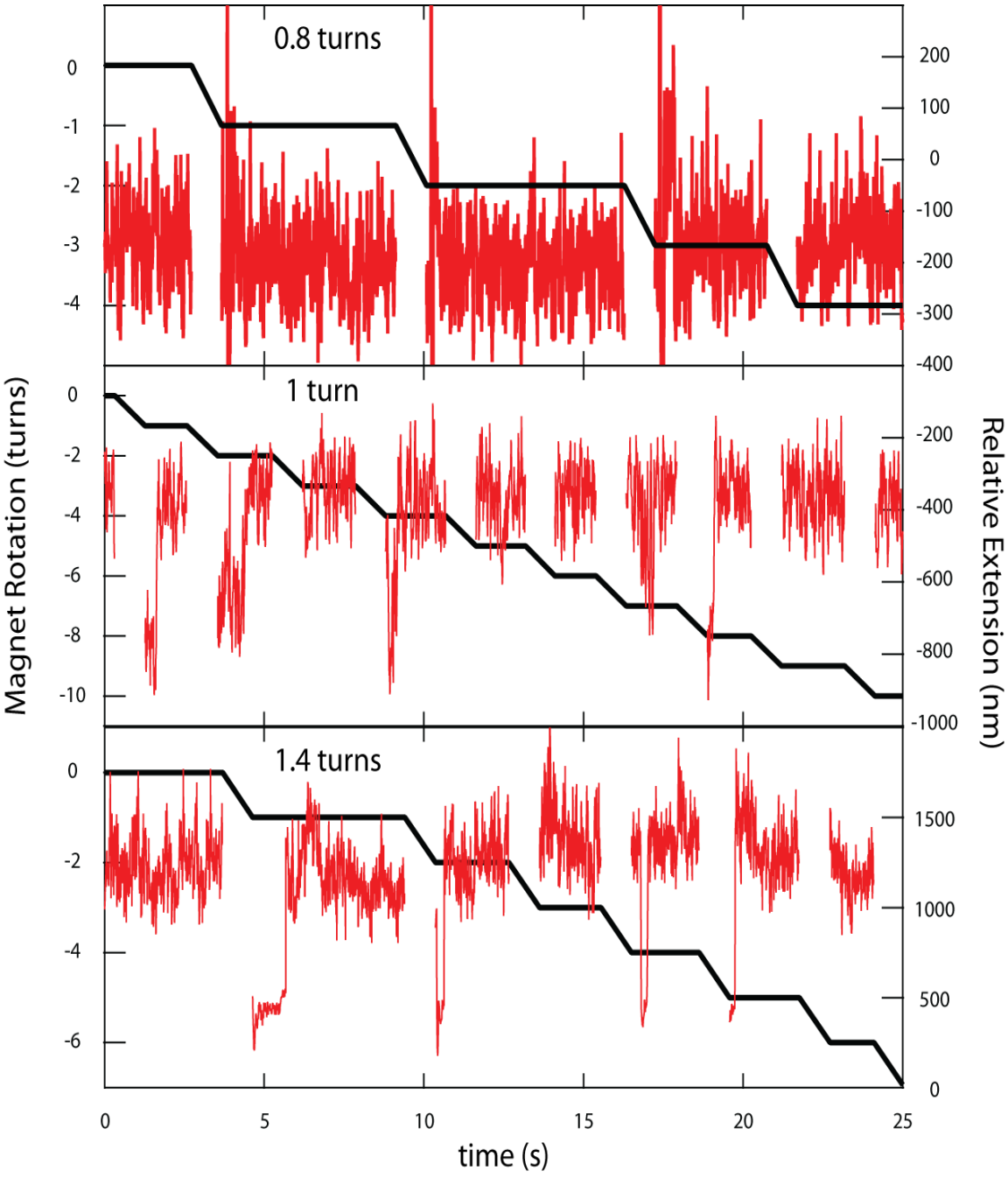

Bibliography

1. Dahm, R. (2008) Discovering DNA: Friedrich Miescher and the early years of nucleic acid research. *Hum Genet*, **122**, 565-581.

2. Avery, O.T., Macleod, C.M. and McCarty, M. (1944) Studies on the Chemical Nature of the Substance Inducing Transformation of Pneumococcal Types : Induction of Transformation by a Desoxyribonucleic Acid Fraction Isolated from Pneumococcus Type Iii. *J Exp Med*, **79**, 137-158.

3. Chargaff, E. (1951) Structure and function of nucleic acids as cell constituents. *Fed Proc*, **10**, 654-659.

4. Watson, J.D. and Crick, F.H. (1953) Molecular structure of nucleic acids; a structure for deoxyribose nucleic acid. *Nature*, **171**, 737-738.

5. Watson, J.D. and Crick, F.H. (1953) The structure of DNA. *Cold Spring Harb Symp Quant Biol*, **18**, 123-131.

6. Franklin, R.E. and Gosling, R.G. (1953) Evidence for 2-chain helix in crystalline structure of sodium deoxyribonucleate. *Nature*, **172**, 156-157.

7. Bates, A.D. and Maxwell, A. (2005) *DNA Topology*. Oxford University Press, New York.

8. Wang, J.C. (1998) Moving one DNA double helix through another by a type II DNA topoisomerase: the story of a simple molecular machine. *Q Rev Biophys*, **31**, 107-144.

9. Meselson, M. and Stahl, F.W. (1958) The Replication of DNA in Escherichia Coli. *Proc Natl Acad Sci U S A*, **44**, 671-682.

10. Pohl, W.F. and Roberts, G.W. (1978) Topological considerations in the theory of replication of DNA. *J Math Biol*, **6**, 383-402.

11. Rodley, G.A., Scobie, R.S., Bates, R.H. and Lewitt, R.M. (1976) A possible conformation for double-stranded polynucleotides. *Proc Natl Acad Sci U S A*, **73**, 2959-2963.

12. Sasisekharan, V. and Pattabiraman, N. (1978) Structure of DNA predicted from stereochemistry of nucleoside derivatives. *Nature*, **275**, 159-162.

13. Sasisekharan, V., Pattabiraman, N. and Gupta, G. (1978) Some implications of an alternative structure for DNA. *Proc Natl Acad Sci U S A*, **75**, 4092-4096.

14. Crick, F.H., Wang, J.C. and Bauer, W.R. (1979) Is DNA really a double helix? *J Mol Biol*, **129**, 449-457.

15. Wang, J.C. (2009) *Untangling the Double Helix: DNA Entanglement and the Action of the DNA Topoisomerases*. Cold Spring Harbor Laboratory Press, New York.

16. Vinograd, J., Lebowitz, J., Radloff, R., Watson, R. and Laipis, P. (1965) The twisted circular form of polyoma viral DNA. *Proc Natl Acad Sci U S A*, **53**, 1104-1111.

17. Pommier, Y. (2006) Topoisomerase I inhibitors: camptothecins and beyond. *Nat Rev Cancer*, **6**, 789-802.

18. Bauer, W.R. (1978) Structure and reactions of closed duplex DNA. *Annu Rev Biophys Bioeng*, **7**, 287-313.

19. Fuller, F.B. (1971) The writhing number of a space curve. *Proc Natl Acad Sci U S A*, **68**, 815-819.

20. Fuller, F.B. (1978) Decomposition of the linking number of a closed ribbon: A problem from molecular biology. *Proc Natl Acad Sci U S A*, **75**, 3557-3561.

21. Forterre, P., Gribaldo, S., Gadelle, D. and Serre, M.C. (2007) Origin and evolution of DNA topoisomerases. *Biochimie*, **89**, 427-446.

22. Aaij, C. and Borst, P. (1972) The gel electrophoresis of DNA. *Biochim Biophys Acta*, **269**, 192-200.

23. Sharp, P.A., Sugden, B. and Sambrook, J. (1973) Detection of two restriction endonuclease activities in Haemophilus parainfluenzae using analytical agarose--ethidium bromide electrophoresis. *Biochemistry*, **12**, 3055-3063.

24. Borst, P. (2005) Ethidium DNA agarose gel electrophoresis: how it started. *IUBMB Life*, **57**, 745-747.

25. Bauer, W. and Vinograd, J. (1970) Interaction of closed circular DNA with intercalative dyes. II. The free energy of superhelix formation in SV40 DNA. *J Mol Biol*, **47**, 419-435.

26. Hsieh, T.S. and Wang, J.C. (1975) Thermodynamic properties of superhelical DNAs. *Biochemistry*, **14**, 527-535.

27. Stuchinskaya, T., Mitchenall, L.A., Schoeffler, A.J., Corbett, K.D., Berger, J.M., Bates, A.D. and Maxwell, A. (2009) How do type II topoisomerases use ATP hydrolysis to simplify DNA topology beyond equilibrium? Investigating the relaxation reaction of nonsupercoiling type II topoisomerases. *J Mol Biol*, **385**, 1397-1408.

28. Liu, L.F., Perkocha, L., Calendar, R. and Wang, J.C. (1981) Knotted DNA from bacteriophage capsids. *Proc Natl Acad Sci U S A*, **78**, 5498-5502.

29. Hudson, B. and Vinograd, J. (1967) Catenated circular DNA molecules in HeLa cell mitochondria. *Nature*, **216**, 647-652.

30. Clayton, D.A. and Vinograd, J. (1967) Circular dimer and catenate forms of mitochondrial DNA in human leukaemic leucocytes. *Nature*, **216**, 652-657.

31. Champoux, J.J. and Dulbecco, R. (1972) An activity from mammalian cells that untwists superhelical DNA--a possible swivel for DNA replication. *Proc Natl Acad Sci U S A*, **69**, 143-146.

32. Gellert, M., Mizuuchi, K., O'Dea, M.H. and Nash, H.A. (1976) DNA gyrase: an enzyme that introduces superhelical turns into DNA. *Proc Natl Acad Sci U S A*, **73**, 3872-3876.

33. Schoeffler, A.J. and Berger, J.M. (2008) DNA topoisomerases: harnessing and constraining energy to govern chromosome topology. *Q Rev Biophys*, **41**, 41-101.

34. Charvin, G., Strick, T.R., Bensimon, D. and Croquette, V. (2005) Tracking topoisomerase activity at the single-molecule level. *Annu Rev Biophys Biomol Struct*, **34**, 201-219.

35. Rybenkov, V.V., Ullsperger, C., Vologodskii, A.V. and Cozzarelli, N.R. (1997) Simplification of DNA topology below equilibrium values by type II topoisomerases. *Science*, **277**, 690-693.

36. Pommier, Y., Leo, E., Zhang, H.L. and Marchand, C. (2010) DNA Topoisomerases and Their Poisoning by Anticancer and Antibacterial Drugs. *Chemistry & Biology*, **17**, 421-433.

37. Hsiang, Y.H., Hertzberg, R., Hecht, S. and Liu, L.F. (1985) Camptothecin induces protein-linked DNA breaks via mammalian DNA topoisomerase I. *J Biol Chem*, **260**, 14873-14878.

38. Koster, D.A., Palle, K., Bot, E.S., Bjornsti, M.A. and Dekker, N.H. (2007) Antitumour drugs impede DNA uncoiling by topoisomerase I. *Nature*, **448**, 213-217.

39. Belova, G.I., Prasad, R., Kozyavkin, S.A., Lake, J.A., Wilson, S.H. and Slesarev, A.I. (2001) A type IB topoisomerase with DNA repair activities. *Proc Natl Acad Sci U S A*, **98**, 6015-6020.

40. Gadelle, D., Filee, J., Buhler, C. and Forterre, P. (2003) Phylogenomics of type II DNA topoisomerases. *Bioessays*, **25**, 232-242.

41. Wang, J.C. (2002) Cellular roles of DNA topoisomerases: a molecular perspective. *Nat Rev Mol Cell Biol*, **3**, 430-440.

42. Berger, J.M. (1998) Structure of DNA topoisomerases. *Biochim Biophys Acta*, **1400**, 3-18.

43. Champoux, J.J. (2001) DNA topoisomerases: structure, function, and mechanism. *Annu Rev Biochem*, **70**, 369-413.

44. Deweese, J.E. and Osheroff, N. (2009) The DNA cleavage reaction of topoisomerase II: wolf in sheep's clothing. *Nucleic Acids Res*, **37**, 738-748.

45. Bates, A.D. and Maxwell, A. (2007) Energy coupling in type II topoisomerases: why do they hydrolyze ATP? *Biochemistry*, **46**, 7929-7941.

46. Liu, Z.R., Deibler, R.W., Chan, H.S. and Zechiedrich, L. (2009) The why and how of DNA unlinking. *Nucleic Acids Res*, **37**, 661-671.

47. Ishii, S., Murakami, T. and Shishido, K. (1991) Gyrase inhibitors increase the content of knotted DNA species of plasmid pBR322 in Escherichia coli. *J Bacteriol*, **173**, 5551-5553.

48. Shishido, K., Komiyama, N. and Ikawa, S. (1987) Increased production of a knotted form of plasmid pBR322 DNA in Escherichia coli DNA topoisomerase mutants. *J Mol Biol*, **195**, 215-218.

49. Deibler, R.W., Mann, J.K., Sumners, D.W.L. and Zechiedrich, L. (2007) Hin-mediated DNA knotting and recombining promote replicon dysfunction and mutation. *BMC Molecular Biology*, **8**.

50. Hardin, A.H., Sarkar, S.K., Seol, Y., Liou, G.F., Osheroff, N. and Neuman, K.C. (2011) Direct measurement of DNA bending by type IIA topoisomerases: implications for non-equilibrium topology simplification. *Nucleic Acids Res*, **39**, 5729-5743.

51. Corbett, K.D., Shultzaberger, R.K. and Berger, J.M. (2004) The C-terminal domain of DNA gyrase A adopts a DNA-bending beta-pinwheel fold. *Proc Natl Acad Sci U S A*, **101**, 7293-7298.

52. McClendon, A.K., Rodriguez, A.C. and Osheroff, N. (2005) Human topoisomerase IIalpha rapidly relaxes positively supercoiled DNA: implications for enzyme action ahead of replication forks. *J Biol Chem*, **280**, 39337-39345.

53. Nitiss, J.L. (2009) Targeting DNA topoisomerase II in cancer chemotherapy. *Nat Rev Cancer*, **9**, 338-350.

54. Buhler, C., Lebbink, J.H., Bocs, C., Ladenstein, R. and Forterre, P. (2001) DNA topoisomerase VI generates ATP-dependent double-strand breaks with two-nucleotide overhangs. *J Biol Chem*, **276**, 37215-37222.

55. Corbett, K.D. and Berger, J.M. (2003) Structure of the topoisomerase VI-B subunit: implications for type II topoisomerase mechanism and evolution. *EMBO J*, **22**, 151-163.

56. Corbett, K.D., Benedetti, P. and Berger, J.M. (2007) Holoenzyme assembly and ATP-mediated conformational dynamics of topoisomerase VI. *Nat Struct Mol Biol*, **14**, 611-619.

57. Buck, G.R. and Zechiedrich, E.L. (2004) DNA disentangling by type-2 topoisomerases. *J Mol Biol*, **340**, 933-939.

58. Yan, J., Magnasco, M.O. and Marko, J.F. (1999) A kinetic proofreading mechanism for disentanglement of DNA by topoisomerases. *Nature*, **401**, 932-935.

59. Vologodskii, A.V., Zhang, W., Rybenkov, V.V., Podtelezhnikov, A.A., Subramanian, D., Griffith, J.D. and Cozzarelli, N.R. (2001) Mechanism of topology simplification by type II DNA topoisomerases. *Proc Natl Acad Sci U S A*, **98**, 3045-3049.

60. Klenin, K., Langowski, J. and Vologodskii, A. (2002) Computational analysis of the chiral action of type II DNA topoisomerases. *J Mol Biol*, **320**, 359-367.

61. Trigueros, S., Salceda, J., Bermudez, I., Fernandez, X. and Roca, J. (2004) Asymmetric removal of supercoils suggests how topoisomerase II simplifies DNA topology. *J Mol Biol*, **335**, 723-731.

62. Vologodskii, A. (2009) Theoretical models of DNA topology simplification by type IIA DNA topoisomerases. *Nucleic Acids Res*, **37**, 3125-3133.

63. Dong, K.C. and Berger, J.M. (2007) Structural basis for gate-DNA recognition and bending by type IIA topoisomerases. *Nature*, **450**, 1201-1205.

64. Laponogov, I., Sohi, M.K., Veselkov, D.A., Pan, X.S., Sawhney, R., Thompson, A.W., McAuley, K.E., Fisher, L.M. and Sanderson, M.R. (2009) Structural insight into the quinolone-DNA cleavage complex of type IIA topoisomerases. *Nat Struct Mol Biol*, **16**, 667-669.

65. Laponogov, I., Pan, X.S., Veselkov, D.A., McAuley, K.E., Fisher, L.M. and Sanderson, M.R. (2010) Structural basis of gate-DNA breakage and resealing by type II topoisomerases. *PLoS One*, **5**, e11338.

66. Wohlkonig, A., Chan, P.F., Fosberry, A.P., Homes, P., Huang, J., Kranz, M., Leydon, V.R., Miles, T.J., Pearson, N.D., Perera, R.L. *et al.* (2010) Structural basis of quinolone inhibition of type IIA topoisomerases and target-mediated resistance. *Nat Struct Mol Biol*, **17**, 1152-1153.

67. Liu, Z.R., Zechiedrich, L. and Chan, H.S. (2010) Local site preference rationalizes disentangling by DNA topoisomerases. *Phys Rev E*, **81**, 031902.

68. Randall, G.L., Pettitt, B.M., Buck, G.R. and Zechiedrich, E.L. (2006) Electrostatics of DNA-DNA juxtapositions: consequences for type II topoisomerase function. *Journal of Physics-Condensed Matter*, **18**, S173-S185.

69. Liu, Z.R., Mann, J.K., Zechiedrich, E.L. and Chan, H.S. (2006) Topological information embodied in local juxtaposition geometry provides a statistical mechanical basis for unknotting by type-2 DNA topoisomerases. *J Mol Biol*, **361**, 268-285.

70. Liu, Z.R., Zechiedrich, E.L. and Chan, H.S. (2006) Inferring global topology from local juxtaposition geometry: Interlinking polymer rings and ramifications for topoisomerase action. *Biophys J*, **90**, 2344-2355.

71. Liu, Z.R., Zechiedrich, L. and Chan, H.S. (2010) Action at Hooked or Twisted-Hooked DNA Juxtapositions Rationalizes Unlinking Preference of Type-2 Topoisomerases. *J Mol Biol*, **400**, 963-982.

72. Yan, J., Magnasco, M.O. and Marko, J.F. (2001) Kinetic proofreading can explain the supression of supercoiling of circular DNA molecules by type-II topoisomerases. *Phys Rev E Stat Nonlin Soft Matter Phys*, **63**, 031909.

73. Moore, D.D. and Voytas, D. (2002) In Ausubel, F. M., Brent, R., Kingston, R. E., Moore, D. D., Seidman, J. G., Smith, J. A. and Struhl, K. (eds.), *Short Protocols in Molecular Biology*. 5th ed. John Wiley and Sons, Inc, Vol. 1, pp. 2.1-2.55.

74. Schmidt, B.H., Burgin, A.B., Deweese, J.E., Osheroff, N. and Berger, J.M. (2010) A novel and unified two-metal mechanism for DNA cleavage by type II and IA topoisomerases. *Nature*, **465**, 641-644.

75. Charvin, G., Strick, T.R., Bensimon, D. and Croquette, V. (2005) Topoisomerase IV bends and overtwists DNA upon binding. *Biophys J*, **89**, 384-392.

76. Binnig, G., Quate, C.F. and Gerber, C. (1986) Atomic force microscope. *Phys Rev Lett*, **56**, 930-933.

77. Alessandrini, A. and Facci, P. (2005) AFM: a versatile tool in biophysics. *Meas Sci Technol*, **16**, R65-R92.

78. Rivetti, C., Guthold, M. and Bustamante, C. (1996) Scanning force microscopy of DNA deposited onto mica: equilibration versus kinetic trapping studied by statistical polymer chain analysis. *J Mol Biol*, **264**, 919-932.

79. Joo, C. and Ha, T. (2008) In Selvin, P. R. and Ha, T. (eds.), *Single-Molecule Techniques: A Laboratory Manual*. Cold Spring Harbor Laboratory Press, New York, pp. 3-36.

80. Roy, R., Hohng, S. and Ha, T. (2008) A practical guide to single-molecule FRET. *Nat Methods*, **5**, 507-516.

81. Clegg, R.M. (1992) Fluorescence resonance energy transfer and nucleic acids. *Methods Enzymol*, **211**, 353-388.

82. Marians, K.J. and Hiasa, H. (1997) Mechanism of quinolone action. A drug-induced structural perturbation of the DNA precedes strand cleavage by topoisomerase IV. *J Biol Chem*, **272**, 9401-9409.

83. Wang, H., Yang, Y., Schofield, M.J., Du, C.W., Fridman, Y., Lee, S.D., Larson, E.D., Drummond, J.T., Alani, E., Hsieh, P. *et al.* (2003) DNA bending and unbending by MutS govern mismatch recognition and specificity. *Proc Natl Acad Sci U S A*, **100**, 14822-14827.

84. Erie, D.A., Yang, G., Schultz, H.C. and Bustamante, C. (1994) DNA bending by Cro protein in specific and nonspecific complexes: implications for protein site recognition and specificity. *Science*, **266**, 1562-1566.

85. Rees, W.A., Keller, R.W., Vesenka, J.P., Yang, G. and Bustamante, C. (1993) Evidence of DNA bending in transcription complexes imaged by scanning force microscopy. *Science*, **260**, 1646-1649.

86. Allan, B.W., Garcia, R., Maegley, K., Mort, J., Wong, D., Lindstrom, W., Beechem, J.M. and Reich, N.O. (1999) DNA bending by EcoRI DNA methyltransferase accelerates base flipping but compromises specificity. *J Biol Chem*, **274**, 19269-19275.

87. Sokal, R.R. and Rohlf, F.J. (1969) *Biometry*. W. H. Freeman and Company, San Francisco, CA.

88. Bevington, P. and Robinson, K.D. (2002) *Data Reduction and Error Analysis for the Physical Sciences* Third ed. McGraw-Hill Science/Engineering/Math, New York, NY.

89. Efron, B. and Tibshirani, R. (1991) Statistical Data Analysis in the Computer Age. *Science*, **253**, 390-395.

90. Leone, F.C., Nottingham, R.B. and Nelson, L.S. (1961) Folded Normal Distribution. *Technometrics*, **3**, 543-550.

91. Le Cam, E., Fack, F., Menissier-de Murcia, J., Cognet, J.A., Barbin, A., Sarantoglou, V., Revet, B., Delain, E. and de Murcia, G. (1994) Conformational analysis of a 139 base-pair DNA fragment containing a single-stranded break and its interaction with human poly(ADP-ribose) polymerase. *J Mol Biol*, **235**, 1062-1071.

92. Cherny, D.I., Striker, G., Subramaniam, V., Jett, S.D., Palecek, E. and Jovin, T.M. (1999) DNA bending due to specific p53 and p53 core domain-DNA interactions visualized by electron microscopy. *J Mol Biol*, **294**, 1015-1026.

93. Pastre, D., Pietrement, O., Fusil, S., Landousy, F., Jeusset, J., David, M.O., Hamon, L., Le Cam, E. and Zozime, A. (2003) Adsorption of DNA to mica

mediated by divalent counterions: a theoretical and experimental study. *Biophys J*, **85**, 2507-2518.

94. Bustamante, C. and Rivetti, C. (1996) Visualizing protein-nucleic acid interactions on a large scale with the scanning force microscope. *Annu Rev Biophys Biomol Struct*, **25**, 395-429.

95. Moukhtar, J., Fontaine, E., Faivre-Moskalenko, C. and Arneodo, A. (2007) Probing persistence in DNA curvature properties with atomic force microscopy. *Phys Rev Lett*, **98**, 178101.

96. Faas, F.G., Rieger, B., van Vliet, L.J. and Cherny, D.I. (2009) DNA deformations near charged surfaces: electron and atomic force microscopy views. *Biophys J*, **97**, 1148-1157.

97. Sushko, M.L., Shluger, A.L. and Rivetti, C. (2006) Simple model for DNA adsorption onto a mica surface in 1:1 and 2:1 electrolyte solutions. *Langmuir*, **22**, 7678-7688.

98. Rivetti, C., Walker, C. and Bustamante, C. (1998) Polymer chain statistics and conformational analysis of DNA molecules with bends or sections of different flexibility. *J Mol Biol*, **280**, 41-59.

99. Rivetti, C., Guthold, M. and Bustamante, C. (1999) Wrapping of DNA around the E.coli RNA polymerase open promoter complex. *EMBO J*, **18**, 4464-4475.

100. Lu, Y., Weers, B.D. and Stellwagen, N.C. (2003) Analysis of the intrinsic bend in the M13 origin of replication by atomic force microscopy. *Biophys J*, **85**, 409-415.

101. Neuman, K.C., Charvin, G., Bensimon, D. and Croquette, V. (2009) Mechanisms of chiral discrimination by topoisomerase IV. *Proc Natl Acad Sci U S A*, **106**, 6986-6991.

102. Stone, M.D., Bryant, Z., Crisona, N.J., Smith, S.B., Vologodskii, A., Bustamante, C. and Cozzarelli, N.R. (2003) Chirality sensing by Escherichia coli topoisomerase IV and the mechanism of type II topoisomerases. *Proc Natl Acad Sci U S A*, **100**, 8654-8659.

103. Pastre, D., Hamon, L., Sorel, I., Le Cam, E., Curmi, P.A. and Pietrement, O. (2009) Specific DNA-protein interactions on mica investigated by atomic force microscopy. *Langmuir*, **26**, 2618-2623.

104. Bustamante, C., Marko, J.F., Siggia, E.D. and Smith, S. (1994) Entropic elasticity of lambda-phage DNA. *Science*, **265**, 1599-1600.

105. Deweese, J.E. and Osheroff, N. (2009) Coordinating the two protomer active sites of human topoisomerase IIalpha: nicks as topoisomerase II poisons. *Biochemistry*, **48**, 1439-1441.

106. Hopfield, J.J. (1974) Kinetic proofreading: a new mechanism for reducing errors in biosynthetic processes requiring high specificity. *Proc Natl Acad Sci U S A*, **71**, 4135-4139.

107. Roca, J. and Wang, J.C. (1992) The capture of a DNA double helix by an ATP-dependent protein clamp: a key step in DNA transport by type II DNA topoisomerases. *Cell*, **71**, 833-840.

108. Roca, J. and Wang, J.C. (1994) DNA transport by a type II DNA topoisomerase: evidence in favor of a two-gate mechanism. *Cell*, **77**, 609-616.

109. Neuman, K.C. and Nagy, A. (2008) Single-molecule force spectroscopy: optical tweezers, magnetic tweezers and atomic force microscopy. *Nat Methods*, **5**, 491-505.

110. Lionnet, T., Allemand, J.-F., Revyakin, A., Strick, T.R., Saleh, O.A., Bensimon, D. and Croquette, V. (2008) In Selvin, P. R. and Ha, T. (eds.), *Single Molecule Techniques: A Laboratory Manual*. Cold Spring Harbor Laboratory Press, New York, pp. 347-369.

111. Strick, T.R., Allemand, J.F., Bensimon, D. and Croquette, V. (1998) Behavior of supercoiled DNA. *Biophys J*, **74**, 2016-2028.

112. Perals, K., Cornet, F., Merlet, Y., Delon, I. and Louarn, J.M. (2000) Functional polarization of the Escherichia coli chromosome terminus: the dif site acts in chromosome dimer resolution only when located between long stretches of opposite polarity. *Molecular microbiology*, **36**, 33-43.

113. Charvin, G., Bensimon, D. and Croquette, V. (2003) Single-molecule study of DNA unlinking by eukaryotic and prokaryotic type-II topoisomerases. *Proc Natl Acad Sci U S A*, **100**, 9820-9825.

114. Charvin, G., Vologodskii, A., Bensimon, D. and Croquette, V. (2005) Braiding DNA: experiments, simulations, and models. *Biophys J*, **88**, 4124-4136.

115. Vologodskii, A.V. and Cozzarelli, N.R. (1994) Conformational and thermodynamic properties of supercoiled DNA. *Annu Rev Biophys Biomol Struct*, **23**, 609-643.

116. Sturges, H.A. (1926) The Choice of a Class Interval. *Journal of the American Statistical Association*, **21**, 65-66.